2014

Reservoirs Modeling of Gas hydrate deposits in North Slope of Alaska and Gulf of Mexico

Manohar Gaddipati

Reservoirs Modeling of Gas hydrate deposits in North Slope of Alaska and Gulf of Mexico

Manohar Gaddipati

Dissertation submitted to the
College of Engineering and Mineral Resources
at West Virginia University
in partial fulfillment of the requirements
for the degree of

Doctor of Philosophy
in
Chemical Engineering

Dr. Brian J. Anderson
Dr. H. Ilkin Bilgesu
Dr. Charter Stinespring
Dr. John Zondlo
Dr. Hema Siriwardane

Department of Chemical Engineering
Morgantown, West Virginia
2014

Key words: Gas hydrates, CMG STARS, PBU L-Pad, Gulf of Mexico, Methane drate reservoir simulation, Gas production from hydrates

ProQuest LLC.
789 East Eisenhower Parkway
P.O. Box 1346
Ann Arbor, MI 48106 - 1346

Reservoir Modeling of Gas hydrate deposits in North Slope of Alaska and Gulf of Mexico

Abstract

Manohar Gaddipati

In order to address the world's growing energy demand, the necessity to explore more and more unconventional sources of energy arises. Recently there has been increased interest in the potential of natural gas hydrates as an alternate energy resource. Methane hydrates are crystalline solids, very similar to ice, in which non-polar molecules are trapped inside the cages formed by water molecules. Methane hydrates could be potentially a vast source of energy. The production of natural gas from hydrates economically poses a big challenge to today's scientific world. Two sites for greatest potential for gas production from gas hydrates as identified by USGS and NETL/DOE are North Slope (ANS) Alaska and the Gulf of Mexico (GOM). In this work specific locations of hydrate deposits are examined, namely the Prudhoe Bay L Pad (PBU L-Pad) and Walker Ridge 313 (WR313) deposits in the ANS and GOM. Reservoir modeling in this work is primarily based on these two gas hydrate deposits.

The uncertainty of reservoir parameters such as hydrate reaction kinetics, the permeability of hydrate bearing sediment, Porosity and permeability of the shale layer boundary on gas production is studied in this work. Gas production from a horizontal well as opposed to a vertical well is evaluated using a mechanistic well bore model. A preliminary assessment of thermal disturbance due to a hot well bore penetrating hydrate deposits in the PBU L pad site is performed using CMG STARS coupled geotechnical model. The results of this study indicate that the extent of hydrate dissociation around a hot wellbore is limited by the thermal diffusion of heat moving radially away from the casing and cement.

In April and May of 2009, the U.S. Department of Energy (DOE) National Energy Technology Laboratory (NETL) in collaboration with the U.S. Geological Survey (USGS), the U.S. Minerals Management Service, an industry research consortium led by Chevron, and others completed a marine hydrate drilling expedition in the Gulf of Mexico called the Joint Industry Project (Leg II) expedition. A complex heterogeneous 3-D model using well log data seismic data are constructed and simulated using CMG STARS and Petrel. An uncertainty assessment of gas production from the WR313 G well on reservoir parameters is performed using a Latin-hyper cube Monte Carlo sampling. Results of the reservoir simulations indicate very high potential for producing methane from these marine hydrate deposits using depressurization due to *in situ* temperature and pressure related to the great depth of the deposits. The predicted production rates display high (5-40 MMscf/day) rates making the reservoirs to be attractive locations for further exploration. Special cases were considered to estimate influence of permeable over- and under burden on production.

Table of Contents

Acknowledgements

I thank my research advisor Dr. Brian J. Anderson for his encouragement, guidance and his help throughout the course of my research. Besides being my research advisor, he has been of great support in a foreign country to me both personally and professionally. I will remain indebted to him for the inspiration he has given me.

Many thanks to Dr. Charter Stinespring, Dr. Hema Siriwardane, Dr. John Zondlo, Dr. Huseyin I. Bilgesu and Dr. Wu Zhang for being a part of my advisory committee and for all the help and suggestions they have offered.

I sincerely thank George Moridis, Joseph W. Wilder, Scott Wilson, Mark D. White, Mehran Pooladi-Darvish, Kelly Rose, Ray Boswell, Masanori Kurihara for sharing their research results and indirectly supporting my research project.

It is family that makes a person and I am very lucky to have a wonderful family. I am very grateful to my father, Narasimha Rao, my mother, Nagamani for their love and my brother Samba who has been my role model since childhood.

Thank you one and all.

Manohar Gaddipati

Lists of Figures

Lists of Tables

Introduction

The demand of natural gas as a clean source of energy is rapidly increasing in the world. Natural gas hydrates are drawing attention worldwide as an unconventional source of energy because of the vast availability and the foreseen increase in the demand of natural gas. Gas hydrates are combinations of gas and water molecules that form under conditions of high pressure and low temperature. In order to produce gas from hydrate reservoir, it is necessary to destroy the crystalline water structure which traps hydrocarbons. Reservoir modeling of gas hydrate reservoir is challenging due to the dynamics involved and the role of parameters that control the dynamics for exploitation is critical. Therefore, the objective of this research is to understand through reservoir simulations the role of different reservoir parameters and the complicated process involved in the gas production from gas hydrate reservoirs.

In this study, reservoir simulations are performed on two specific sites (i) Prudhoe Bay L Pad; Alaska North Slope and (ii) Walker Ridge 313 hydrate deposit in the Gulf of Mexico. These two sites are the best available targets in U.S in terms of reservoir quality and available data. Well logs and predicted seismic hydrate saturation data are used for building reservoir models. Commercial geological software (Petrel, 2011)) is used in building 3-D complex dipping reservoir models for Walker Ridge 313 hydrate deposit. The full, heterogeneous three-dimensional models for Walker Ridge 313 represents one of the most complete and complex reservoir models of a marine hydrate deposit to date.

The problem description and objectives of each section are different from each other and are explained in detail in following sections.

The following section (Chapter 1) introduces the theory and background of gas hydrates. A brief description of previous collaborative simulation work performed as a member of NETL/USGS

“International methane hydrate Code comparison group” is provided in this section of the thesis. Then, the objectives of this research are described and a summary of thesis is presented.

1. Background

Gas hydrates are non-stoichiometric combinations of gas and water molecules that form under conditions of high pressures and low temperatures. Hydrates are crystalline solids, very similar to ice, in which non-polar molecules are trapped inside the cages of water molecules. Non-polar molecules are typically low molecular weight gases which include natural gases like methane, ethane and propane. Methane hydrates are generally found in the Arctic and ocean floor at depths greater than 500 m and 1500 m respectively (Sloan and Koh, 2007). Naturally-occurring hydrates are mainly methane hydrates due to the availability of low molecular weight natural gas beneath the surface. Methane hydrates receiving increased attention due to increase in gas prices their high energy density and vast potential resource. One volume of hydrate on dissociation releases as much of 164 volumes (Kvenvolden, 1993) of natural gas. The methane hydrate dissociation and reformation reaction is described by the equation

$$CH_4 . N_H H_2O \leftrightarrow N_H H_2O + CH_4 \quad (1)$$

where N_H is the hydration number (~ 6.1). The production of natural gas from hydrates in an economic manner poses a big challenge to today's scientific world. Different numerical reservoir simulators are developed to model the gas hydrate dissociation behavior.

2.1 Growing Energy demand and importance of Hydrate

Energy is inevitable to human life and energy requirements around the world are ever increasing. Energy supply and demand plays an important role in the economic development of a country. Energy consumption is expected to increase more than 53% when projected to 2035 (EIA, 2011). Organization for Economic Corporation and development (OECD) countries like U.S., Europe, Japan, Korea etc. consume the most energy per capita. Energy demand in OECD countries are projected to grow annually at a slower rate of 0.9%, whereas energy consumption in non-OECD

emerging economies like China and India are projected to grow at an annual rate of 2.3% due to rapid economic growth. Since the U.S imports 60% of its crude oil demand, a fluctuation in the crude oil price has been seen to have a great impact on U.S economy. Figure 2.1 show the average crude oil price in both nominal and real dollars projected to 2035 (EIA, 2011). The nominal price for crude oil per barrel is projected to be $183 in 2035.

Natural gas is the world's fastest growing fossil fuel with consumption expected to increase at a average rate of 1.6% per year from 2008 to 2035. Natural gas is the fuel of choice in many regions of the world in the electric power and industrial sectors, in part because of its lower carbon intensity when compared with coal and oil. In addition, it is an attractive alternative fuel for new power generation plants because of low capital costs and favorable thermal efficiencies.

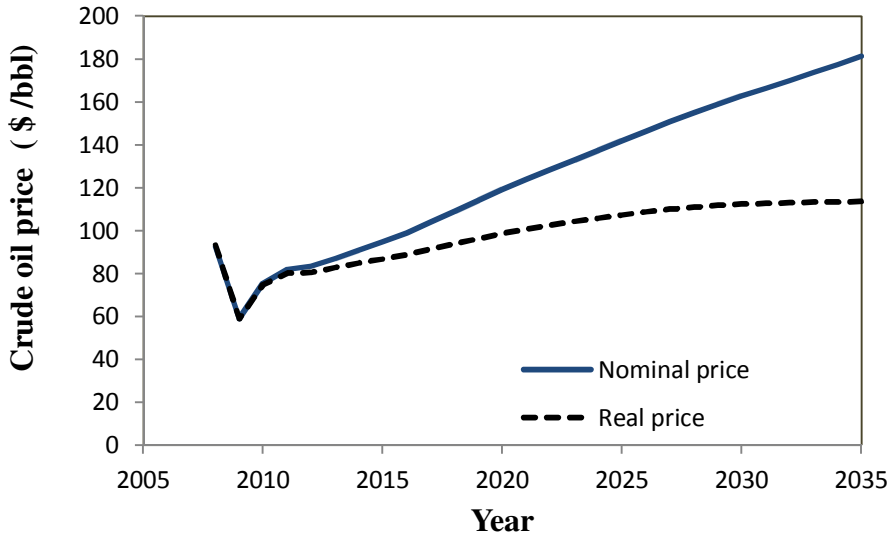

Figure 1.1 Average imported crude oil price projected to 2035 (EIA, 2011)

In recent years, U.S shale gas production has increased 14-fold leading to a decline in net imports of natural gas. The high increase in natural gas production is attributed to the recent advances in horizontal drilling and hydraulic fracturing technologies. The net imports of natural gas are projected to fall from 11% in 2011 to 1% in 2035(). Figure 1.2 shows the U.S. natural gas

production and consumption in quadrillion BTU/year. The U.S. counts on natural gas as a major part of its energy portfolio. Natural gas production by source is shown in Figure 1.3 (EIA, 2008). Onshore and offshore conventional resources show a decline from 1990 to 2030. Production of gas from onshore unconventional resources like shale gas, tight gas and coal bed methane shows a tremendous increase when projected to 2030. There is potentially a vast resource of hydrate accumulations in the United States. A fraction of the methane that is recovered from hydrates could address the increase in future energy demand significantly. Since hydrate deposits are known to act as stabilizers of geological strata, it is important to know the behavior of hydrates and to understand the hazards of drilling in the ocean floor and continental shelves (Collett et al., 2009). Methane is a greenhouse gas and plays major role in global climate change, and thus there have been speculations about explosions of gas hydrates and occasional burps of large amounts of methane into the atmosphere in the past (Ruppel, 2011).

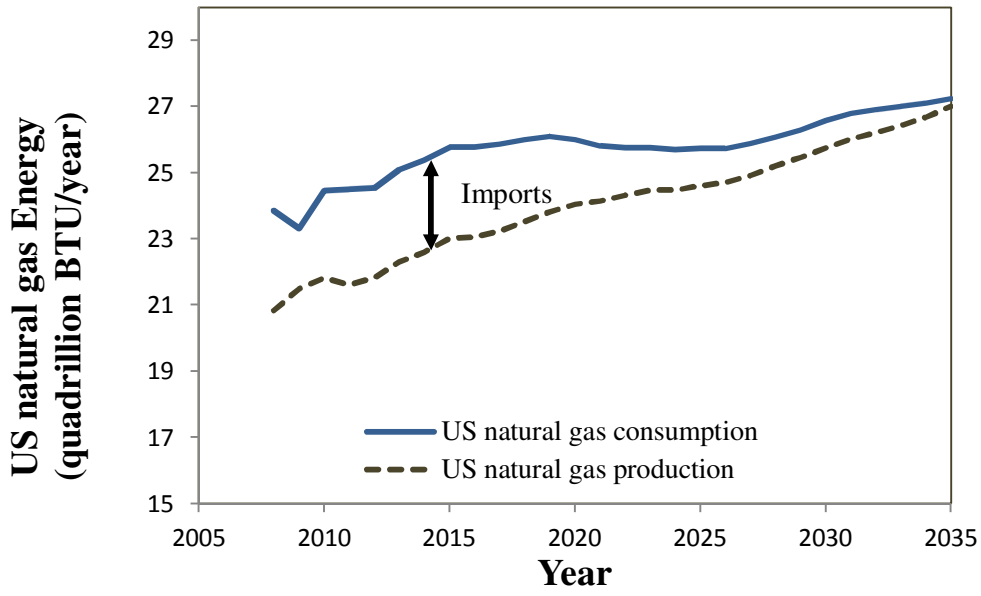

Figure 1.2 U.S. Natural gas consumption and production

Therefore, a rise in sea temperature could trigger hydrate dissociation releasing methane into the atmosphere provoking landslides and tsunamis (Archer, 2007; Kelley et al., 1994; Ocean, 2011). Hence it is important to study methane hydrate in connection with natural gas demand as well as climate and geology.

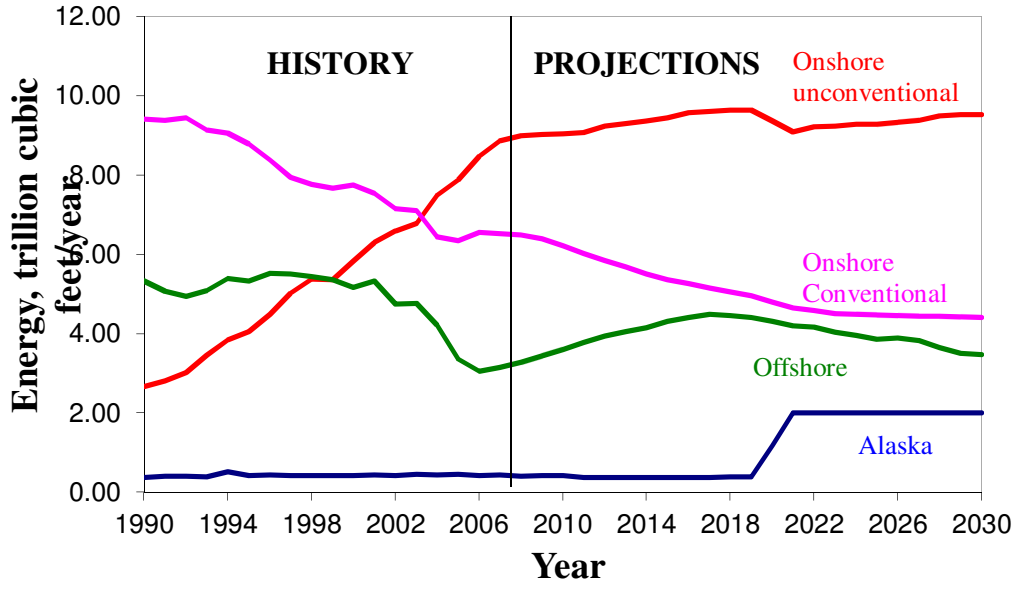

Figure 1.3 U.S natural gas production by source, projections up to 2030

1.2 History, Occurrences

Researchers believe that in 1810, Sir Humphrey Davy first obtained hydrates by cooling a saturated solution of chlorine in water well below 9°C. Also, there is evidence that hydrates were retrieved more than 30 years before Davy. Joseph Priestly in 1778 (Makogon, 1997) had obtained SO_2 hydrate by cooling an aqueous solution and by combining the gaseous SO_2 in ice as well.

Natural gas hydrates are ice-like solids that do not flow but rapidly grow and agglomerate to sizes that can block pipelines (Hammerschmidt, 1934). Gas hydrates have been a known menace in gas and oil pipelines for many decades. Hydrates are known to plug the pipelines that could cause unexpected fountains because of pipeline rupture. Hydrates can form in the pipelines whenever the pertinent temperature and pressure conditions are met and form in valves, lines, elbows etc. Hydrate plugs are formed at the hydrocarbon/water interface which eventually hinders flow and can cause shutdown of the pipelines. A shut down cold well is very prone to hydrate formation (). The current knowledge about hydrate location in the world is incomplete. The majority of known gas hydrate occurrences are on continental margins. Figure 1.4 shows a map of locations of gas hydrates (Kvenvolden et al., 2001) and current volume estimates of hydrate bound gas (Moridis et al., 2011) vary widely between 10^{15} to 10^{18} m^3 (standard conditions).

1.3 Natural gas hydrates

1.3.1 Structure

Hydrates are formed due to the unusual behavior of water molecule and its orientation. The water molecules act as the host and the gas molecules are guest molecules embedded in the cages of ice due to hydrogen bonding and van der Waal's forces. The water molecule consists of one oxygen atom covalently bonded to two hydrogen atoms at an angle between the atoms is 104.5°. There are two unbonded electrons on the oxygen atom which induces partially negative charge on the oxygen atom due to its high electro- negativity relative to hydrogen atom. The partial induced charges result in the alignment of pairs of water molecules and a weak bond is called a hydrogen bond. The water molecules line up and they can arrange themselves in different patterns such as those seen in the many crystal structures of water ice. Hydrates are formed due to this ability of

water to form hydrogen bonds. The hydrates are formed when the guest molecules and the host molecules are held together by van der waals force.

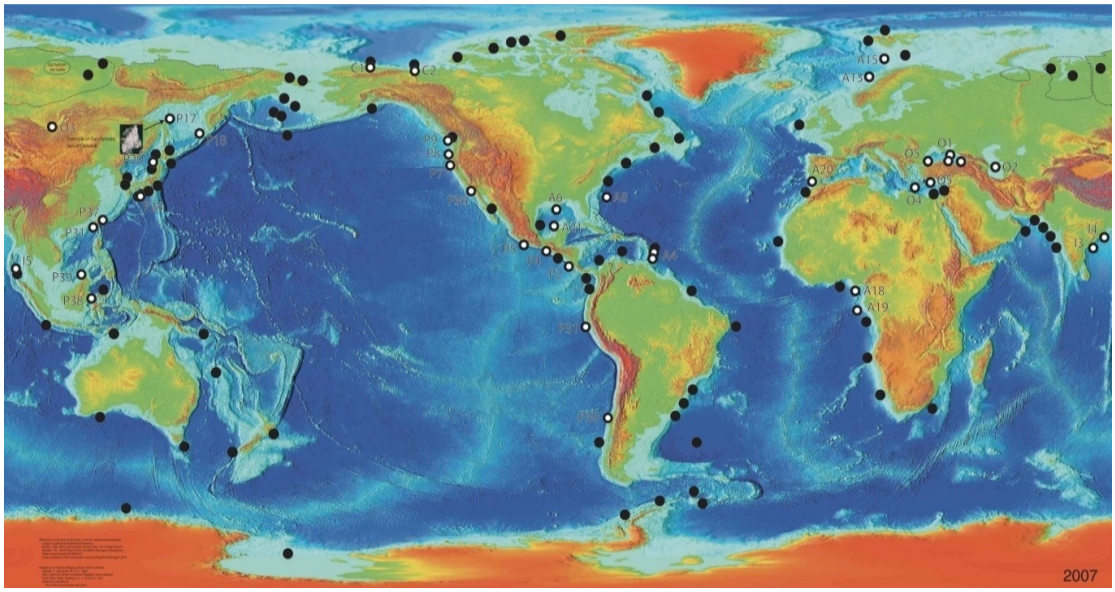

Figure 1.4 World map showing known and inferred gas hydrates. Black dots are inferred locations and white dots are places where core samples have been collected (Kvenvolden et al., 2001).

There are many different know ice structures. Common ice is hexagonal. The hydrocarbon and water forms hydrates at low temperatures and it forms three different crystal structures (Structure I, II, H) depending upon the size of the hydrocarbon. These three different crystal structures are formed by the combination of different basic cavities. The basic cavities of hydrate structures are labeled as n^m; where n are number of edges and m number of faces and are shown in Figure 1.5. The Pentagonal dodecahedron (5^{12}) has 12 pentagonal faces with equal edge lengths and angles. Tetrakaidecahedron ($5^{12}\,6^2$) has 12 pentagonal faces and two hexagonal faces and is common to SI, SII and SH. Description of different cavities like the irregular dodecahedron ($4^3 5^6 6^3$) are given in Table 1.1.

Structure I

This structure was first observed for Ethylene oxide hydrate in 1965 by MC Mullan and Jeffrey(McMullan and Jeffrey, 1965). It is a face centered cubic structure with a lattice constant

of 12 Å, formed by smaller guest molecules like CH_4, C_2H_6, CO_2 and H_2S. There are 46 water molecules arranged to accommodate 8 guest molecules of size 4-6 Å in diameter. There are two small cages of pentagonal dodecahedron and six tetrakaidecahedron. Structural composition is $8G•46H_2O$ where G is number of cages.

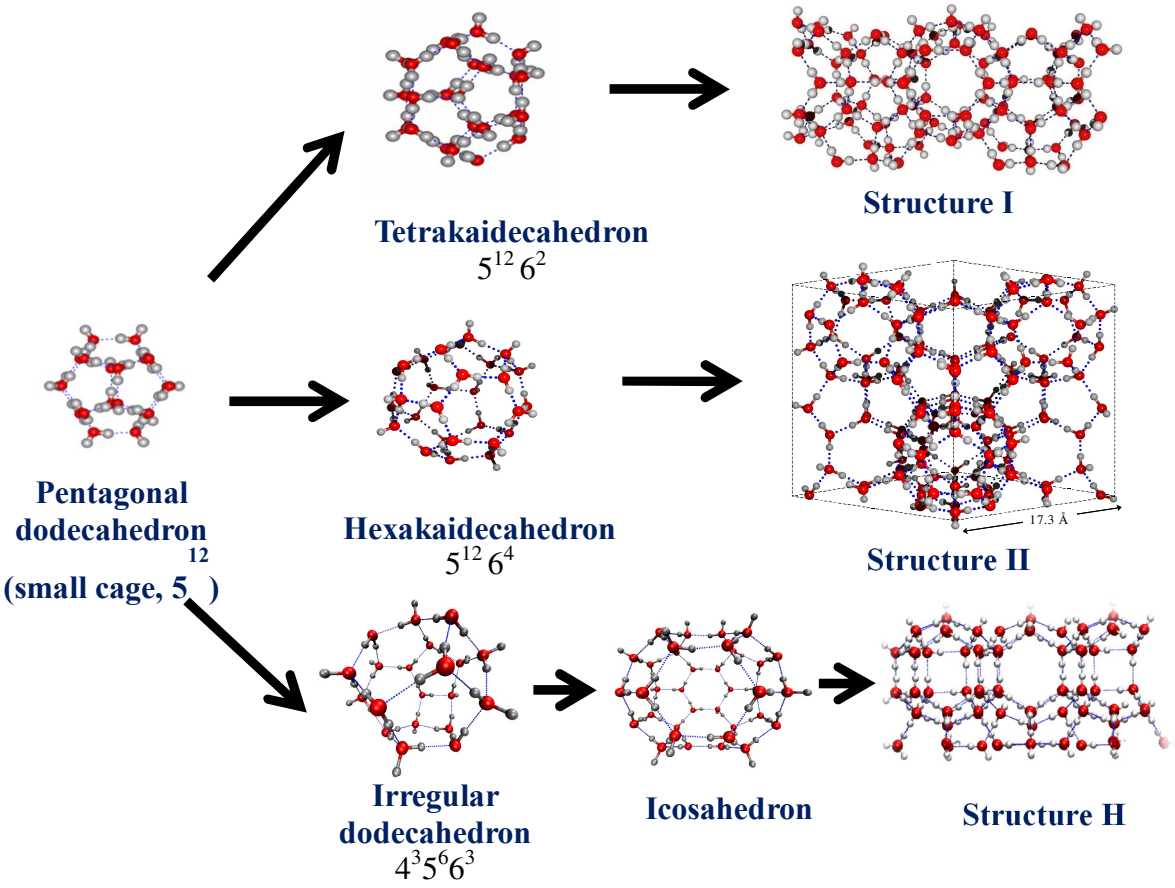

Figure 1.5 Crystal structures of clathrate hydrates.

Structure II

Structure II was observed by Mc Mullan and Jeffrey (McMullan and Jeffrey, 1965) for a H_2S hydrate in 1965. It is a face centered cubic structure which can accommodate 24 guest molecules. It has 16 small and 8 large cages with 136 water molecules per unit cell. Hydrate with

guest molecules like propane, iso-butane usually form this structure. The lattice constant is 17.3 Å, and the structural composition is 24G•136 H_2O.

Structure H

Structure H was first identified by Ripmeester (Ripmeester et al., 1987) in 1987. These crystals have one large cage that can accommodate big molecules like n-butane which has a diameter of 7.1 Å. Structure H is composed of three different types of cavities. It contains 34 water molecules associated with three 5^{12} cavity guest molecules, two $4^3 5^6 6^3$ cavity guest molecules and one $5^{12} 6^2$ cavity guest molecules.

Table 1.1 Geometry of cages

Structure	I		II		H		
Cavity	Small	Large	Small	Large	Small	Medium	Large
Description	5^{12}	$5^{12}6^2$	5^{12}	$5^{12}6^4$	5^{12}	$4^3 5^6 6^3$	$5^{12}6^8$
Number of cavities/unit cell	2	6	16	8	3	2	1
Average cavity radius(Å)	3.95	4.33	3.91	4.73	3.94	4.04	5.79
Variation in radius (%)	3.4	14.4	5.5	1.73	4.0	8.5	15.1
No. of water molecules/cavity	20	24	20	28	20	20	36

Smaller guest molecules, such as CH_4, N_2 and CO_2 occupy 5^{12} cavities, and large guest molecules such as 2-methylbutane, methylcyclopentane, methylcyclohexane, ethylcyclohexane and cyclooctane occupy $4^3 5^6 6^3$ cavities. Structure H hydrates only form if another, small molecule is present.

At high pressure it is observed that there is a transition from one structure to the other(Sloan and Koh, 2007). For example argon hydrate forms structure II and is stable at normal pressure (<30MPa). When the pressure is increased to 0.5 GPa it forms structure H.

1.3.2 Hydrate stability and physical properties

The required conditions for the hydrate to be stable are (i) low temperature (ii) high pressure, and (iii) availability of gas and water molecules. Gas hydrates are stable in ocean floor sediments at a water depth of 600 m and in permafrost regions of depth 1500 m. Figure 1.6 shows the hydrate stability zone in (a) permafrost, and (b) oceanic sediments. The red line represents geo-thermal gradient. The slopes of the red lines are different due to different thermal conductivity which effect thermal gradient. The blue phase-boundary line is pressure-temperature equilibrium curve for pure methane hydrate. Salinity and composition of gas play an important role in shifting the phase boundary line to left or right. For example, increase in salinity shifts the phase boundary curve to the left and presence of higher hydrocarbons like ethane and propane increases stability of hydrate shifting the phase boundary curve to the right. The region between the phase-boundary line and the dashed line represents the hydrate stability zone. The hydrates which are closer to the phase boundary line dissociates easily. Methane molecules are tightly packed in a lattice of water molecules due to crystallization forces. Methane hydrates has the highest energy density of any naturally occurring from of methane. Density of methane hydrate is a function of methane saturation and is approximately 0.9 g/cm^3.

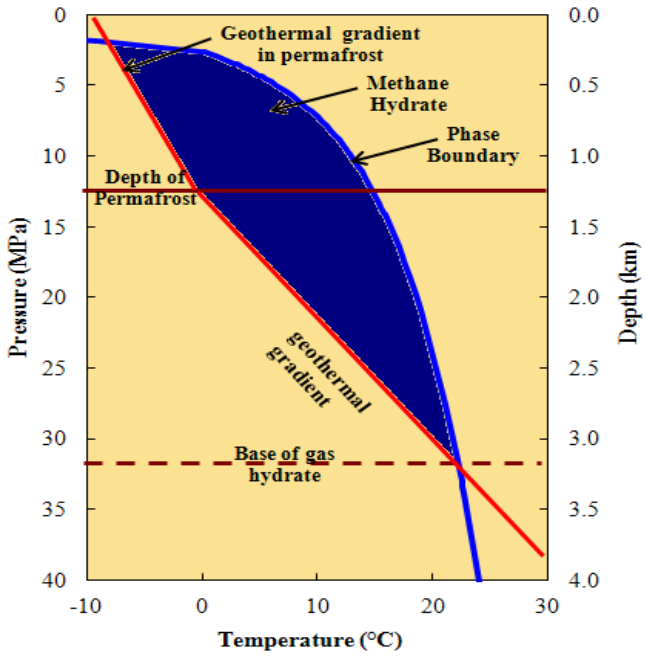

(a)

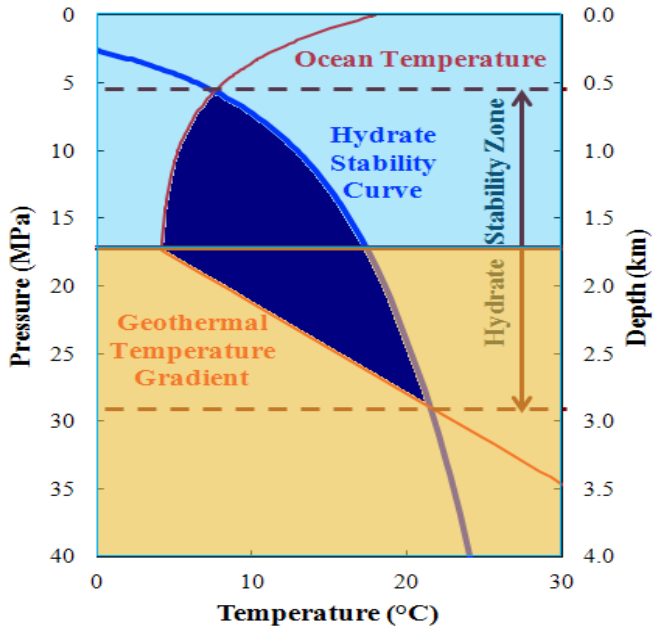

(b)

Figure 1.6 Methane hydrate stability shown in dark blue for (a) permafrost (b) ocean floor. Light blue in (b) represents marine and sand colour represents sediments. The horizontal lines at 12 MPa and 17 MPa represents depth of permafrost and ocean floor.

The heat of hydrate formation and dissociation are equal in magnitude but of opposite sign. Hydrate dissociation is an endothermic, first order reaction with an enthalpy of 51.56 kJ/gmol and activation energy of 81.084 kJ/gmol. The thermal conductivity of gas hydrate is very small (0.5 W/m-K) compared to that of ice (2.25 W/m-K). Pearson et al.(Pearson et al., 1983) demonstrated an increase in resistivity for hydrate bearing sediment relative to water saturated sediment. Through the application of Archie's law (Archie, 1942), bore hole measurements of electrical resistivity have become an important element in estimating the amount of in situ hydrate(Collett, 1998; Hyndman et al., 1999). Hydrates have a heat capacity of 257kJ/mol at constant pressure. Table 2 shows physical properties of ice and hydrate. Pressure-temperature equilibrium curve for methane hydrate is given in Figure 1.7. The quadruple point of methane hydrate is P = 2.563 MPa, T = 272.9 K.

Table 1.2 Physical Properties of Methane hydrates (Max, 2003)

Property	Ice	Hydrate
Dielectric constant at 273 K	94	58
Water molecule reorientation time at 273 K(μsec)	21	10
Isothermal Young's modulus at 268 K (109Pa)	9.5	8.4
Poisson's ratio	0.33	0.33
Bulk modulus (272 K)	8.8	5.6
Shear modulus (272 K)	3.9	2.4
Bulk density (gm/cm^3)	0.916	0.912
Adiabatic bulk compressibility at 273 K 10^{-11}Pa	12	14
Thermal Conductivity at 263 K (W/m-K)	2.25	0.49$\pm$0.02
Heat of Fusion (kJ/mol)	6	54(measured),57(calculated)

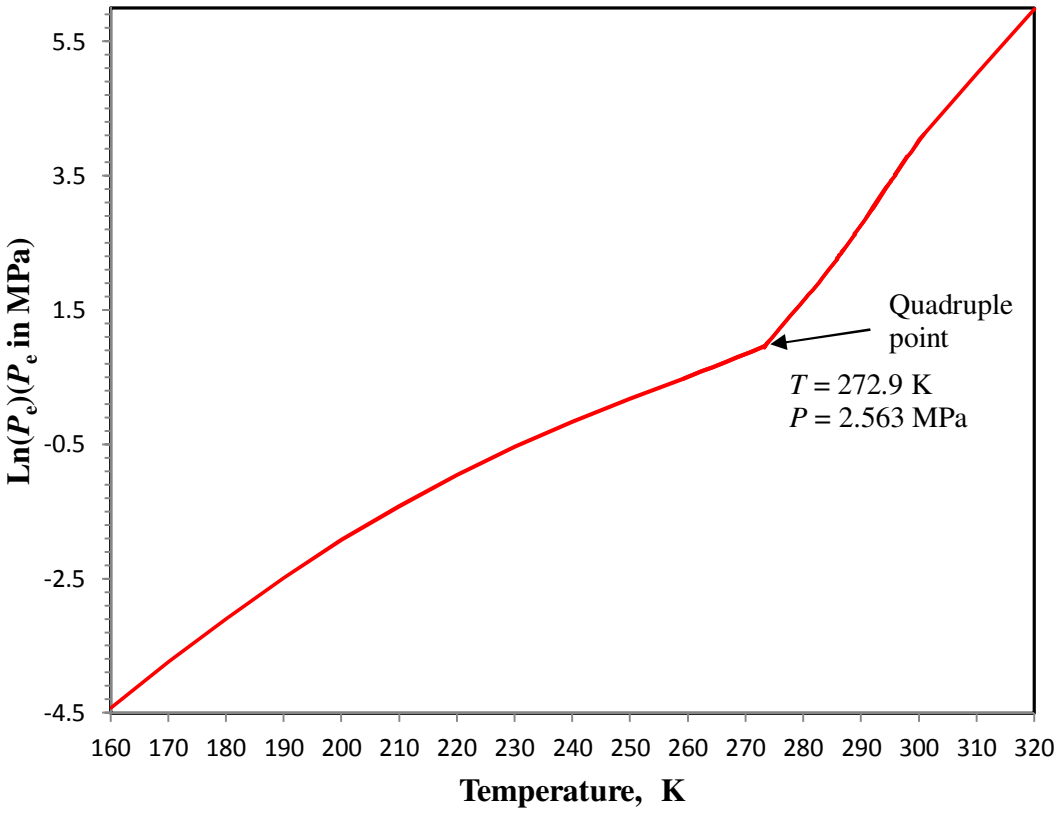

Figure 1.7 Equilibrium Pressure-Temperature relationship of methane hydrates (Moridis, 2008a)

1.4 Conventional methods for producing gas from gas hydrates

Methods of dissociation of hydrates are based on shifting the thermodynamic equilibrium of the three phase system (water-hydrate-gas). Three main methods (Moridis and Collet, 2003; Moridis and Reagan, 2007; Pooladi-Darvish, 2004) for producing gas from hydrates are Depressurization, Thermal stimulation and adding inhibitors like methanol and salts.

Depressurization

In this case, a production well is drilled into the hydrate reservoir and a pressure difference is created between the wellbore and adjacent reservoir. This pressure reduction frees the methane molecules from the hydrate. A reduction in the reservoir pressure is obtained by removing the associated free gas or formation water. Hydrate dissociates giving gas and water molecules,

which migrate towards the wellbore. Different models were developed to describe the process of hydrate decomposition in the porous media.

Thermal Injection

In this method heat is introduced into the hydrate bearing layer through an injector well. Injection wells require high pressure pumps to inject water or steam into the reservoir. The fluids injected are generally hot fluids which rises the temperature of the hydrate layer causing hydrate dissociation. Methane gases mix with hot water and return to the surface. Considering heat loses, lot of energy is being wasted to provide heat to the hydrate layer. It is not economically feasible to produce gas from this method.

Adding Chemical Inhibitors

Commonly used inhibitors are salts, alcohols and glycols. Injection of inhibitors shifts the pressure-temperature equilibrium leading to rapid dissociation of gas hydrates. In this method of production of gas from gas hydrates inhibitors are injected from the surface to the hydrate bearing sediment. When the inhibitor is added through a well, it does not necessarily come into contact with the entire hydrate bearing sediment but this process of dissociation is well accepted for an initial hydrate dissociation which is later followed by depressurization.

1.5 Geology and identification of gas hydrates

The presence of gas hydrate deposits is remotely inferred primarily on the basis of their acoustic expression. The difference in physical properties of sediments in the presence of hydrate and underlying free gas enables us to detect hydrates. The two important physical properties in this respect which enables us to detect hydrate are (i) seismic velocity and, (ii) electrical resistivity. acoustic impedance (Z) is a product of seismic wave velocity (V) and density (ρ) of rock. There are two type of seismic waves that are reflected back to the surface; Compressional wave (p-

wave), and shear wave (s-wave). There are two acoustic impedances, (i) p-impedance, and (ii) s-impedance depending on the type of wave. Reservoir characterization of gas hydrates is performed using conventional well log analysis and seismic data. The general response of well logs for a gas hydrate interval is summarized below (Collett and Ladd, 1995)

- Relatively high deflection on the resistivity log in a gas hydrate bearing sediment (HBS) compared to that of water saturated zone.
- Lower spontaneous potential deflection on a SP log for HBS compared to that of free gas zone
- Indication of oversized borehole on a caliper log
- Decrease in acoustic transit time or increase in sonic velocity in an acoustic transit time log or sonic log
- Slight increase in neutron porosity and small decrease in density on a density log

Wire line well logs of North West Eileen State-2 well Alaska are shown in Figure 1.8. Collett et al. (Collett, 1998) identified hydrate bearing sediments using gamma ray, bulk-Density, neutron-Porosity, velocity and resistivity. C, D and E are identified to be hydrate bearing sediments whereas B is identified to be water- bearing. The two methods for estimating hydrate saturation from well logs are Archie's based resistivity method (Archie, 1942), and Density-Magnetic resonance (DMR) method (Kleinberg et al., 2005; Majumder).

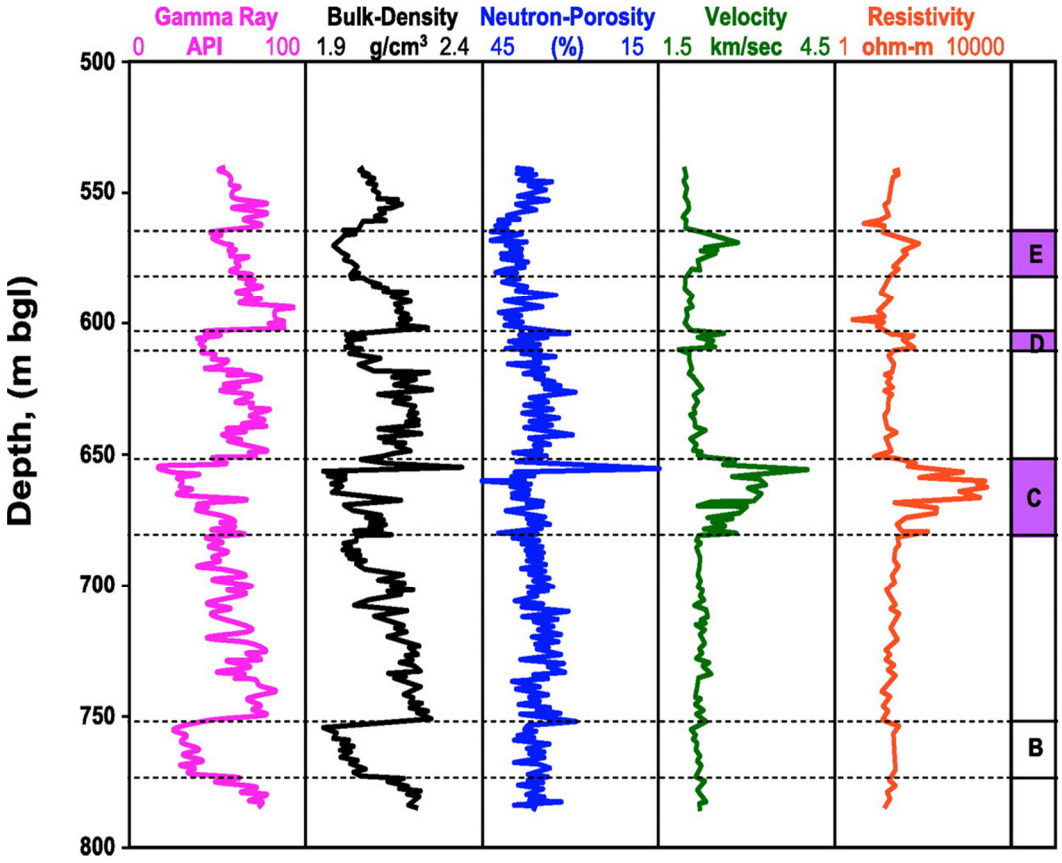

Figure 1.8 Wireline well logs from the sub-permafrost zone in the Northwest Eileen State-2 well, Alaska. C,D and E are identified to be hydrate bearing sediments. Unit B is water bearing(Collett, 1998; Worthington, 2010).

Archie's Equation for calculating water saturation is given as

$$R_t = \frac{a}{\emptyset^m} \times \frac{R_w}{{S_w}^n} \tag{2}$$

where R_t is true resistivity of the formation, $\emptyset$ is porosity, R_w is formation water resistivity, S_w is water saturation, a is constant and m, n are cementation exponents. Doug et al.(Doug, 2011) in his study has compared both methods and concluded that both methods yield similar results for known values of Archie's parameters and DMR method is the best available method for calculating hydrate saturation when one does not have enough information about Archie's parameters (cementation exponent, *m* and saturation exponent, *n*).

The indirect evidence for the presence of gas hydrates on the continental margins is inferred by identification of an anomalous reflector in the seismic data. Hydrates either occupy the pores and/or cement the sediment grains thereby increasing the acoustic velocity of the medium. The hydrate layer if is underlain by brine/free-gas saturated layer, creates impedance contrast across this interface. This contrast has special characteristics in contrast to the normal bedding planes of the sediments and owing to its parallelism to the sea floor is termed as bottom simulating reflector (BSR). Gas hydrates are found above the BSR. Gas hydrates are mostly identified by mapping bottom simulating reflectors (BSR) on seismic sections. The BSR delineates the base of the gas hydrate stability zone (BGHSZ)(Xu and Ruppel, 1999). Figure 1.9 is a seismic cross section of an offshore site in Uruguay showing BSR parallel to the sea floor. Enhanced amplitudes in Figure 1.9 below the BSR (BGHSZ) represent gas (Tomasini et al., 2010). Multiple BSR have also been recorded in many places in Gulf of Mexico and Fiord land Margin New Zealand. Figure 1.9 shows multiple BSR in the Fiord land Margin of New Zealand, One of the BSR as shown in Figure 1.9 appear to outcrop (Figure 1.10) on the sea floor. Hydrate accumulations in this region appear to be associated with slope failure (Crutchley et al., 2010)

Hydrate saturation above the base of the gas hydrate stability zone can be estimated using an indirect method called waveform inversion (Bosch et al., 2010; Shelander et al., 2010; Xu et al., 2004). In waveform inversion, seismic velocities are obtained from seismic data. Different rock physics models(Dvorkin et al., 2003; Mavko et al., 2003) are developed in the past which explains a quasi-linear relationship between hydrate saturation and seismic velocities. So, with the help of rock physics models and seismic velocities one can calculate hydrate saturation from seismic data.

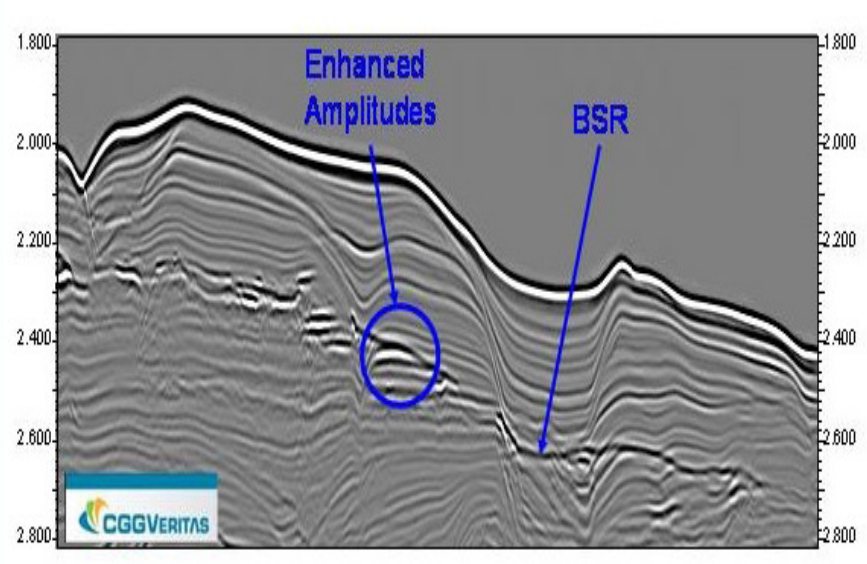

Figure 1.9 Seismic line from an offshore site in Uruguay showing BSR at 0.330 sec TWT (Two way travelling time) and enhanced amplitudes below the gas hydrate stability zone (Tomasini et al., 2010)

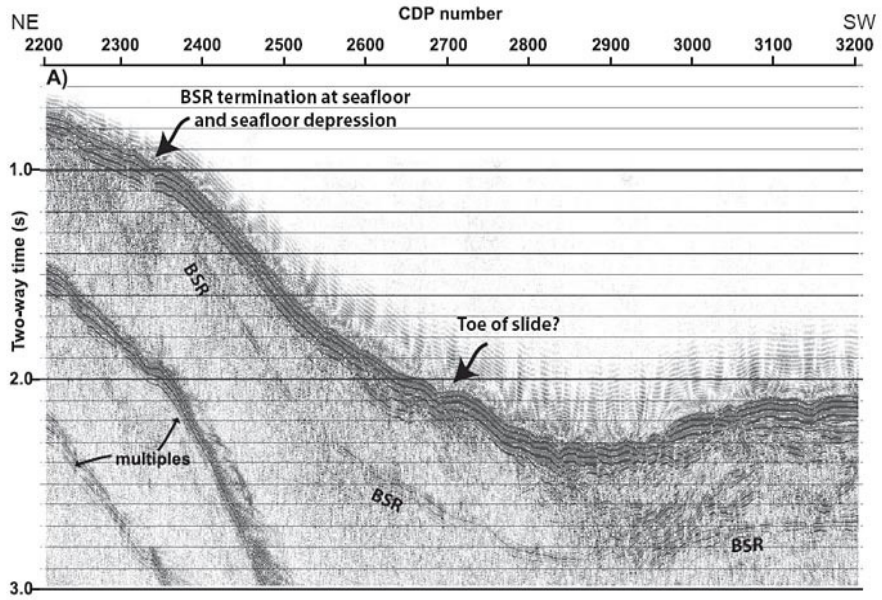

Figure 1.10 Seismic line 61C recorded in 1993 on the Fiordland margin SW of New Zealand showing multiple BSR which appears to outcrop on the sea floor (Fohrmann et al., 2007)

Figure 1.11 is a flow sheet for waveform inversion. An improvement in the resolution of velocity can be achieved by the inversion of the wavefield. Figure 1.12 represents effective medium theory model (Dai et al., 2004) showing relationship between hydrate saturation and seismic impedances.

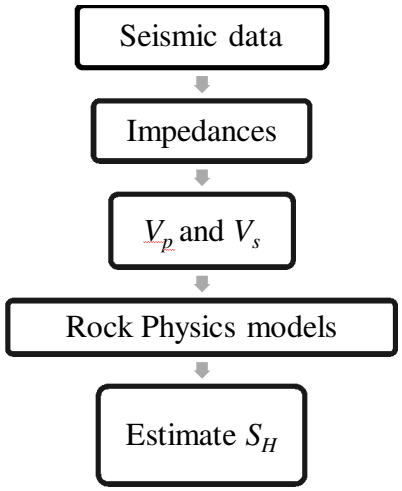

Figure 1.11 Flow sheet for estimating hydrate saturation by inversion of seismic data. Velocities and rock physics models are used to determine hydrate saturation.

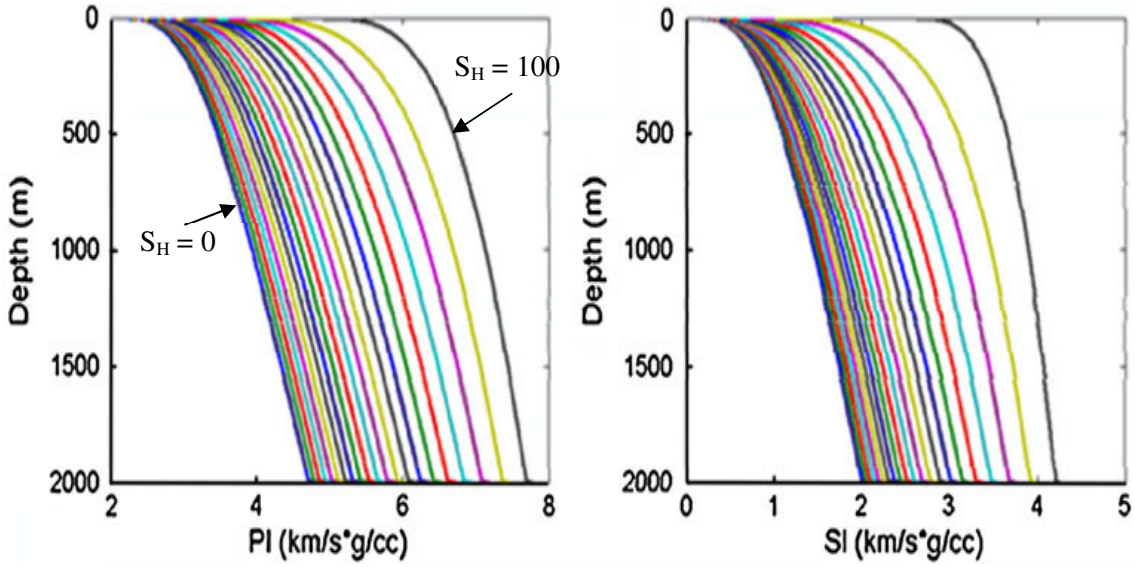

Figure 1.12 Relationship of p-wave and s-wave impedance with hydrate saturation predicted by equilibrium medium theory model. The blue line (first line from left) represents zero hydrate saturation and the black line represents 100% hydrate (Dai et al., 2004)

1.5 International effort for Code comparison of Reservoir simulators: Previous Work

In order to gain confidence in the predicted productivity of gas hydrate deposits, it is important to have a reliable model that can reliably forecast potential production scenario. To gain such confidence, it was essential that various models be studied and compared within code comparison project on an international scale. The initiative of an international comparison of

different reservoir simulators to model hydrates was been led by the National Energy Technology Laboratory (NETL) and the U.S. Geological Survey (USGS) (NETL, 2012a). The outcome of the project was expected to be the sharing of knowledge, cross validation of results of various simulators, and the acquired self-reliance for future production prediction techniques using those simulators.

The objective set for the participants of the project was to estimate the performance of different model reservoirs of varying properties subject to same reservoir parameters using different reservoir modeling programs. Different reservoir simulators used in the code comparison study were

- CMG-STARS (STARS and Guide, 2008) developed by COMPUTER MODELLING GROUP LTD.
- TOUGH+HYDRATE (Moridis, 2008a), developed at the Lawrence Berkeley National Laboratory (LBNL)
- MH-21 (MH21, 2012) Hydrate Reservoir Simulator (MH-21 HYDRES), developed by the National Institute of Advanced Industrial Science and Technology, Japan Oil Engineering Co., Ltd.
- HydrateResSim (Moridis et al., 2005a) developed at the Lawrence Berkeley National Laboratory (LBNL).
- STOMP (White and McGrail, 2006) developed by Pacific Northwest National Laboratory (PNNL).

The problems addressed in the project are called Problems 1-5, 6, and Problem 7 (a, b & c). Figure 1.13(a) is the illustration of Problems (1-5) and Figure 1.13(b) shows the results of Problem 3 confirming the consensus between different reservoir simulators participated in the

study. Problem 1 is a simple one dimensional problem with no hydrate. It is designed to validate the changes of thermodynamic properties in a reservoir.

Problem 2 & 3 have hydrate phase but different geometries of the 1-D grid. Problem 4 contains a cylindrical grid and both thermal and depressurization methods are modeled in this problem.

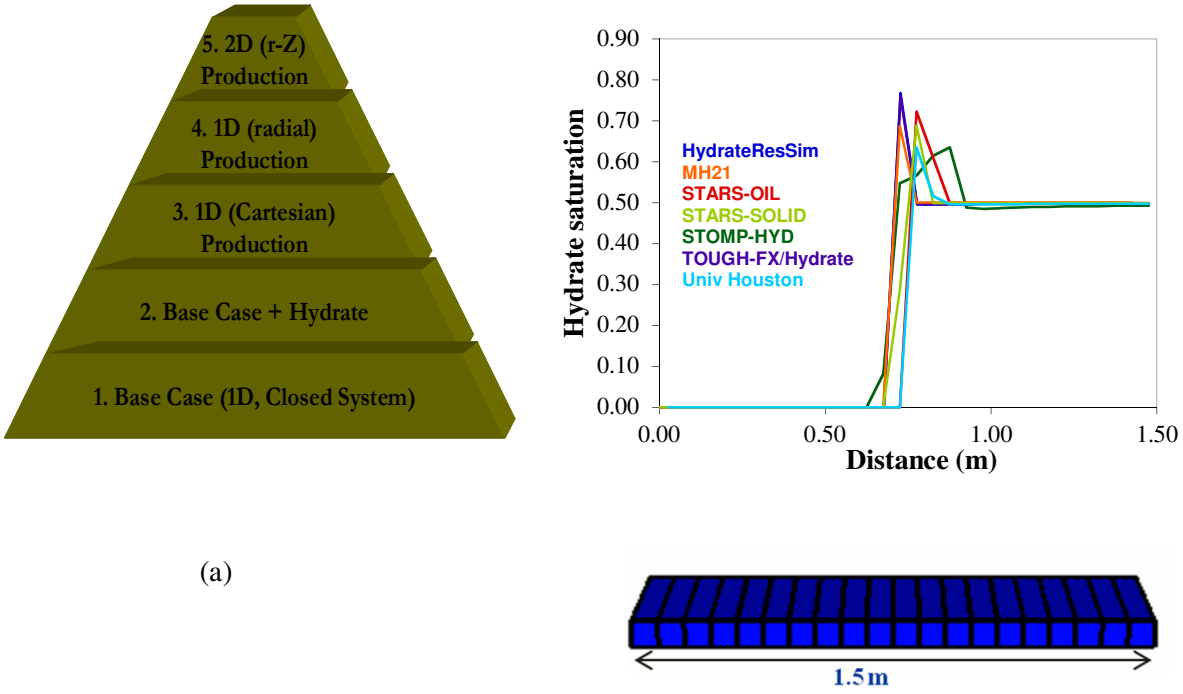

(a)

(b) Problem 3

Figure 1.13 (a) Schematic representation of code comparison problems 1-5 (b) Problem 3: Hydrate saturation profile after 5 days with decomposition front moving towards right. The peak in (b) represents hydrate formation and thus showing consensus between all reservoir simulators

Problem 5 is about a hydrate deposit in which hydrate is bound by two shale zones saturated with water. Problem 6 is based on well test data from a gas hydrate reservoir (Mt Elbert stratigraphic test well) using Schlumberger's Modular Dynamics Formation Tester (MDT) wire line tool. Four such MDT tests, ranging from six to twelve hours in duration, and including a series of flow, sampling, and shut-in periods of various durations, were conducted. The pressure and temperature were measured directly during the various flow and buildup periods of the MDT

test. The experimentally measured pressure is shown in Figure 1.14. In the first flow period as shown in Figure 1.14, the well pressure was kept above the in-situ hydrate dissociation pressure (2700 kPa).

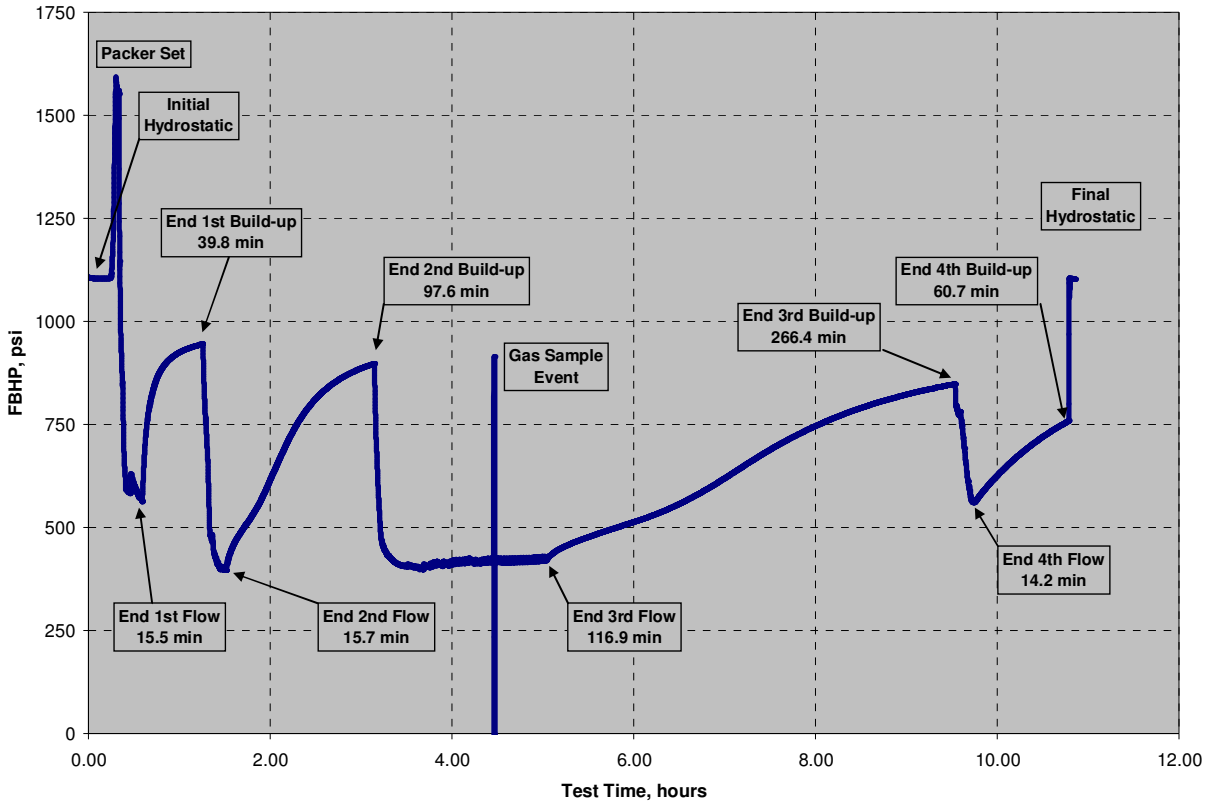

Figure 1.14 Downhole measured flowing bottom hole pressure (FBHP) for the C2 MDT experiment (Anderson et al.)

During the second and third flow periods the pressure was reduced below the expected gas hydrate equilibrium pressure, thereby resulting in hydrate dissociation and release of free gas. The prolonged pressure recovery after the second pressure drawdown indicated compressible gas in the annular space of MDT. History matches of one multi-stage; 12-h test (the C-2 test) is described as Problem 6 by the code comparison participants.

Problem 6 and the results are published in Anderson et al. (Anderson et al., 2008; Kurihara et al., 2008; Pooladi-Darvish and Hong, 2010). Figure 1.15 shows history matching results of various

reservoir simulators. The effective permeability of the formation was calculated to be in the range of 0.12 to 0.17 mD with an intrinsic permeability of 1 D. Initial efforts to history match second and third flow and build up periods were not very successful. An annular space was explicitly included around the MDT tool to account for well bore storage of reservoir fluids. After the inclusion of annular space, very good pressure matches were obtained.

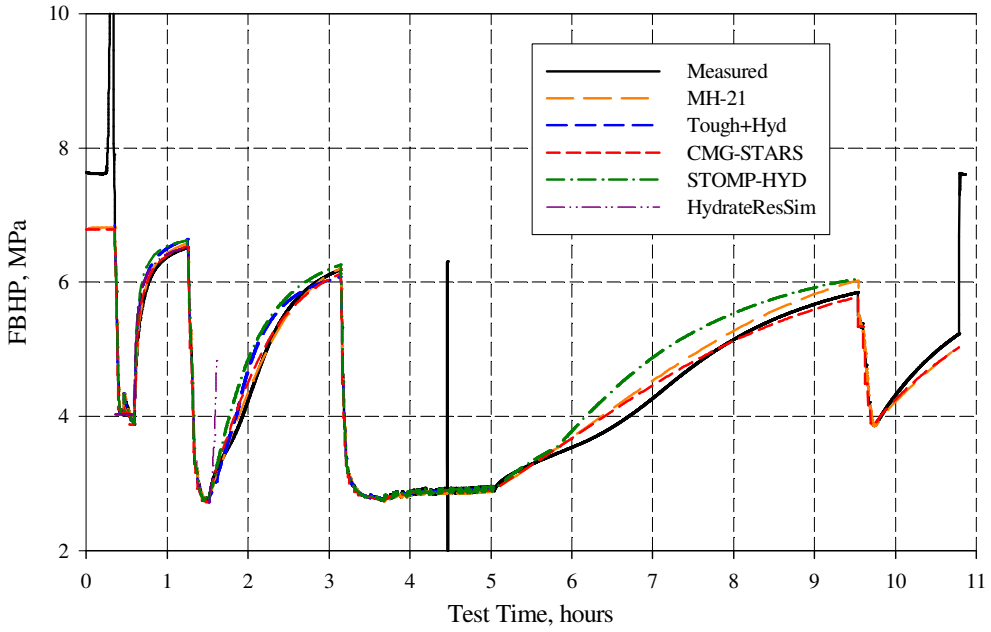

Figure 1.15 History matching of C2 MDT test, measured line is shown solid black line

Problem 7 is based on the Mt. Elbert site and data from the Prudhoe Bay L-Pad unit. A broad consensus of gas production is achieved for Problem 7(Anderson et al., 2011b; Gaddipati, 2008). A parametric study was conducted for seven most important of the several reservoir parameters using design of experiments. A Plackett-Burman (Beres and Hawkins, 2001; Plackett and Burman, 1946) design of size 8 was implemented since the number of factors was 7. The seven parameters studied were permeability, porosity, hydrate saturation, bottom-hole pressure, free water saturation, temperature and pressure.

The effects of the PB design were calculated as follows.

$$S_n = \sum_{i=0}^{20} \frac{P_i}{(1+i)^m} \tag{3}$$

where n is the number of run, S_n is the discounted cumulative gas production and P_i is annual Production and i =0.15, the interest rate used to discount the future production rate to a number that can be added to today's value to give a present value of the total production in the predicted future. Thus, $S_n s\ (S_1, S_2 \ldots S_{16})$ are calculated. The effects of the PB design were calculated using Equation (4).

$$E_j = \sum \frac{\pm S_n}{8 * \%\ change\ in\ E_j} \tag{4}$$

where j = 1, 2…7, '+' is taken before the S_n when there is a corresponding '+' in the Plackett Burman matrix column for that specific parameter and '–' is taken before the S_n when there is a corresponding '-' in the matrix column for that specific parameter. Please note that the "Design" is scenario of a different reservoir condition. The effects of various factors/parameters are plotted against those factors. A positive higher effect indicates that an increase in that factor increases the production rate and a negative effect value means that an increase in that factor decreases the production rate. The effects of all the design parameters are shown in Figure 1.16. For pressure, some effects were higher and some effects were lower than zero. This means that it depends on the other factors in the scenario.

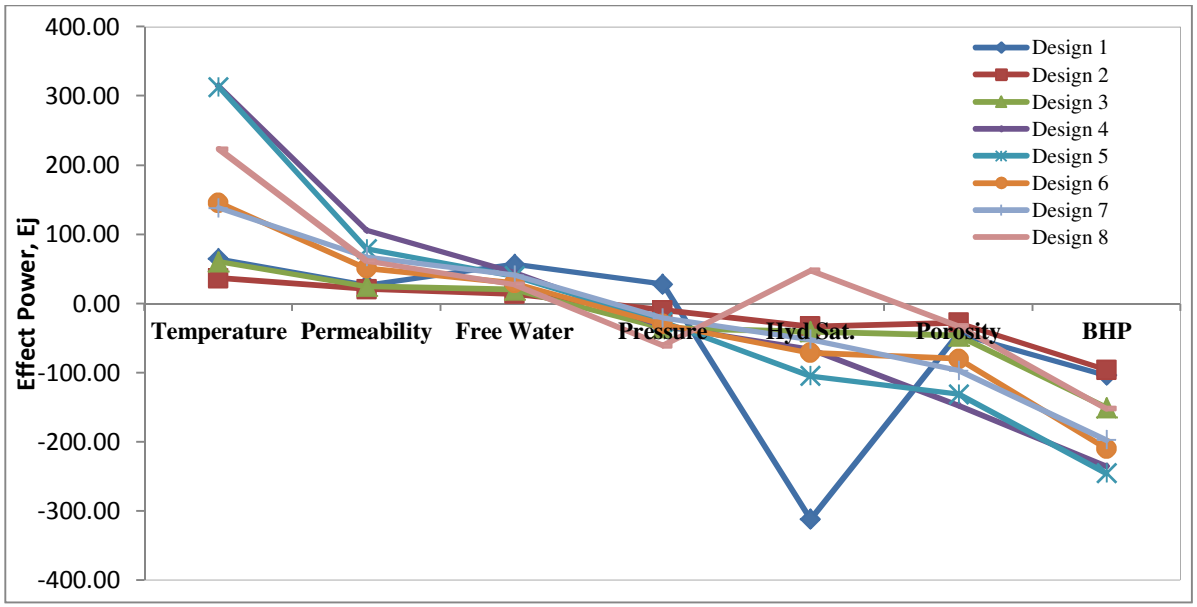

Figure 1.16 Effects of parameters on gas production.

Table 1.3 Effects of input parameters on Cumulative gas production

Design	Temp.	Perm.	Free Water	Pressure	Hyd Sat.	Porosity	BHP
1	64.66	26.71	57.03	28.26	-311.77	-44.11	-103.86
2	36.61	20.78	13.79	-9.87	-33.17	-27.68	-96.00
3	60.44	24.76	19.99	-35.11	-40.90	-46.93	-150.28
4	314.49	105.64	45.19	-32.31	-66.14	-147.40	-235.17
5	313.07	79.09	39.82	-26.64	-104.86	-131.06	-245.29
6	145.70	50.83	29.43	-29.56	-71.31	-80.28	-209.52
7	138.16	67.59	40.99	-20.70	-51.75	-96.93	-197.27
8	223.30	61.41	27.65	-60.86	47.83	-32.27	-152.03

Each of the parameters has been ranked based on the magnitude of the effect calculated. BHP was ranked the strongest in all the designs except design 8, which is warm reservoir and has less hydrate saturation. Temperature is observed to the next most important factor in determining the productivity of the reservoir.

Table 1.4 Rankings for different parameters involved in each design/scenario

Design	1	2	3	4	5	6	7	8
Pressure	6	7	5	7	7	6	7	4
Temperature	3	2	2	1	1	2	2	7
Hyd. Sat.	1	3	4	4	4	4	5	3
Permeability	7	5	6	5	5	5	4	6
BHP	2	1	1	2	2	1	1	5
Porosity	5	4	3	3	3	3	3	1
Free water	4	6	7	6	6	7	6	2

Reservoir temperature and bottom-hole pressure are found to be the most important parameters affecting gas production(Gaddipati, 2008). The effect of heterogeneity of reservoir parameters on gas production was also studied.

Important conclusions or observations that could be drawn from the code comparison project are

- A valid consensus has been achieved for all reservoir simulators in hydrate modeling for all code comparison problems, except on a problem which has ice in the system.
- Depressurization is the most economic method for gas production.
- Gas production from gas hydrate reservoirs primarily depend in initial conditions, reservoir pressure, temperature, porosity and permeability of hydrate bearing formation.
- Incorporating heterogeneities in properties like porosity, permeability, hydrate saturation, irreducible water saturation has increased production rates.
- Sensitivity analysis was performed using Placket-Burman Design and results showed that temperature, bottom-hole pressures are the most sensitive parameters. Hydrate saturations above 60% have a negative impact on production rates. Hydrate saturations of 40-50% has showed a positive impact on gas production rates.

1.6 Recent developments in the production of natural gas from gas hydrates

The first hydrate test was carried out at the Mallik field in Canada in 1972 (Max, 2003). Minor methane recovery was observed. A collaborative drilling program was carried out at Mallik field in 1998 and hydrate bearing core samples were collected for research and laboratory purposes. A high concentration of hydrate was observed as a result of this drilling program. Later, in 2002 (Dallimore and Collett, 2002), at the same field a test well was drilled and 6 days of petro-physical data was collected. That test flared gas over a short period indicating that it was actually possible to recover energy through hydrate dissociation.

In 2004, hydrate bearing sediments were recovered by drilling shallow wells at the Nankai Trough in Japan (Numasawa et al., 2008). Before this, in 1999-2000, a deep well was drilled for gas hydrates and conventional oil & gas exploration as well.

In 2006, in India, coring, drilling and down hole logging of gas hydrates was performed and samples were recovered at ten different sites in order to study the distribution, the nature of gas hydrates, the flow processes and the geological factors that control hydrate formation in marine segments (Collett and Scientific Party, 2007). Geophysical surveys and geological studies of gas hydrates in the western deep-water Ulleung basin have been carried out since 2000. A total of 23 piston cores were collected in western Ulleung basin (Ryu et al., 2009). In 2007, Korea successfully completed logging while drilling (LWD), coring and wireline logging for the 1st Ulleung basin gas hydrate expedition.

In 2007, two days of experimental-scale tests were performed at the Mt. Elbert site on the North Slope (Anderson et al., 2011a; Boswell et al., 2008; Hunter et al., 2011). Modular Dynamics Testing was performed and the flow and pressure build-up data collected indicated that gas was produced. The pressure build up data was used to calculate the permeability of the

reservoir. At the Mallik site, a collaboration of Japan and Canada conducted a 60 hour flow test which reinforced the notion that production of gas from hydrate wells was feasible. In 2008, sustained gas flow was first reported from a hydrate well at the Mallik field and it was concluded that methane gas equivalent to that of coal bed methane well was produced.

In 2009, the Gulf of Mexico (GOM) Gas Hydrates Joint-Industry-Project (JIP) Leg I and II drilling program (Collett et al., 2010; Mrozewski et al., 2010; Ruppel et al., 2008)confirmed that gas hydrate occurs at high saturations within reservoir-quality sands in the GOM. A comprehensive logging-while-drilling dataset was collected from seven wells at three sites. In February 2012, US DOE and Conoco Phillips conducted (NETL, 2012b) Ignik Sikumi gas hydrate field trial for CO_2-CH_4 exchange. A mixture of CO_2 and N_2 is injected into a gas hydrate reservoir which is then followed by gas production through depressurization. The objective of the project is to sequester CO_2 followed by CH_4 gas production. The economic viability of gas production from hydrates is not yet established but the tests are conducted to get an insight into technical feasibility of gas hydrates.

1.8 Introduction to CMG STARS reservoir simulator

The Computer Modeling Group's Steam Thermal Adaptive Reservoir Simulator (CMG STARS) (STARS and Guide, 2008) is a commercial reservoir simulator used for flow simulations. STARS is designed to simulate a variety of complex oil field production and enhancement processes. STARS have been modified to accommodate the properties of hydrate. Hydrate can be specified by the user as an oil component with a high viscosity. Hydrate dissociation and formation are specified by equilibrium kinetics. Comparison between equilibrium and kinetic models for methane hydrate dissociation was done previously by Kowalsky et al. (Kowalsky and Moridis, 2007) and Gamwo et al. (Gamwo and Liu, 2010). Kowalsky et al. concluded that the

dissociation behavior was indistinguishable using both models. Gamwo et al. found significant deviations for both models and recommended complex kinetic models for flow simulations. The equilibrium model exhibits a moving front pattern for hydrate dissociation while the kinetic model shows a moving zone pattern under adiabatic conditions. As for the constant temperature boundary condition, the hydrate dissociates by shrinking in all dimensions for the equilibrium model while, for the kinetic model, hydrate dissociates with no specific pattern throughout the reservoir. Hydrate dissociation is an endothermic, first order reaction with an enthalpy of ~51 kJ/gmol and activation energy of approximately 81 kJ/gmol(Kim et al., 1987; Moridis et al., 2005b).

Hydrate dissociation rate is given in Equation (5).

$$-\frac{dn_H}{dt} = \frac{k_d^0 A_{SH} a}{\rho_w \rho_H} \exp\left(-\frac{E - bR}{RT}\right) (\varphi S_w \rho_w) (\varphi S_H \rho_H)\left(1 - {}^1/_K\right) \quad (5)$$

where k_d^0 is dissociation rate constant, A_{SH} is the specific area, ρ_w, ρ_H are the densities of water and methane hydrate, φ is porosity of the porous media, S_w and S_H are saturations of water and hydrate, E is the activation energy, a, b are constants obtained from equilibrium data of methane hydrate and K is the equilibrium constant. Please note that a term EACT ($E - bR$) is used to denote activation energy of methane hydrate in the later part of the thesis.

The gas hydrate in this study is a pure methane hydrate with a hydration number (N_H in Equation 1) of 6.176. A fully coupled mechanistic, discretized wellbore (DW) model is used, which treats each section of a wellbore as a grid block so the wellbore equations and reservoir flow equations can be coupled (STARS and Guide, 2008) . The DW model has a finite conductivity which allows accurate calculation of the frictional pressure drop and wellbore

hydraulics. The pipe flow equations used for a wellbore are transformed into Darcy's equations used to estimate flow through porous media. All wellbore properties are converted into equivalent reservoir properties like permeability, porosity, and heat capacity used in the porous media flow equations.

1.8.1 Conservation Equations

A conservation equation is constructed for each component of a set of identifiable chemical components that completely describes all the fluids of interest. The change in the amount of component i within the elementary volume is a result of fluid leaving and entering the elementary volume as given in Equation (6).

$$Rate\ of\ accumulation = Net\ rate\ of\ inflow\ from\ adjacent\ regions + Net\ rate\ of\ addition\ from\ sources\ and\ sinks \quad (6)$$

Total volume (V) of a grid block is given as Equation (7)

$$V = V_r + V_f \quad (7)$$

Where, V_r is rock volume and V_f is fluid volume given by Equation (8)

$$V_f = V_0 + V_w + V_g \quad (8)$$

Where subscripts o, w, g represents oil, water and gas

Fluid porosity is defined as in Equation (9)

$$\varphi_f = V_f / V \quad (9)$$

The saturations ($S_{w,o,g}$) are defined as

$$S_{w,o,g} = V_{w,o,g} / V_f \quad (10)$$

The accumulation term for flowing component I is

$$V\frac{\partial}{\partial t}\left[\varphi_f(\rho_w S_w w_i + \rho_o S_o x_i + \rho_g S_g y_i\right] \quad (11)$$

The accumulation term for energy is

$$V\frac{\partial}{\partial t}\left[\varphi_f(\rho_w S_w U_w + \rho_o S_o U_o + \rho_g S_g U_g + \left(1-\varphi_f\right)U_r\right] \quad (12)$$

where, $U_{w,o,g}$ is the internal energy as a function of temperature and phase composition, $\rho_{w,o,g}$ is fluid phase densities. U_r is the energy per rock volume. w_i,x_i,y_i are water oil and gas phase mole fractions respectively.

The flow term of flowing component I between two regions is given in Equation (13)

$$\rho_w v_w w_i + \rho_o v_o x_i + \rho_g v_g y_i + \varphi\rho_w D_{wi}\Delta w_i + \varphi\rho_g D_{gi}\Delta y_i + \varphi\rho_o D_{oi}\Delta x_i \quad (13)$$

Where, $v_{w,o,g}$ is volumetric flow rate defined by Equation (14).D_{wi}, D_{gi}, D_{oi} are the component dispersibilities in three phases (water, gas and oil).

$$v_j = T\left(\frac{k_{rj}}{\mu_j r_j}\right)\Delta\emptyset_j, j = w, o, g \quad (14)$$

Where $T\left(\frac{k_{rj}}{\mu_j r_j}\right)$ is the phase transmissibility between two regions, accounting for the cross sectional area, node spacing, as well as the permeability at the interface. The potential difference $\Delta\emptyset_j$ is the value at the node of the adjacent region minus the value at the node of the current region of interest. A positive value of $\Delta\emptyset_j$ represents inflow, a negative value represents outflow. The concentration differences Δw_i, Δy_i, Δx_i are the differences in phase concentrations between the nodes.

The flow term of energy between two regions is defined as Equation (15)

$$\rho_w v_w H_w + \rho_o v_o H_o + \rho_g v_g H_g + K\Delta T \quad (15)$$

Where H is the enthalpy of the phase. K is the thermal transmissibility at the interface between two regions and ΔT is the temperature drop between the nodes.

Well source/sink terms are the means by which all process are driven. Well source/sink terms for flowing component I is defined as shown in Equation (16).

$$\rho_w q_{wk} w_i + \rho_o q_{ok} x_i + \rho_g q_{gk} y_i \tag{16}$$

where q_{wk}, q_{ok}, q_{gk} are well phase rates defined by Equation (17), and k is layer number.

$$q_{jk} = I_{jk}\left(p_{wfk} - p_k\right), j = w, o, g \tag{17}$$

Where I_{jk} is the phase index which is a function of geometry, skin factor, permeability and layer thickness. p_{wfk} is the flowing wellbore pressure in well layer k and p_k is the node pressure of region of interest.

Well source/sink term for energy is given in Equation (18).

$$\rho_w q_{wk} H_w + \rho_o q_{ok} H_o + \rho_g q_{gk} H_g \tag{18}$$

The chemical reaction term for component I is shown in Equation (19).

$$V \sum_{k=1}^{n_r} (s'_{ki} - s_{ki}) r_k \tag{19}$$

Where s'_{ki} and s_{ki} are the product and reactant stoichiometric coefficient of component I in reaction k respectively. r_k is the volumetric rate of reaction k calculated from reaction kinetics.

The reaction source/sink term for energy is given in Equation in (20).

$$V \sum_{k=1}^{n_r} H_{rk} r_k \tag{20}$$

Where H_{rk} is the enthalpy of reaction k

The spatially discretized conservation equation of flowing component I and energy is obtained by combining Equations (6-20) as shown in Equation 21 and 22 respectively.

$$V\frac{\partial}{\partial t}\left[\varphi_f(\rho_w S_w w_i + \rho_o S_o x_i + \rho_g S_g y_i\right]$$

$$= \sum_{k=1}^{n_f}[\rho_w T_w w_i \Delta\emptyset_w + \rho_o T_o x_i \Delta\emptyset_o + \rho_g T_g y_i\, \Delta\emptyset_g] + V\sum_{k=1}^{n_r}\left(s'_{ki} - s_{ki}\right)r_k$$

$$+ \sum_{k=1}^{n_f}\left[\varphi\rho_w D_{wi}\Delta w_i + \varphi\rho_g D_{gi}\Delta y_i + \varphi\rho_o D_{oi}\Delta x_i\right] + [\,\rho_w q_{wk} w_i + \rho_o q_{ok} x_i$$

$$+ \rho_g q_{gk} y_i] \qquad (21)$$

$$V\frac{\partial}{\partial t}\left[\varphi_f(\rho_w S_w U_w + \rho_o S_o U_o + \rho_g S_g U_g + \left(1-\varphi_f\right)U_r\right]$$

$$= \sum_{k=1}^{n_f}[\rho_w T_w H_w \Delta\emptyset_w + \rho_o T_o H_o \Delta\emptyset_o + \rho_g T_g H_g\, \Delta\emptyset_g] + \sum_{k=1}^{n_f} K\Delta T + \rho_w q_{wk} H_w$$

$$+ \rho_o q_{ok} H_o + \rho_g q_{gk} H_g + V\sum_{k=1}^{n_r} H_{rk} r_k + HL \qquad (22)$$

For three component system a total of five equations (3 component conservation equation, Energy conservation equation and phase constraint equation) are solved simultaneously for each grid block. The equations summarized in Equation 21 and 22 are written in residual form as shown in Equation (23). Evaluation of residuals amounts to calculation of all terms in Equation (21 and 22).

$$R_i = [net\ inflow\ rate] + [net\ \ source/sink\ \ rate] - [rate\ of\ change\ of\ Accumulation] \qquad (23)$$

The total number of equations solved depends on the number of grid blocks and no of wells. Let N represents the total number of primary variables and X_i represents all primary variables, with i =1 to N. Each residual depends on primary variable. Advancing the solution over one time step consists of solving $R(X) = 0$. This is accomplished using Newton's method as shown in Equation (24)

$$X^{k+1} = X^k - [J^k]^{-1} \cdot R^k \tag{24}$$

Where $J^k = dR/dX$ is the Jacobian matrix of derivatives and k is the Newton iteration number. The entries of the Jacobian matrix corresponding to unconnected grid blocks and wells are zero making it a banded sparse matrix. An example of a sparse matrix of 3×5 ($i \times j$) grid is shown in Figure 1.18. Figure 1.17 shows a naturally ordered 3×5 grid system. The sparse matrix in Figure 1.18 shows grid connections. For example grid block number 3 is connected to blocks 2 and 6 as shown in yellow shaded regions of Figure 1.17. The diagonal elements are shown in grey shaded solid black dots. The rest of the entries in the sparse matrix are zero. The iterative process is considered converged when both $\left(X^{k+1} - X^k\right)$ and R (Reesidual) are sufficiently small.

1	2	3
4	5	6
7	8	9
10	11	12
13	14	15

Figure 1.17 Naturally ordered 3×5 grid system

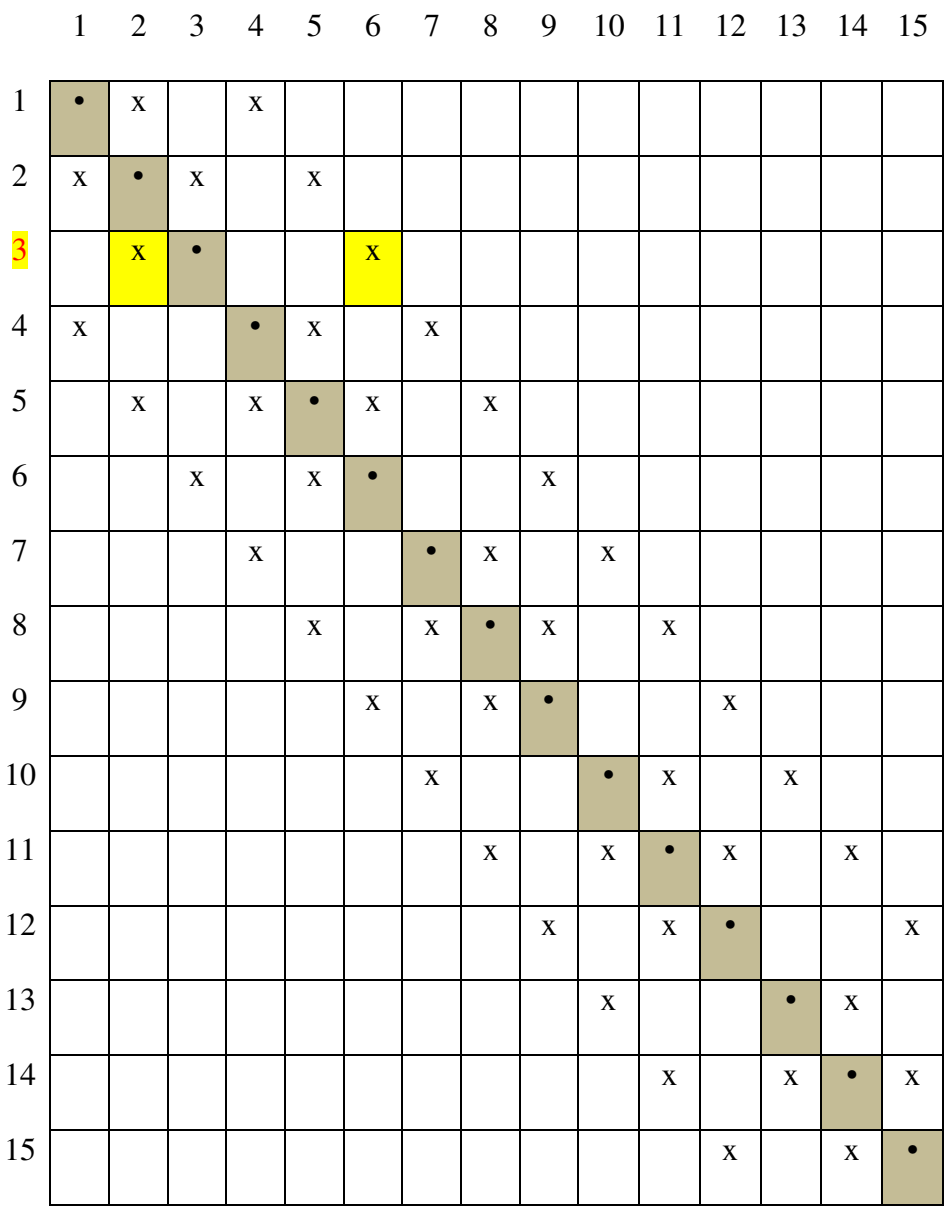

Figure 1.18 Sparse matrix showing grid connections of 3×5 grid system. Grey shaded regions are diagonal elements and yellow shaded entries shows grid connection of Block 3.

2. Summary

The problem description and objectives of each chapter are different from each other and are explained in detail in the following chapters.

Chapter 3 deals with the uncertainty assessment of gas production of upper and lower C hydrate sands of Prudhoe Bay L-Pad site. Uncertainty propagation in gas production is studied using a Latin hypercube sampling of porosity permeability, bottom hole pressure and hydrate reaction kinetics as uncertain parameters.

In Chapter 4 gas production of horizontal well, deviated well to vertical well for Prudhoe Bay L-Pad site are compared. A mechanistic model is used to incorporate pressure drop for horizontal wells.

The production potential of Walker Ridge 313 site Gulf of Mexico is estimated using 3-D reservoir models and is elaborated in Chapter 5. The gas production from two wells WR 313 G and WR 313 H is simulated by depressurization at constant pressure. Uncertainty assessment of gas production from WR 313 G well will be performed.

Geomechanical modeling of thermal disturbance caused due to a hot well bore in hydrate bearing formation is presented in chapter 6. A sensitivity study is be conducted to understand the effect of reservoir parameters on subsidence and volumetric strain.

3. Uncertainty assessment of gas production from Prudhoe Bay L-pad site

The objective of this study is to estimate the uncertainty in gas production of upper and lower C hydrate deposits of Prudhoe Bay L-Pad site that could arise from the uncertainty in the reservoir parameters. The base case for this uncertainty assessment is adapted from Problem 7b of the Code comparison project(Anderson et al., 2011b; Gaddipati, 2008). Problem 7b of the code comparison project is a much simpler problem with homogenous properties like hydrate saturation, porosity. It has been unanimously observed by hydrate researchers that incorporating heterogeneity in the reservoir model increases gas production (Anderson et al., 2011b; Gaddipati, 2008; Reagan, 2010). A base model is constructed incorporating heterogeneity to Problem 7b. Uncertainty propagation can be studied using a variety of methods, the most popular being a Monte-Carlo procedure.

Schematic representation uncertainty propagation in a Monte Carlo simulation is shown in Figure 3.1.

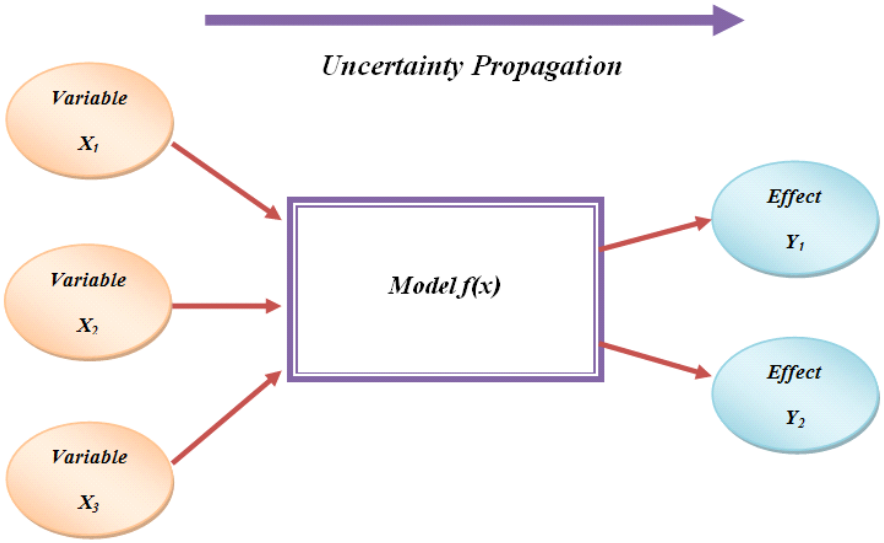

Figure 3.1 Schematic of uncertainty propagation in Monte-carlo analysis

A Monte Carlo study was performed to understand the behavior of the reservoir model and to gain perspectives on the most important variables with respect to uncertainty in gas production. Once system behavior is understood and the more important variables are identified, resources can be focused on improving the characterization of the uncertainty in these important variables. The other methods are Differential analysis, response surface methodology (RSM), the Fourier amplitude sensitivity test (FAST), Sobol variance decomposition and fast probability integration (FPI)(Helton and Davis, 2003; McKay et al., 1979). The desirable features of a Monte Carlo approach are (i) extensive sampling of uncertain variables (ii) results are obtained without a surrogate model which is an approximation of the original reservoir model and (iii) ease of implementation. The major drawback of a Monte Carlo procedure is the computation cost; however this can be reduced by using a Latin hyper cube sampling(Helton and Davis, 2003). Latin hypercube sampling does not require more samples for more dimensions; this independence is the main advantage and therefore used in this study.

3.1 Introduction to Latin hypercube sampling

Latin hypercube sampling is a widely used technique for the propagation of uncertainty analysis for a complex system. The Latin hyper cube sampling is a process applied for multiple variables to reduce the number of required simulations necessary for a Monte-Carlo simulation. In Latin hypercube sampling, each of the parameter can have any number of sample values. The sample values can be evenly distributed (Uniform distribution) or from a normal distribution. The sample values are combined to create job patterns. For the first simulation run in the job pattern each parameter is selected randomly from a known probability distribution function. The parameters for the second run are selected excluding the values used in the first run. This procedure is repeated to generate a job pattern for the sampling. In this study sensitivity analysis

is conducted by inputting reservoir properties from a pre-determined range of values with a specific mean and standard deviation. These statistics of the input variables are adapted from the well data and the range is decided by engineering judgment. Bottom-hole pressure, permeability, Hydrate reaction kinetics and porosity are the uncertain parameters in this study. The presence of higher hydrocarbons like ethane and propane will increase the stability of hydrate while increase in salinity will reduce the stability. To keep track of uncertainty in hydrate stability the parameters of reaction kinetics are altered and its effect on gas production is studied. Hydrate saturation, reservoir pressure, temperature and lithology which are specific to the Prudhoe Bay hydrate deposit are not treated as uncertain parameters due to limited available data.

3.2 Base case model (PBU L Pad)

The base case problem originates from Prudhoe Bay L-Pad 106 well in Alaska. The geographical location is shown in Figure 3.2. The base case problem is adapted from the International Methane Hydrate Code Comparison Project(Problem 7b)(Gaddipati, 2008).

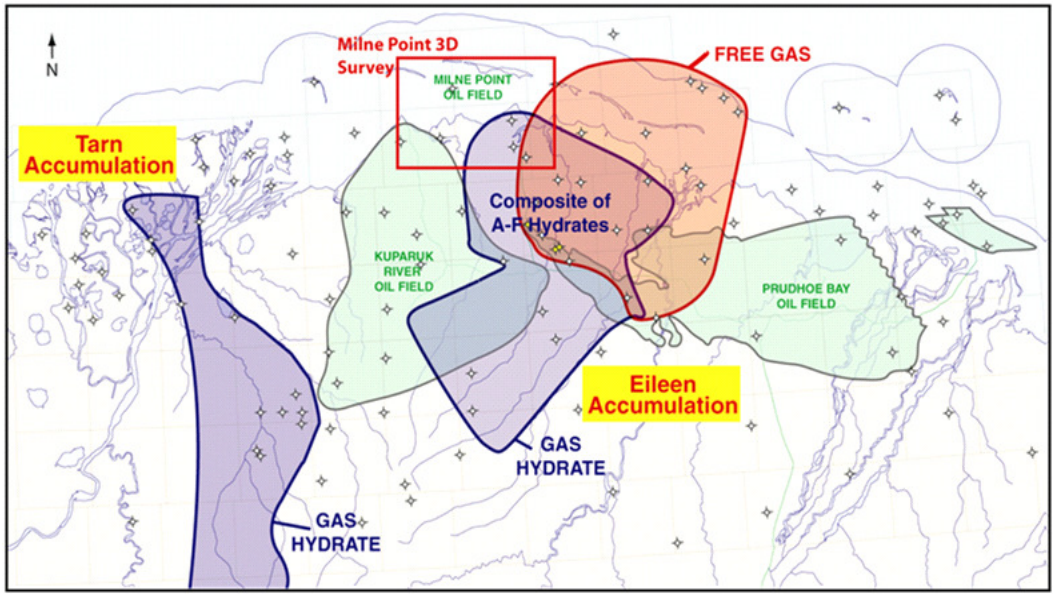

Figure 3.2 Gas hydrate deposits in North Slope of Alaska

A radial grid of outer radius 450 m and 240 m deep is considered in this problem. A schematic view of the grid is shown in Figure 3.3.The hydrate bearing zones (H1 & H2) and the shale layer between them (S2) are uniformly discretized and the upper and lower shale zones are logarithmically discretized. The porosity and saturations of hydrate bearing sediments are obtained from well log data of PBU L-106. Impermeable shale boundary of the hydrate layers is considered in this base model. The top of hydrate bearing zone (H1) is 62 m below the top of the hydrate bearing zone. Pressure temperature of the hydrate bearing zone are 7.327 MPa and 278.15 K.

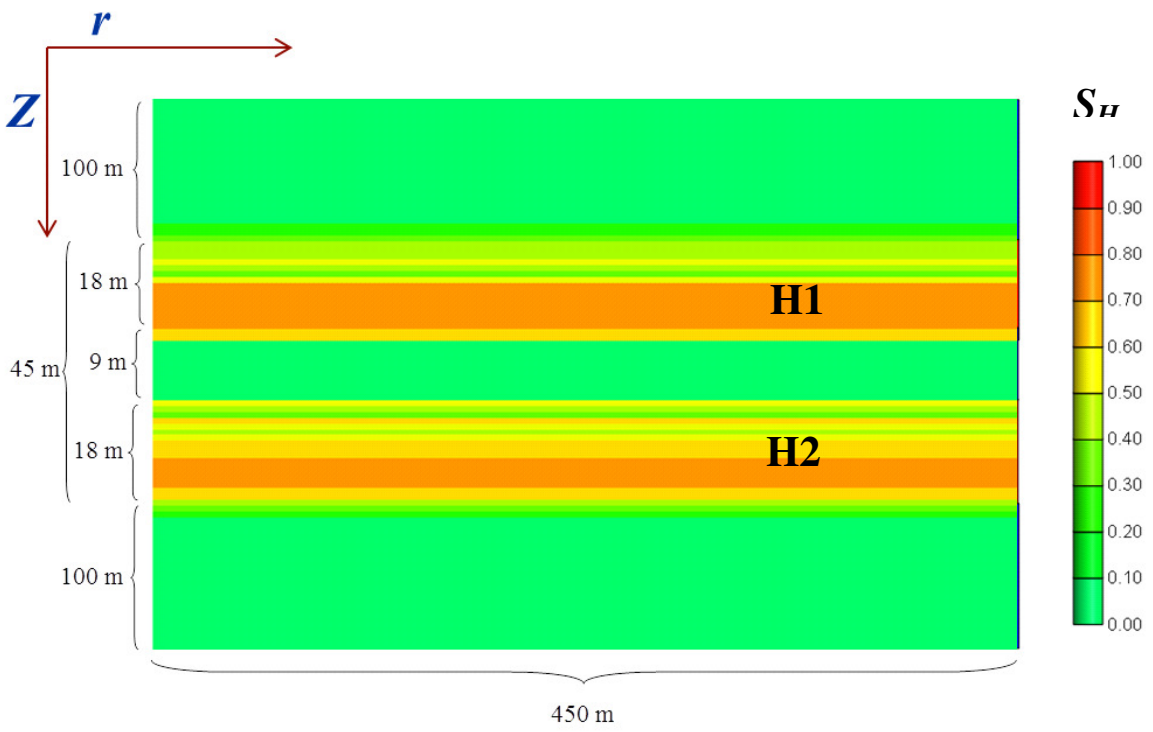

Figure 3.3 Schematic representation of the base model

Pressure and temperature values for each layer are calculated using a hydrostatic pressure gradient of 9792 Pa/m and geothermal gradient of 3°C/100 m.

There is no net mass transport between the reservoir and the surroundings. The upper boundary temperature is held constant at 275.15 K and the lower boundary temperature is held at constant at 282.50 K.

The van Genuchten (Equation 25) (Van Genuchten, 1980) capillary pressure model is used to express the relationship between gas aqueous capillary pressure head and the aqueous saturation:

$$\overline{s}_l = \frac{(S_l - S_{lr})}{(1 - S_{lr})} = \left(1 - \left(\alpha\beta_{gl}\left(\frac{P_g - P_l}{\rho_l g}\right)\right)^n\right)^m \tag{25}$$

and the modified Stone three-phase model (Equation 26 and 27) (Aziz and Settari, 1979; Stone, 1970) is used for calculating relative permeabilities

$$K_{rl} = (\bar{s}_l)^n, K_{rG} = (\bar{s}_l)^m \tag{26}$$

$$\bar{s}_l = \frac{(S_l - S_{lr})}{(1 - S_{lr})}\ \bar{s}_g = \frac{(S_G - S_{irG})}{(1 - S_{irG})} \tag{27}$$

where $\overline{s}_l$ is effective aqueous saturation, $\bar{s}_g$ is effective gas saturation, S_l is aqueous saturation, S_{lr} is irreducible aqueous saturation, $\alpha, \beta_{gl}\ n, m$ are reference parameters. k_{rl} is aqueous relative permeability. k_{rG} is gas relative permeability. The values of reference parameters are listed in Table 3.1. The simulations are carried out in CMG STARS for a time period of 50 years. Data for gas production rate, water production rate, cumulative gas production and cumulative water production is recorded with a frequency of 90 days for 50 years.

Table 3.1 Reservoir properties and reference parameters for the base model

Property	Value/Source
Hydrate bearing sediment (HBS) - saturations	Derived from well logs using Archie's Equation
Permeability-HBS	1000 mD horizontal , 100 mD vertical
Average Porosity of HBS	0.4
Shale layer – Porosity	0.0
Rock Density	2600 kg/m^3
Rock Specific cheat	1000 J/kg K
Dry Thermal Conductivity	2.0 W/m K
Pore Compressibility	10^{-9} Pa^{-1}
Composite Thermal Conductivity Model	linear
Capillary Pressure Model	Van Genuchten Equation – Equation 25
α	10.204 (m^{-1})
β_{gl}	1
S_{lr}	0.28
n	4.432
m	0.7744
Aqueous Relative Permeability Model	Stone + Aziz – Equation 26,27
S_{irA}	0.2
n	4.20
Gas Relative Permeability Model	Stone + Aziz – Equation 26,27
S_{irG}	0.02
n	3.16

Results: The reservoir was depressurized to a bottom hole pressure of 2.7 MPa for a period of 50 years. Figure 3.4 shows gas rate and cumulative gas production of the base model. The gas production started instantaneously without any lag. The gas production reached a maximum of 1200 Mscf/day in 9 years and gradually decreased to 225 Mscf/day at the end of 50 years. Cumulative gas produced from the simulation was 9 Bscf at the end of 50 years as shown in Figure 3.4. The reservoir started producing water due to depressurization instantaneously and reached a maximum of 2600 (Standard barrels/day) STB/day in 1 year. Cumulative water production at the end of 50 years is 12 MMSTB as shown in Figure 3.5.

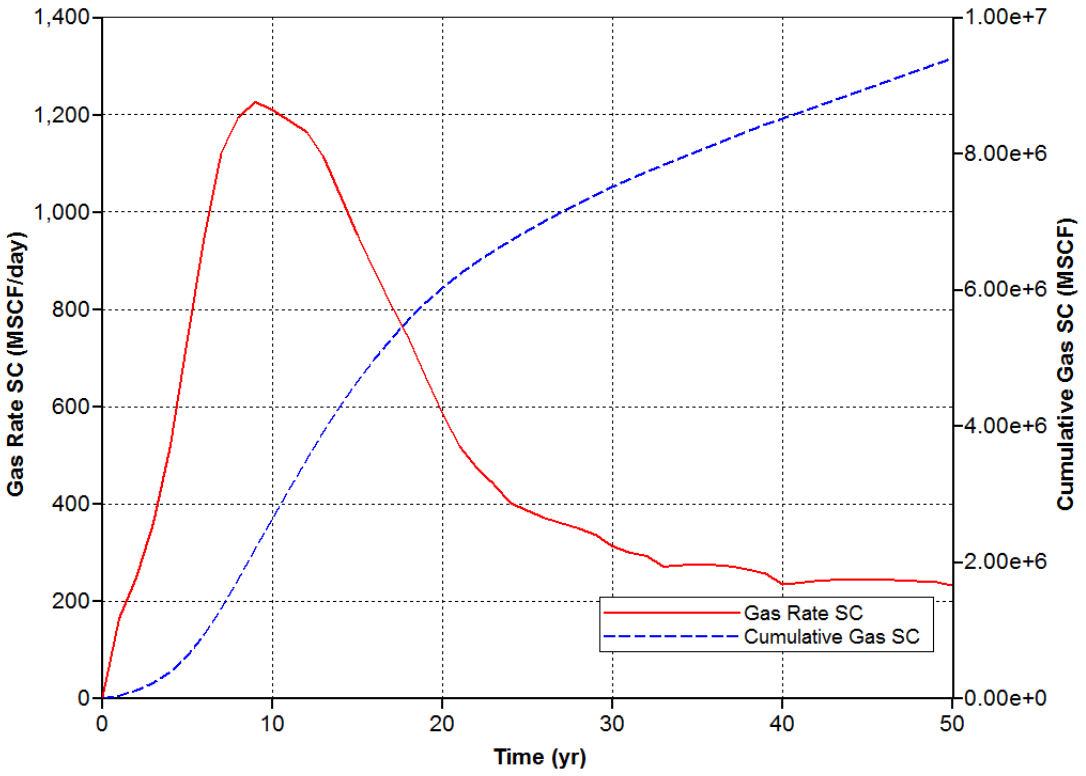

Figure 3.4 Gas rates and Cumulative gas production of the base model.

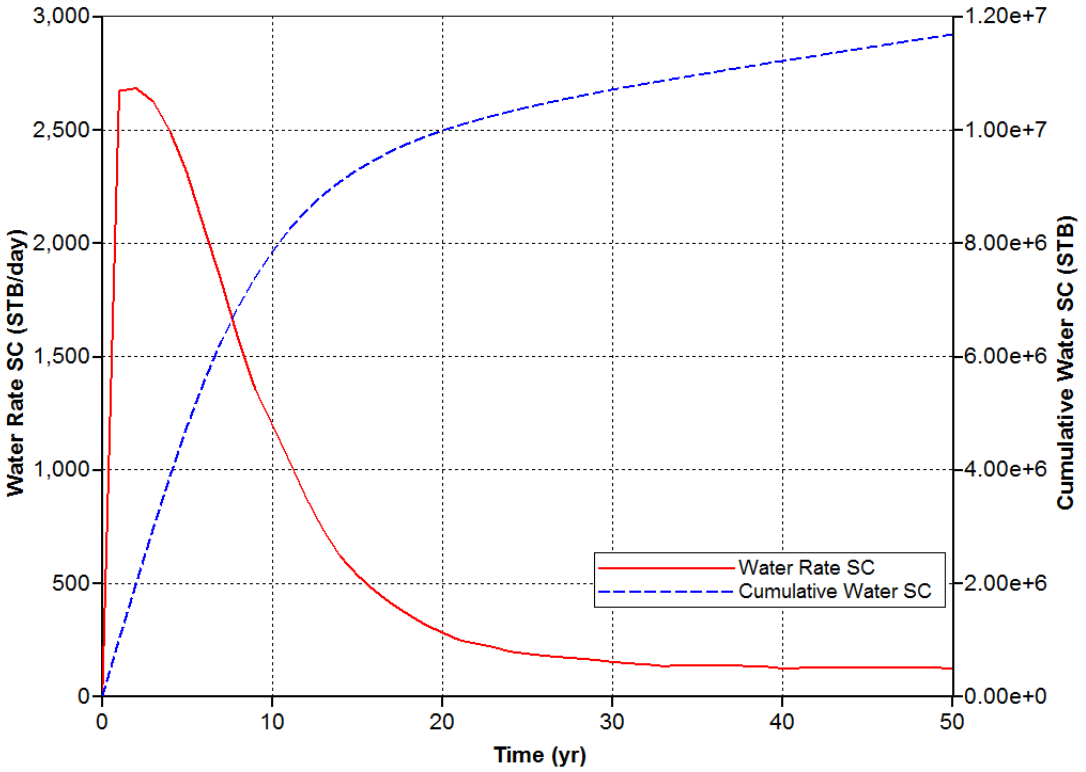

Figure 3.5 Water rates and Cumulative water production of the base model

3.3 Input variables

The reservoir parameters like saturations, porosity of the hydrate bearing sediment (HBS) are calculated from the well log data of PBU L-106 well of upper C and D sands as shown in the base model. The input variables for the Latin hyper cube sampling are reaction kinetics of hydrate formation and dissociation (Activation energy, EACT, refer section 1.8), permeability of hydrate bearing sediment (HBS) and shale layer porosity and permeability. Each reservoir model is simulated using CMG STARS and resulting water production and gas production are recorded from which the discounted cumulative gas production is calculated as the effect of these input variables as shown in Equation (3).

Activation Energy, EACT: Hydrate dissociation can be modeled as an endothermic reaction with an enthalpy of 51 kJ/gmol and activation energy of 81 kJ/gmol (Hong and Pooladi-Darvish,

2005). The activation energy is the minimum energy required to start methane hydrate dissociation. The term EACT used in CMG STARS as referred in Section 1.8 is shown in Equation (28).

$$EACT = E - bR - (28)$$

Where, b is a constant. A truncated normal distribution is used with a mean value of and a standard deviation of 10,000. Figure 3.6 shows the truncated normal distribution of. Table 3.2 gives the details of the distribution used for this study.

Table 3.2 Details of the normal distribution for activation energy (EACT)

Truncated Normal distribution					
Variable	**Mean**	**Std. deviation**	**Min**	**Max**	**N**
EACT	146711	10000	125627	165627	10

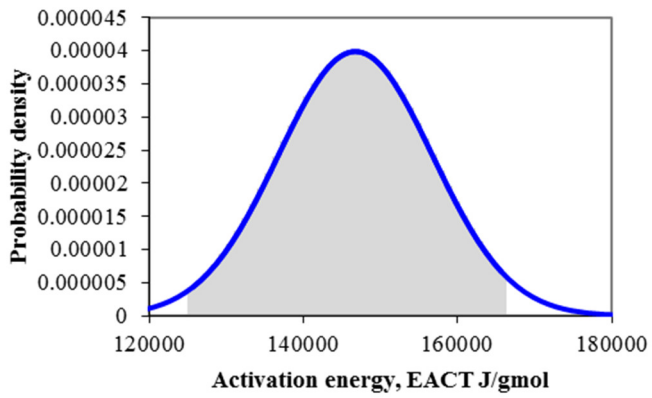

Figure 3.6 Truncated normal distribution of activation energy, EACT

A similar distribution for activation energy for hydrate formation is used. In this study, 10 sample values are randomly picked to cover the entire distribution and details of the values are shown in Table 3.3.

Table 3.3 Sampled values of EACT for hydrate dissociation and formation used in this study

No	E-Hydrate dissociation, J/gmol	EACT Dissociation, J/gmol	E Formation, J/gmol	EACT Formation, J/gmol
1	61202	126830	60003	125630
2	67703	133330	63953	129580
3	73603	139230	71663	137290
4	76253	141880	74403	140030
5	78913	144540	75063	140690
6	83343	148970	81453	147080
7	85843	151470	86813	152440
8	89663	155290	87943	153570
9	91373	157000	92553	158180
10	96573	162200	96363	161990

Shale porosity: Porosity is the void space in a rock or medium. It is the interconnected pores in the medium that allow the medium to have permeability to fluids. It is generally though that higher porosity gives high production rates due to more available pore volume in the reservoir. However it depends on the value of porosity chosen. There is a lot of uncertainty associated with porosity changes. The porosity of hydrate bearing sediment is obtained from the well log data of PBU L106 well. The porosity of the shale layer plays an important in gas production of hydrate reservoirs through depressurization. The permeability of the shale layer is very low and it ranges between 10^{-6}-10^{-9} mD. Figure 3.7 shows the truncated normal distribution used in this study. Table 3.4 and 3.5 shows the details of the distribution and the sample values used in the study.

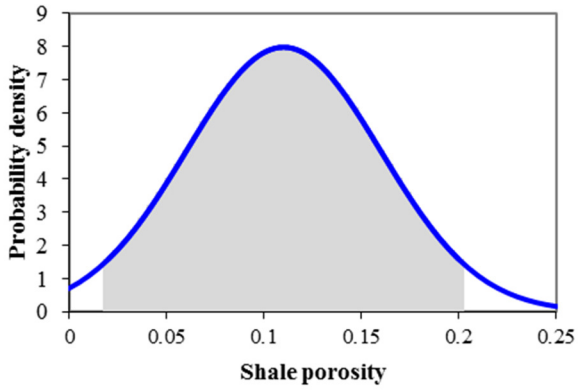

Figure 3.7 Truncated normal distribution of Shale porosity

Table 3.4 Details of normal distribution, Shale porosity

Truncated Normal distribution					
Variable	**Mean**	**Std. deviation**	**Min**	**Max**	**N**
Porosity-Shale	0.11	0.05	0.02	0.2	10

Table 3.5 Sample values of Shale Porosity

No	Porosity-Shale
1	0.034
2	0.037
3	0.069
4	0.072
5	0.088
6	0.099
7	0.117
8	0.144
9	0.172
10	0.197

Absolute Permeability of HBS: Permeability (k) is the ability of a rock or medium to transmit fluids. Effective permeability is the ability to transport a particular fluid in the presence of other immiscible fluids in the reservoir. Relative permeability is the ratio of effective permeability of a particular fluid at a particular saturation to absolute permeability of that fluid at total saturation. Figure 3.8 shows the

distribution of permeability in horizontal direction (*i*-direction). Permeability in *j* and *k* directions are calculated using Equation 29 and 30. Permeability anisotropy for hydrate bearing sediments from core analysis of hydrate bearing sediments of PBU L-106 is ~0.1 and is used for this study. Table 3.6 and 3.7 shows the mean and standard deviation of the truncated normal distribution and sampled data.

$$k_j = k_i \tag{29}$$

$$k_k = 0.1(k_i) \tag{30}$$

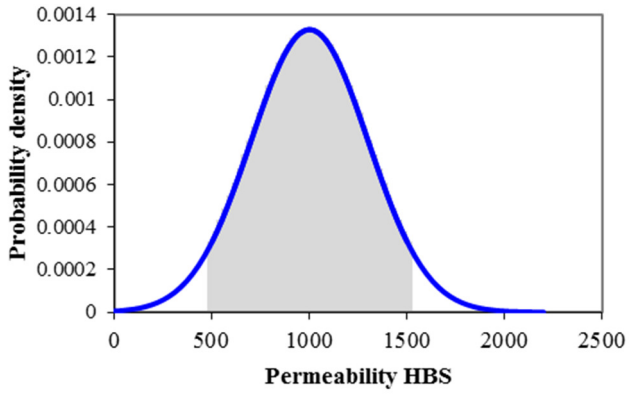

Figure 3.8 Truncated normal distribution of HBS

Table 3. 6 Details of the Normal distribution, Permeability HBS

Truncated Normal distribution					
Variable	**Mean**	**Std. deviation**	**Min**	**Max**	**N**
Permeability-HBS	1000	300	500	1500	10

Table 3.7 Sample values of permeability of HBS

No	k_i, HBS	k_j, HBS
1	532	53
2	545	54
3	648	65
4	768	77
5	899	90
6	1140	114
7	1183	118
8	1194	119
9	1389	139
10	1498	150

Shale Permeability: The accurate measurement of shale permeability is challenging. It is also quite difficult to measure as shale's have very low permeability's ($(10^{-6}$-10^{-9} mD). Pressure transient analysis methods to determine permeability are not applicable for shale's as they produce very little or no fluids. Shale porosity and permeability relationship (Revil and Cathles, 1999) in Equation 31 is used in this study.

$$K_{shi} = K_0 \left({}^{\emptyset_{Sh}}/_{\emptyset_0} \right)^{3m} \tag{31}$$

Where $K_{shi}$the horizontal permeability of shale is, $\emptyset_{Sh}$ is the porosity of shale, K_0 and $\emptyset_0$ are the permeability (Revil and Cathles, 1999) of reference states ($K_0 = 2.75E-06\, mD, \emptyset_{Sh} = 0.5, m = 3$) . Table 3.5 shows sample values for shale porosity. Table 3.8 shows the sample values for shale horizontal ($\boldsymbol{k_{shi}}$) and vertical permeability ($\boldsymbol{k_{shk}}$).

Table 3.8 Sample values of Shale Permeability

No	$\boldsymbol{k_{shi}, Shale}$	$\boldsymbol{k_{shk}, Shale}$
1	1.69E-06	1.69E-07
2	1.84E-06	1.84E-07
3	3.47E-06	3.47E-07
4	3.62E-06	3.62E-07
5	4.38E-06	4.38E-07
6	4.93E-06	4.93E-07
7	5.86E-06	5.86E-07
8	7.18E-06	7.18E-07
9	8.60E-06	8.60E-07
10	9.85E-06	9.85E-07

Job pattern for Latin hyper cube sampling: The sample values for each parameter are randomly picked to create a job pattern. A total of 50 simulations are conducted to create a response surface of discounted cumulative gas production. The effect of each parameter on gas production is evaluated and ranked. Table 3.9 shows the job pattern and values of input variables used in each simulation. The pattern in Table 3.9 shows the number of sample value (out of 10) and 'G' represents calculated values, For example in "02040809GGGGGG" ,"02" represents 3rd value of

shale porosity in Table 3.5, "04" represents 5th value of horizontal permeability (k_i, HBS) in Table 3.7, "08" represents 9th value of activation energy (*EACT*) in Table 3.3, "09" represents 10th value of activation energy (*EACTB*) in Table 3.3 and 'G' represents dependent variables such as permeability (k_j, HBS), $k_k, (HBS)$, ($k_{shi}, shale$), $k_{shj}, (shale)$ and $k_{shk}, (shale)$. The dependent variables were calculated and the sampling simulation runs were performed.

Table 3.9 Job pattern of Latin hypercube sampling

No	Pattern	POR	PERM	EACT	EACTB
1	02040809GGGGGG	0.069	899	157000	162000
2	03070101GGGGGG	0.072	1194	133000	130000
3	01070303GGGGGG	0.037	1194	142000	140000
4	01020706GGGGGG	0.037	648	155000	152000
5	02040206GGGGGG	0.069	899	139000	152000
6	08080603GGGGGG	0.172	1389	151000	140000
7	07010501GGGGGG	0.144	545	149000	130000
8	03050104GGGGGG	0.072	1135	133000	141000
9	05040508GGGGGG	0.099	899	149000	158000
10	06030700GGGGGG	0.117	768	155000	126000
11	05050301GGGGGG	0.099	1135	142000	130000
12	07090007GGGGGG	0.144	1498	127000	154000
13	00040009GGGGGG	0.034	899	127000	162000
14	07030608GGGGGG	0.144	768	151000	158000
15	08000203GGGGGG	0.172	532	139000	140000
16	02010108GGGGGG	0.069	545	133000	158000
17	05080304GGGGGG	0.099	1389	142000	141000
18	04000304GGGGGG	0.088	532	142000	141000
19	07000705GGGGGG	0.144	532	155000	147000
20	06000907GGGGGG	0.117	532	162000	154000
21	04030603GGGGGG	0.088	768	151000	140000
22	01010002GGGGGG	0.037	545	127000	137000
23	00060201GGGGGG	0.034	1183	139000	130000
24	09030005GGGGGG	0.197	768	127000	147000
25	02060200GGGGGG	0.069	1183	139000	126000
26	08080405GGGGGG	0.172	1389	145000	147000
27	01010508GGGGGG	0.037	545	149000	158000
28	02080902GGGGGG	0.069	1389	162000	137000
29	09080009GGGGGG	0.197	1389	127000	162000
30	08020702GGGGGG	0.172	648	155000	137000

No	Pattern	POR	PERM	EACT	EACTB
31	05020902GGGGGG	0.099	648	162000	137000
32	06050406GGGGGG	0.117	1135	145000	152000
33	08050407GGGGGG	0.172	1135	145000	154000
34	03050307GGGGGG	0.072	1135	142000	154000
35	03090804GGGGGG	0.072	1498	157000	141000
36	03060800GGGGGG	0.072	1183	157000	126000
37	04060103GGGGGG	0.088	1183	133000	140000
38	01030805GGGGGG	0.037	768	157000	147000
39	00020106GGGGGG	0.034	648	133000	152000
40	07000200GGGGGG	0.144	532	139000	126000
41	09090608GGGGGG	0.197	1498	151000	158000
42	00070401GGGGGG	0.034	1194	145000	130000
43	09060500GGGGGG	0.197	1183	149000	126000
44	06020509GGGGGG	0.117	648	149000	162000
45	09070404GGGGGG	0.197	1194	145000	141000
46	00090807GGGGGG	0.034	1498	157000	154000
47	04010606GGGGGG	0.088	545	151000	152000
48	06070909GGGGGG	0.117	1194	162000	162000
49	05090902GGGGGG	0.099	1498	162000	137000
50	04040705GGGGGG	0.088	899	155000	147000

3.4 Results of Latin Hyper cube sampling

Figure 3.9 shows the representative gas rates of the simulations and shows a distribution of all runs. The base run has impermeable shale surrounding the hydrate bearing sediment and is shown in black. All other runs shown in Figure 3.9 have permeable shale. As shown in Figure 3.9 depressurization is more effective when the hydrate bearing sediment is surrounded by impermeable shale and is less effective with increase in the shale permeability. The decreases in the gas rate of all the simulation runs are attributed to permeable shale.

The maximum gas rate for all simulation runs are in the order of 180-380 MSCF/day as shown in Figure 3.9. Figure 3.10 shows cumulative gas for all the simulation runs. The water rates and cumulative water production are shown in Figure 3.11 and Figure 3.12. A decrease in Gas-water ratios is observed in all the simulation runs due to decrease in gas and water production which are influenced by hydrate reaction kinetics as shown in Figure 3.13. A discounted cumulative gas production with a discount rate of 15% is calculated for each simulation run. Effects of each parameter on the discounted cumulative gas production are calculated and are listed in a Tornado plot as shown in Figure 3.14.

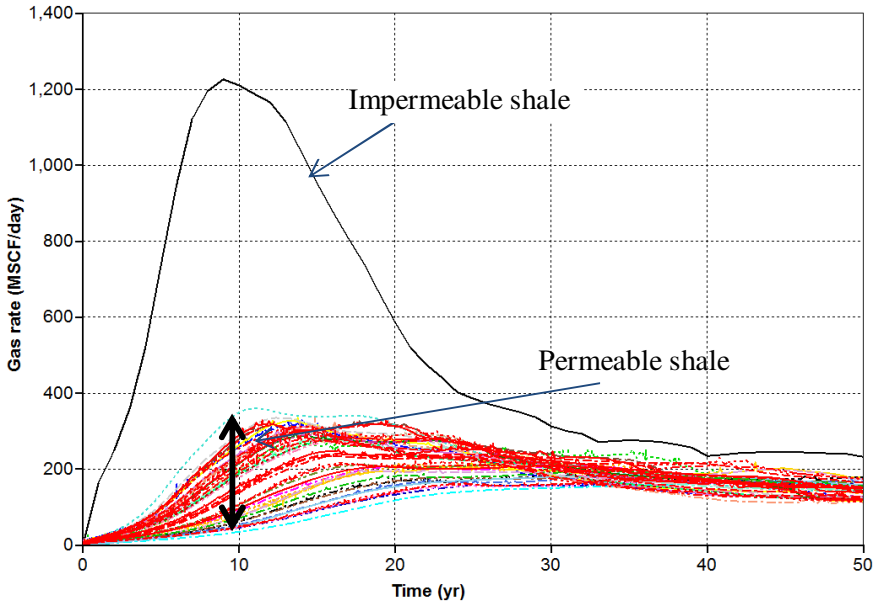

Figure 3.9 Gas rates of all the simulations in the Latin hypercube sampling, Black line represents base model

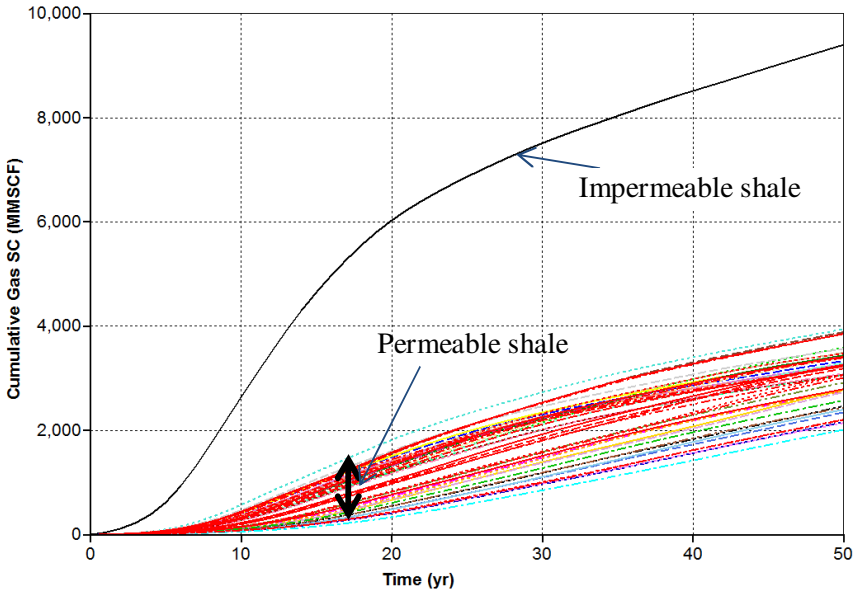

Figure 3.10 Cumulative gas production of all the simulations in the Latin hypercube sampling, Black line represents base model

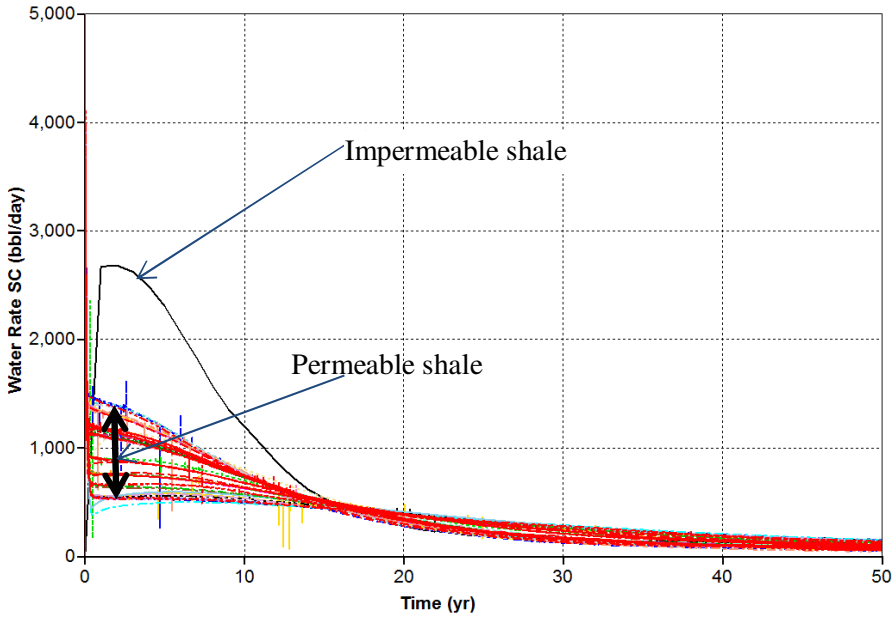

Figure 3.11 Water rates of all the simulations in the Latin hypercube sampling, Black line represents base model

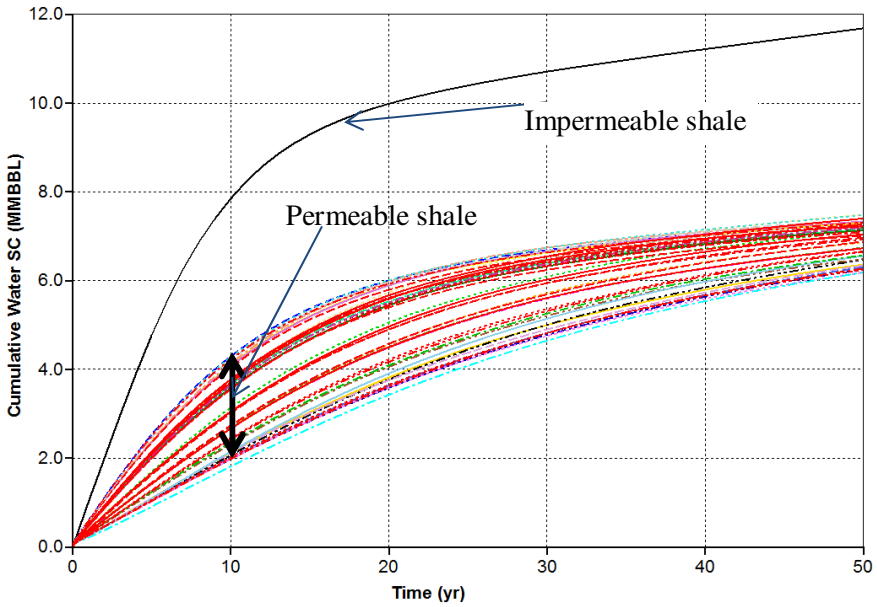

Figure 3.12 Gas rates of all the simulations in the Latin hypercube sampling, Black line represents base model

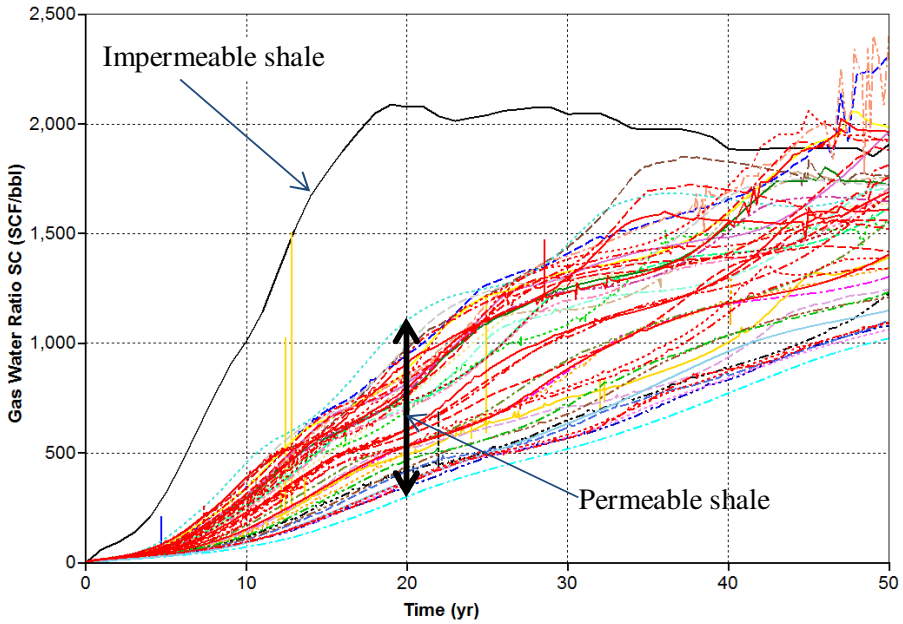

Figure 3.13 Gas water ration of all the simulations in the Latin hypercube sampling, Black line represents base model

The tornado plot shows the actual predicted response change in discounted gas rate as the parameter travels from a smallest sample value to the largest sample value. Permeability of hydrate bearing sediment (PERM) has the highest positive effect. Shale porosity (POR-Shale) and permeability has a negative effect on gas production. Hydrate dissociation activation energy (EACT) has a higher negative effect than activation energy (EACTB) of hydrate formation as shown in Figure 3.14.

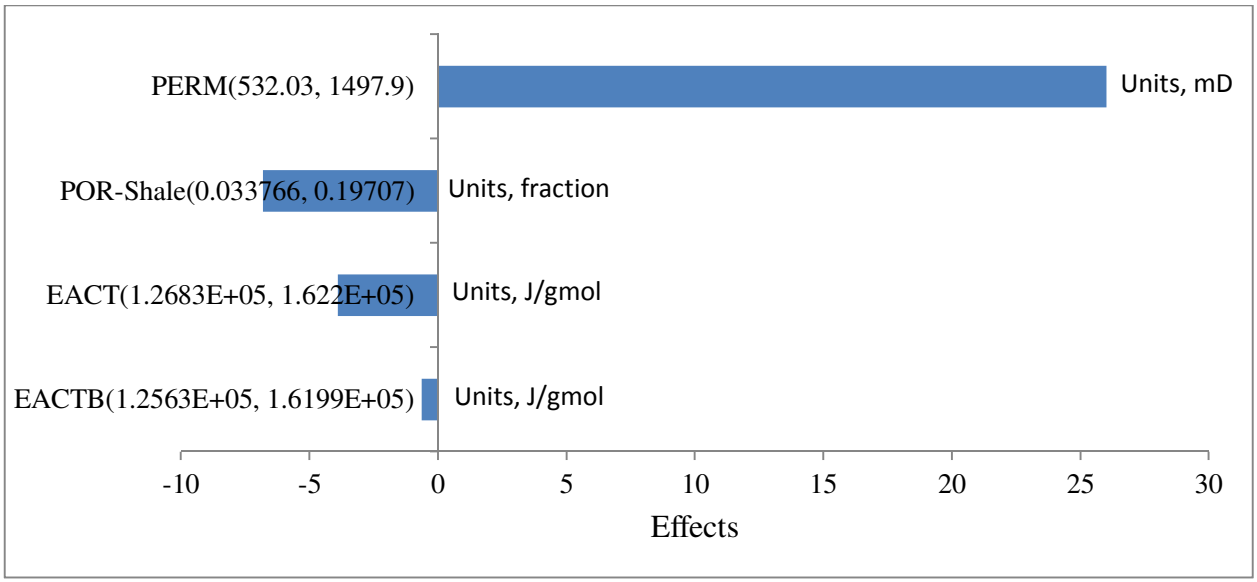

Figure 3.14 Tornado plot showing effects of each parameter when varied from a low value to a high value

Statistics of Discounted Cumulative gas production

```
Objective Function Name: Discounted Cumulative gas production
Model Classification: Linear Model
Summary of Fit
R-Square   0.940974
R-Square Adjusted 0.935727
R-Square Prediction     0.924
Mean of Response  6.17E+06
Standard Error    619099

Analysis of Variance
Source     Degrees of Freedom  Sum of SquaresMean Square  F Ratio      Prob > F
Model      4      2.75E+14     6.87E+13     179.343      <0.00001
Error      45     1.72E+13     3.83E+11
Total      49     2.92E+14

Effect Screening Using Normalized Parameters (-1, +1)
Term       Coefficient   Standard Error      t Ratio      Prob > |t|    VIF
Intercept  6.32E+06      91521.6       69.0987      <0.00001     0
POR(0.033766, 0.19707)  -943073       138446 -6.81183      <0.00001     1.01
PERM(532.03, 1497.9)    3.35E+06      128658 26.0064       <0.00001     1.02
EACT(1.2683E+05, 1.622E+05)    -575467       147581 -3.89934      0.00032      1
EACTB(1.2563E+05, 1.6199E+05)  -91024.4      139569 -0.65218      0.5176 1.01

Coefficients in Terms of Actual Parameters
Term       Coefficient
Intercept  6.05E+06
POR -1.15E+07
PERM       6928.31
EACT       -32.5399
EACTB      -5.00684

Equation in Terms of Actual Parameters
Dicounted      Cumulative      gas      production      (Std.      m3)=6.04763E+06-
1.15499E+07*POR+6928.31*PERM-32.5399*EACT-5.00684*EACTB
```

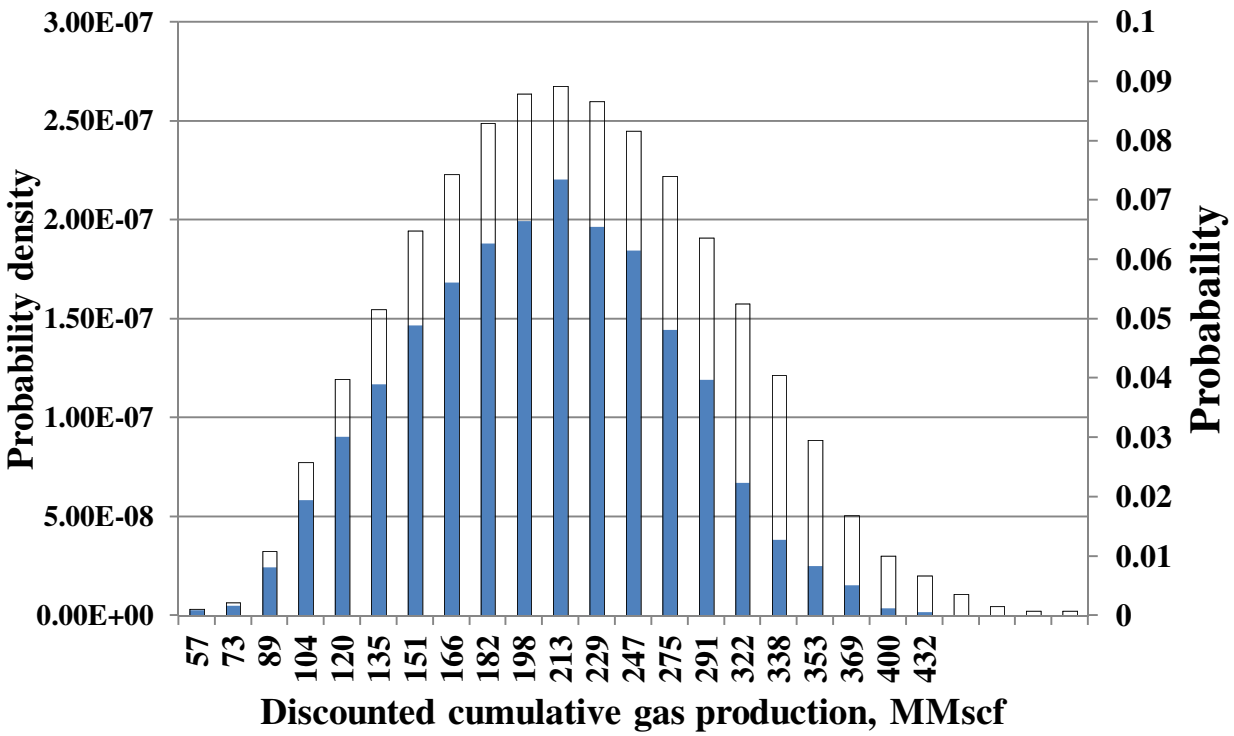

Figure 3.15 Probability distribution of discounted cumulative gas production

Figure 3.15 shows the probability distribution of discounted cumulative gas production with P50 of 213 MMScf, P10 of 135 MMScf and P90 of 306 MMScf. The blue columns in Figure 3.15 represent probability density and the white color columns represent probability.

4. Gas Production from Prudhoe Bay L-Pad deposit

The objective of this chapter is to compare the performance and economics of vertical and horizontal wells in hydrate bearing reservoirs. It has been suggested by Moridis (Moridis, 2008b) that conventional type of wells using horizontal well technology and following the depressurization method for hydrate dissociation yield high amounts of gas from the hydrate reservoirs. A horizontal well creates high contact in hydrate bearing formation resulting in high gas production. Moridis et al (Moridis, 2008b) used horizontal well symmetry thereby simulating one slice in the horizontal direction for comparing gas production from horizontal and vertical wells. By simulating one slice, the pressure drop in the horizontal well was neglected by Moridis et al (Moridis, 2008b). Zhang et al. (Zhang et al., 2010) studied alternative horizontal well designs for gas production in Shenhu hydrate deposit, North Slope of China Sea and concluded that Shenhu hydrate deposits are not economically efficient. The effect of deviated well on gas production has not been studied. It has been observed from our previous studies that bottom hole pressure is the most important parameter affecting gas production (Gaddipati, 2008). Neglecting pressure drop of horizontal wellbore will over predict gas production. This is an attempt to compare gas production from a horizontal well and a deviated well to a vertical well of similar size. A mechanistic well bore model developed by Petalas and Aziz (Petalas and Aziz, 2000) is used to incorporate pressure drop in this study. The method of production is depressurization for all simulations. The reservoirs are adapted from Problem 7b of the DOE Code Comparison Study (Gaddipati, 2008).

4.1 Gas production using vertical well

In this section of the study, a conventional vertical well is simulated for gas production. The structure of the simulated grid is a cylinder with a vertical production well at the axis of the cylinder. Figure 4-1 shows a schematic of the reservoir used to calculate production rates using a vertical well at the bottom of the hydrate bearing layer. It is a 450 m × 178 m reservoir in *r*-*z* directions. There are 80 cells distributed logarithmically from $r = r_w = 0.111$ m. (r_w = well bore radius) to r = 450m. In the z direction, the hydrate bearing zone is uniformly discretized into 20 cells each of 0.9 m. The upper and lower shale zones are logarithmically discretized in the z direction. For each subsequent cell, the dz obeys $dz_i = dz_{i-1} * 1.49587$ (as one moves away from the hydrate zone). There is no net mass transport between the reservoir and the surroundings. The upper boundary temperature is held constant at 274.715 K and the lower boundary temperature is held at constant at 277.271 K. The simulations are carried over a time period of 50 years. Data for gas production rate, water production rate, cumulative gas production and cumulative water production is recorded with a time step of 0.001 days for 50 years.

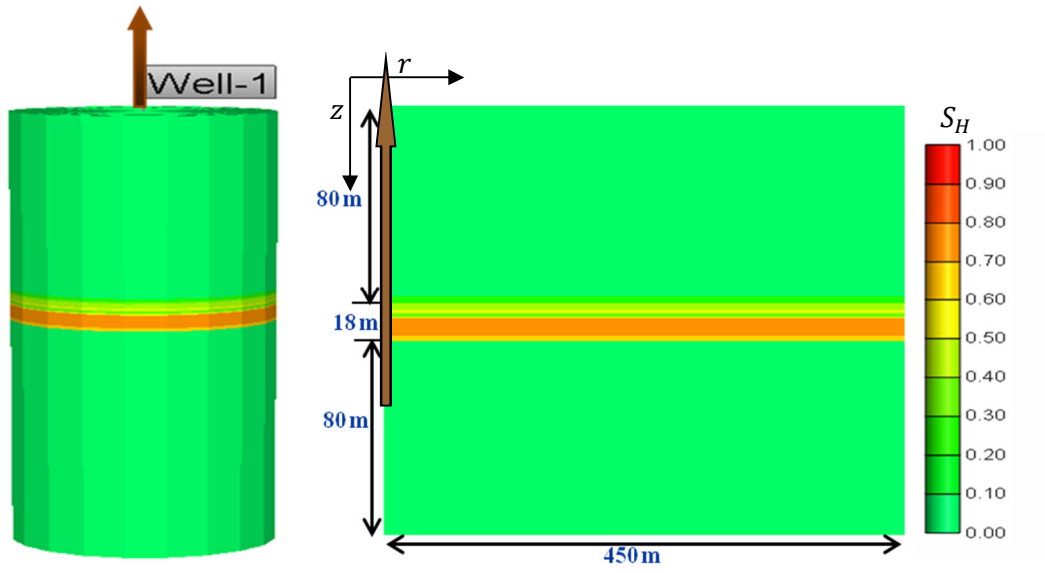

Figure 4.1 Radial reservoir grid used for the simulation of gas production from a vertical well

4.2 Gas production from a horizontal well

A similar reservoir model used in Section 4.1 is used to simulate gas production from a horizontal well. Figure 4.2 shows a schematic of the reservoir used to calculate production rates using a horizontal well at the bottom of the hydrate bearing layer. It is a 450 m × 1 m × 245 m reservoir in *i-j-k* directions. For the actual simulation using CMG STARS, because of symmetry, slices in the *j*-direction of the reservoir are simulated to incorporate well bore pressure drop which is then later integrated for the entire reservoir using a numerical code (Polynomial Interpolation). The slice simulated is shown in Figure 4.3. It is 1 m thick in the *j-direction*. The hydrate layer is discretized into 1 m blocks in the *k-direction*; the upper shale layer is discretized into 3 m blocks in the *k-direction* and the lower shale layer is discretized into 2.5 m blocks in the *k-direction*. The entire reservoir is divided into 1 m blocks in *i-direction*. Well log data of PBU L106 well is used for porosity and saturations of hydrate bearing sediment. An Impermeable shale with water saturation assumed to be 100% is used similar to the model simulated using vertical well.

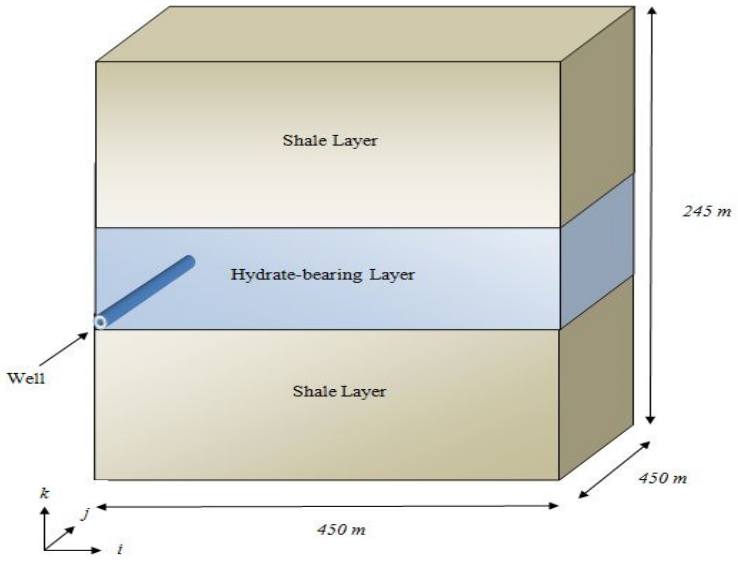

Figure 4.2 Schematic representation of the reservoir model for a horizontal well

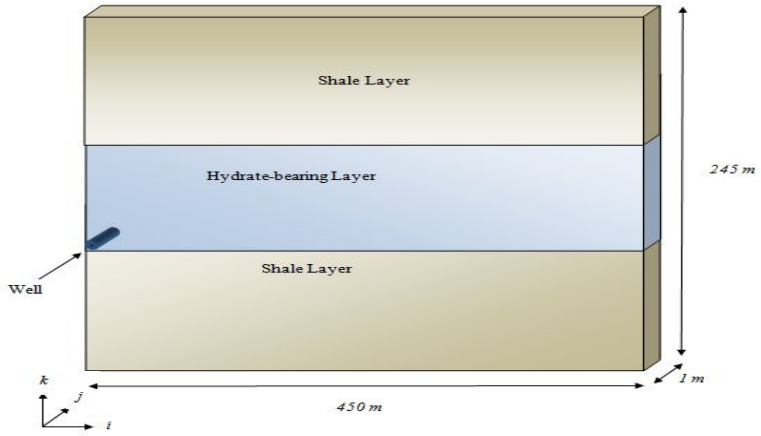

Figure 4.3 Slice of the reservoir model simulated with j = 1 m

Figure 4.4 shows the wellbore pressure drop of a horizontal and deviated well from a mechanistic wellbore model developed by Petalas et. al. (Petalas and Aziz, 2000) A constant gas flow rate of 20,000 m^3/day and water flow rate of 400 m^3/day is used to calculate pressure drop in the well bore.

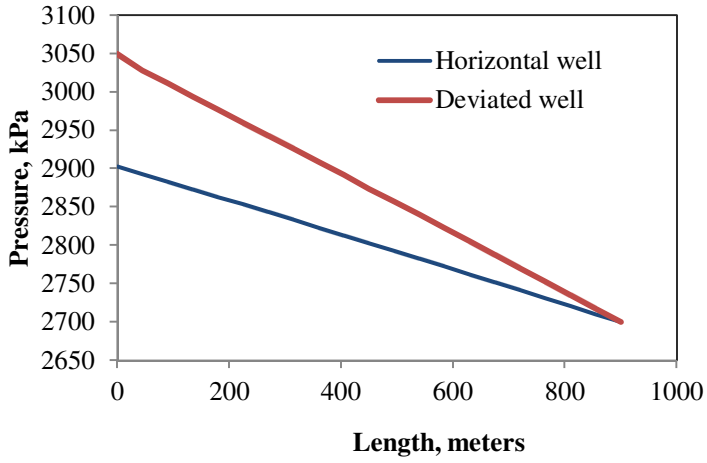

Figure 4.4 Well bore pressure drop of horizontal and deviated well

Figure 4.5 shows schematic representation of slices in the *j*-direction for horizontal and deviated well. The horizontal well intersects the hydrate bearing sediment without any deviation at the bottom of the Upper C sand. Different cases studied in this work are (i) Horizontal well without wellbore pressure drop, (ii) Horizontal well with pressure drop, and (iii) Deviated well.

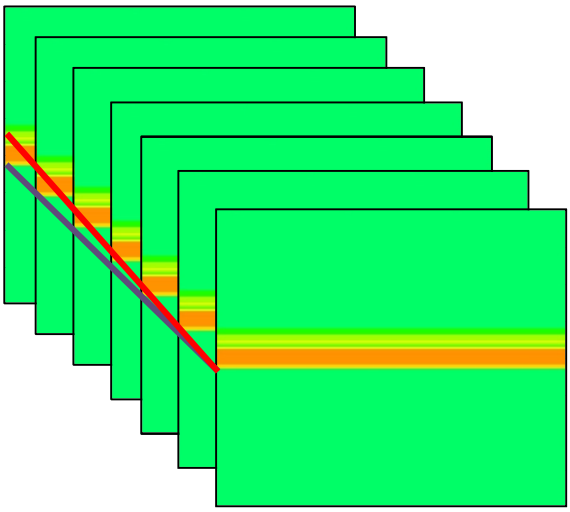

Figure 4.5 Slices simulated for horizontal and deviated well

Horizontal well without pressure drop: For the horizontal slice (450 m × 1 m × 245 m, in *i-j-k* directions). In order to integrate the results obtained for the entire reservoir, the rates are multiplied by a factor of 450π. This factor is worked out from the fact that the reservoir is 450 m thick in the *j-direction* and that it is being compared to a cylindrical system (450 m × 450 m, *r-z* direction). The ratio of their volumes is π. For this scaling up, the pressure drop across the horizontal well is neglected in this case.

Horizontal well with pressure drop: Six slices in the *j*-direction are simulated at bottom hole pressures of 2700 k Pa, 2750 kPa, 2800 kPa, 2900 kPa. Each slice is simulated with well perforation at the bottom of hydrate bearing sediment as shown in Figure 4.5.

Deviated well with pressure drop: Seven slices in the *j*-direction are simulated at bottom hole pressures of 2700 k Pa, 2750 kPa, 2800 kPa, 2900 kPa, 2950 kPa, 3000 kPa and 3050 kPa. The

well perforation for each slice is shifted from bottom to top of the hydrate bearing sediment as shown in Figure 4.5.

4.3 Comparison of gas production from vertical and horizontal well

The simulations are carried over a time period of 50 years. Data for gas production rate, water production rate, cumulative gas production and cumulative water production is recorded with a time step of 0.001 days for period of 50 years. The numerical interpolation code used for calculating gas production from a horizontal well is shown below

```
Program Main
       CHARACTER*40 OUTFILE,INFILE
      INTEGER M,N
      parameter (M=450)
      REAL DY,X(1000),Y(1000),XA(1500),YA(1500),sum

      WRITE (*,*) 'Enter data input file name '
c      READ(*,*) INFILE
      INFILE= 'trial.dat'

      OPEN(UNIT=11,FILE=INFILE,STATUS='OLD',IOSTAT=ISTAT)

      IF ( ISTAT .GT. 0 ) THEN
        WRITE (*,*) ' **** UNABLE TO OPEN INPUT FILE **** '
        STOP
      ENDIF


      open(unit=22,file='out.dat',status='unknown',iostat=istat)
       open(unit=23,file='sum.dat',status='unknown',iostat=istat)
       IF ( ISTAT .GT. 0 ) THEN
        WRITE (*,*) ' **** UNABLE TO OPEN INPUT FILE **** '
        STOP
      ENDIF
      X(1)=0
      X(2)=450
      X(3)=900
      J=0
       DO WHILE (.NOT. EOF(11))
         J = J + 1
c         READ(11,*) text, text,text
         READ(11,*) Y(1), Y(2), Y(3)
             sum= Y(1)

                   do 10 i=1,900
                       xa(i)=1*i
                       call POLINT(x,y,3,xa(i),ya(i),dy)
                        write (22,*) i,xa(i), ya(i)
                        sum=sum+ya(i)
```

```
   10              continue

                  write (23,*) sum


       END DO
       n=j
      write (*,*) n
      end

POLINT

SUBROUTINE polint(xb,yb,n,x,y,dy)
      INTEGER n,NMAX
      REAL dy,x,y,xb(n),yb(n)
      PARAMETER (NMAX=2000)
      INTEGER i,m,ns
      REAL*16 den,dif,dift,ho,hp,w,c(NMAX),d(NMAX)
      ns=1
      dif=abs(x-xb(1))
      do 11 i=1,n
        dift=abs(x-xb(i))
        if (dift.lt.dif) then
          ns=i
          dif=dift
        endif
        c(i)=yb(i)
        d(i)=yb(i)
11    continue
      y=yb(ns)
      ns=ns-1
      do 13 m=1,n-1
        do 12 i=1,n-m
          ho=xb(i)-x
          hp=xb(i+m)-x
          w=c(i+1)-d(i)
          den=ho-hp
          if(den.eq.0.)stop 'failure in polint'
          den=w/den
          d(i)=hp*den
          c(i)=ho*den
12      continue
        if (2*ns.lt.n-m)then
          dy=c(ns+1)
        else
          dy=d(ns)
          ns=ns-1
        endif
        y=y+dy
13    continue
      return
      END
```

The reservoir with horizontal well yielded quicker and higher gas rates at earlier times. This can be attributed to the quicker depressurization in the horizontal well. Gas production rates from horizontal wells are highest during initial days of operation as shown in Figure 4.6. Gas rates for horizontal well without pressure drop reached a maximum rate of 1059 Mscf/day (30,000 m^3/day) in 5 years. Gas rates for horizontal well with pressure drop reached a maximum gas rate of 600 Mscf/day (17,000 m^3/day) in 5 years. Higher water rates are obtained in the horizontal well case than that in the vertical well case. The higher water removal causes higher depressurization of the reservoir and enhances gas production due to the pressure gradient in the reservoir as shown in Figure 4.7. Pressure drop have a huge negative impact on gas production from horizontal wells. Symmetry cannot be assumed in horizontal wells. Production of water is approximately 3 times more for horizontal wells as shown in Figure 4.7. Calculation of pressure drop plays a crucial role in gas production from horizontal wells. Integrated system of a well bore model with reservoir simulations is needed to accurately predict gas production from horizontal wells.

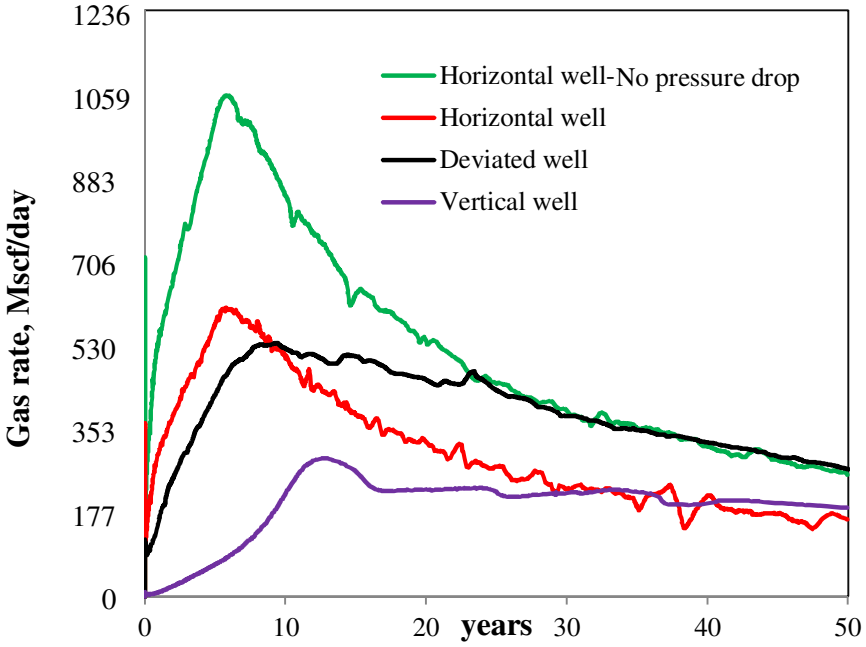

Figure 4.6 Gas rates for horizontal well without pressure drop, horizontal well, deviated well and vertical well

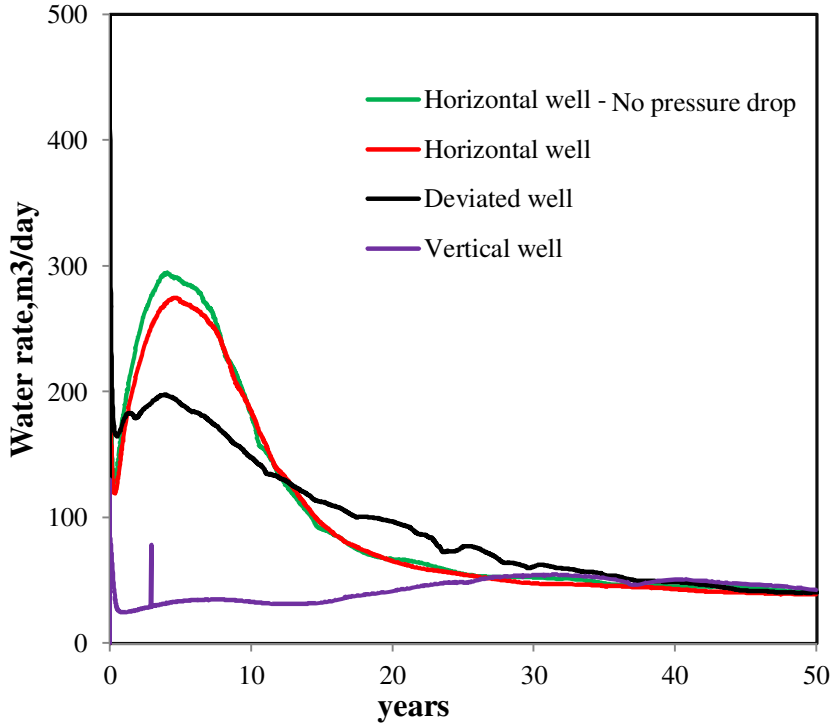

Figure 4.7 Water rates for horizontal well without pressure drop, horizontal well, deviated well and vertical well

5. 3-D reservoir modeling of Walker Ridge 313 site, Gulf of Mexico

5.1 Introduction

In April and May of 2009, the U.S. Department of Energy (DOE) National Energy Technology Laboratory (NETL) in collaboration with the U.S. Geological Survey (USGS), the U.S. Minerals Management Service, an industry research consortium led by Chevron, and others completed a marine hydrate drilling expedition in the Gulf of Mexico. The 21-day logging-while-drilling (LWD) expedition targeted three drilling sites: Walker Ridge 313 (WR 313), Green Canyon 955 (GC 955), and Alaminos Canyon 21 (AC 21). A suite of density, gamma ray, and resistivity logs was collected from the Joint Industry Project (JIP) Leg II LWD expedition for two wells (WR313-G and WR313-H) drilled in the WR 313. Figure 5.1 shows different sites evaluated by Joint Industry Project (JIP).

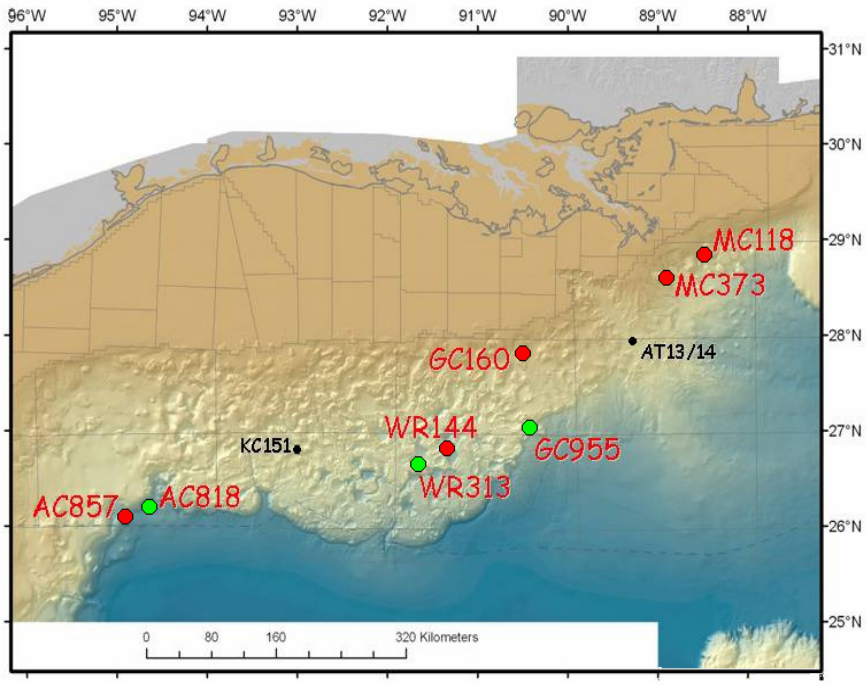

Figure 5.1 Location of all sites evaluated (red) and those ultimately selected (green) for JIP leg II gas hydrate project. Sites drilled in the first phase of JIP, which focused on geo-hazard issues and occurrences of gas hydrate in fine grained sediments are shown in black(Jones et al., 2008).

A suite of density, gamma ray, and resistivity logs was collected from the LWD expedition of JIP Leg II for wells drilled in the Gulf of Mexico (Collett et al., 2010; Mrozewski et al., 2010; Shelander et al., 2010). The JIP wells tested three horizons: Blue, Orange and Green (Nomenclature) in WR313. The structure of the WR 313 is dipping from NW to SE. The WR Blue sand has numerous minor channels grading into a broad thin sheet, whereas the WR Orange has clay-filled channels with sand rich axial lags and marginal levees. Figure 5.2 shows a cross line of seismic in WR 313 showing WR 313 G well and WR 313 H well. The occurrence of gas hydrate- bearing sand was confirmed by LWD data at each target above the base of gas hydrate stability zone (BGHS).

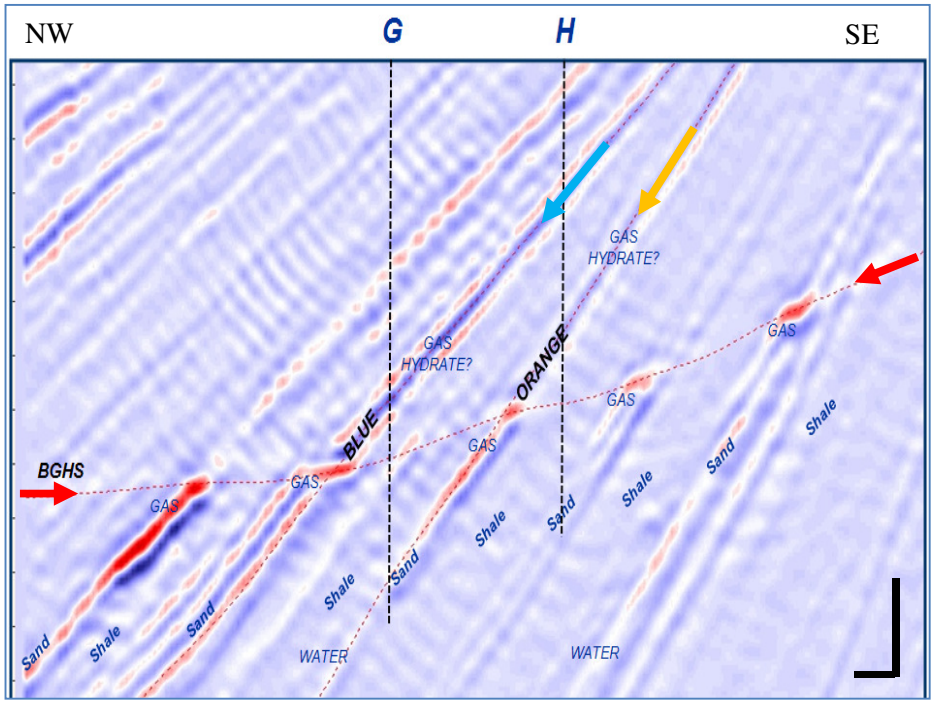

Figure 5.2 cross line example of seismic in WR 313 showing G and H wells. The red arrows indicate BSR which delineates the base of gas hydrate stability zone (BGHS). The blue and orange arrows indicate blue and orange horizons. The scale bars (bottom, right) represent 200 m horizontal and 100 ms vertical (Shelander et al., 2010).

Concentrations of gas hydrates at the WR 313 site were estimated through integration of pre-stack seismic inversion and rock property modeling by Shelander et.al. (Shelander et al., 2010).

The distribution of hydrate saturation of Blue and Orange sands is shown in Figure 5.3. The yellow color areas in Figure 5.3 represents hydrate saturation of 70% and the light blue color area represents hydrate saturation of ~ 10%. The WR313#1 well shown in Figure 5.3 is a pre-existing industry well used for conventional resources. Up to 46 ft. of cumulative hydrate bearing sand was discovered for G well within a 230 ft. gross interval.

A total of 25 different sand bodies are identified internally with thickness ranging from 1-6 ft. Gamma-ray (GR) log and schematic representation of different sand bodies for WR 313 G in Blue sand is shown in Figure 5.4. Different environments are interpreted in the region ranging from proximal to distal levees of relatively small-scale turbiditic channels to more distal-thin and widespread unconfined sheet sands (Shelander et al., 2010). The Orange and Blue sands are separated vertically by several hundred feet of finer-grained lithofacies, including silts and clays. The thickness of Orange sand is high in WR 313H well as per the LWD data. Two sand bodies are detected with thickness varying from 14-20 ft. and a cumulative thickness of 32 ft. Figure 5.5 shows gamma ray log for the H well with a schematic representation of different sand bodies for the Orange deposit.

From the set of seismic data from the pre-drill analysis and the LWD data, schematic representations of Walker Ridge 313 Blue and Orange were made by Boswell et al. (Boswell et al., 2011). Figure 5.6 shows the schematic representations which are used for building 3-D models. The dotted line represents the base of the gas hydrate stability zone. Area inside heavy line in Figure 5.6(a) represents area of greatest reservoir quality. In Figure 5.6(a) for Blue sand, dark green represents sand thickness greater than 20ft; green indicates sand thickness between 10-20 ft and light green denotes sand thickness less than 10 ft. Initial estimations of porosity in the blue sands are approximately 33% at the H well and 39% at the G well.

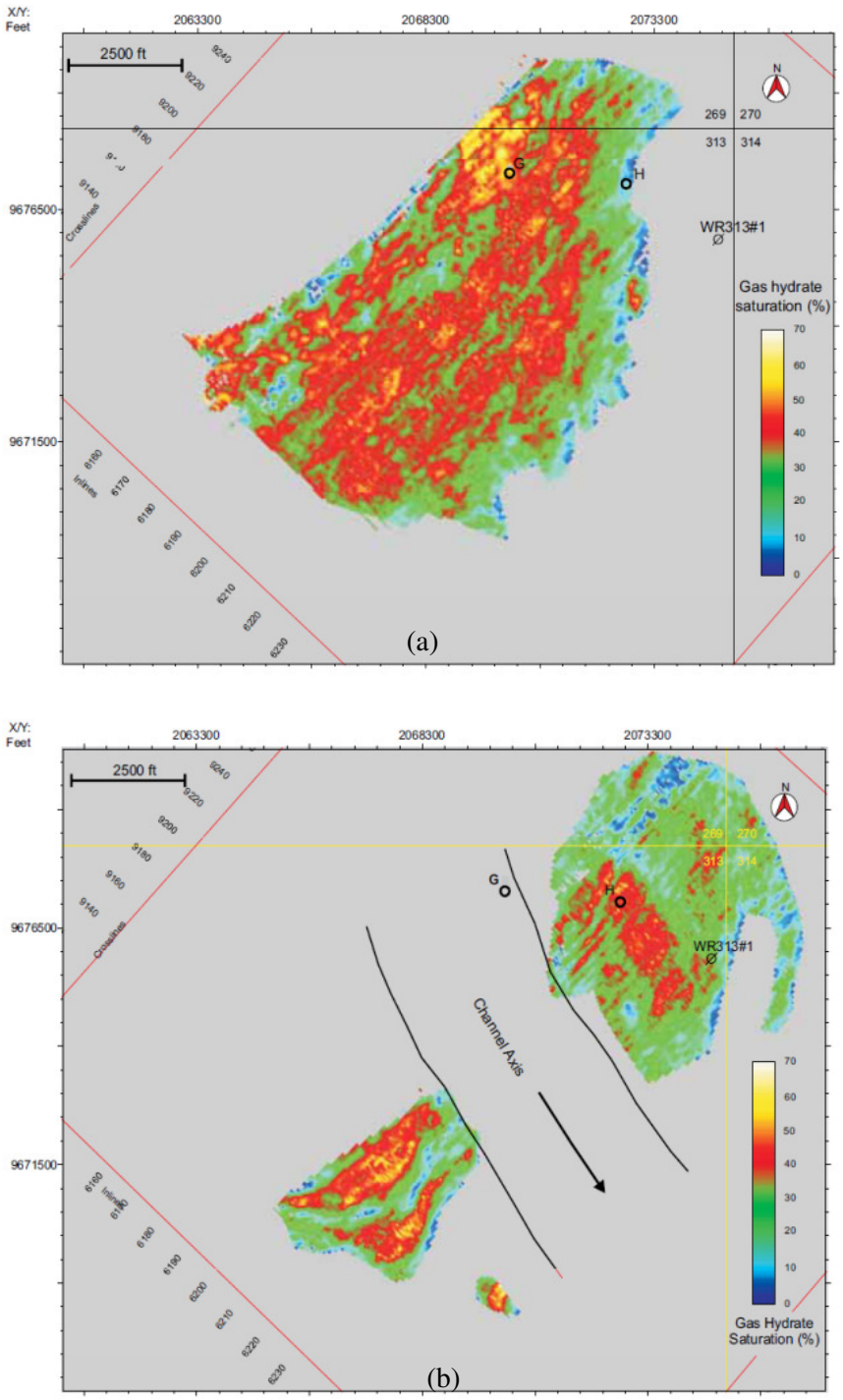

Figure 5.3 (a) shows the predicted hydrate saturations for the WR 313 Blue hydrate-bearing sand and Figure 5.3(b) shows the hydrate saturations for the WR 313 Orange hydrate bearing sand(Shelander et al., 2010).

Initial saturations at the G and H well are determined using Archie's equation(Archie, 1942) and resistivity data. The gas hydrate saturation at the G well is around 80% and 45% at the H

well. The gas hydrate bearing sands are surrounded by clay rich sediments. The gas hydrate bearing sediments near the BGHS to the north are likely in direct contact with free gas bodies. The gas saturations for the gas rich sand bodies as shown in pink color in Figure 5.6(a) are difficult to determine based on the available information. In the simulation efforts it is assumed that there is no gas rich sediment surrounding the base of the gas hydrate stability zone. In Figure 5.6(b) for Orange sand, Brown represents sand thickness greater than 20 ft; yellow indicates sand thickness between 10-20ft and tan color denotes sand thickness less than 10ft. The porosity of the upper orange sand unit at the H well is ~37% and hydrate saturation is 60-90%. In the lower sand unit of the Orange deposit the porosity is high exceeding 40% but the hydrate saturation is lower (40-60%). More geologic details about the WR313 can found in Boswell et al. (Boswell et al., 2011).

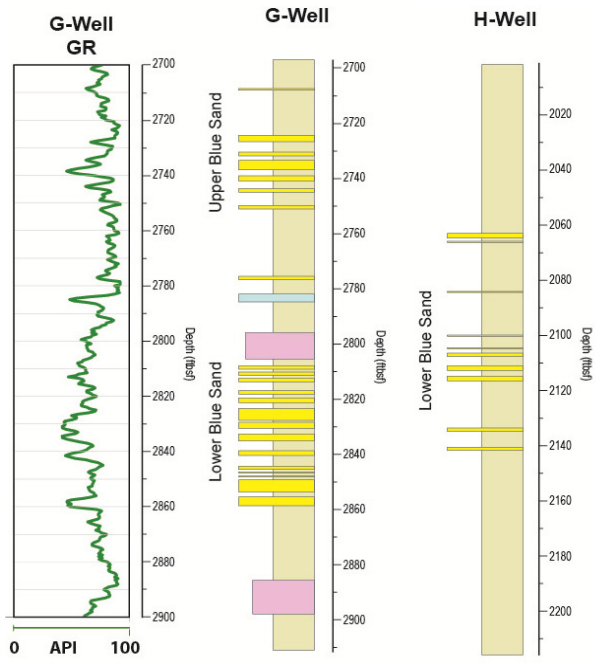

Figure 5.4 Gamma-ray (GR) log through the Blue sands WR313-G and schematic depiction of changes in lithofacies and relative pore fluid saturations for wells G and H. The yellow color indicates moderate to high saturation for hydrate-bearing sands, blue color is waterbearing sand, tan color is dominantly water-bearing fine-grained lithofacies, and the pink color indicates low-porosity, lowhydrate saturation lithofacies.

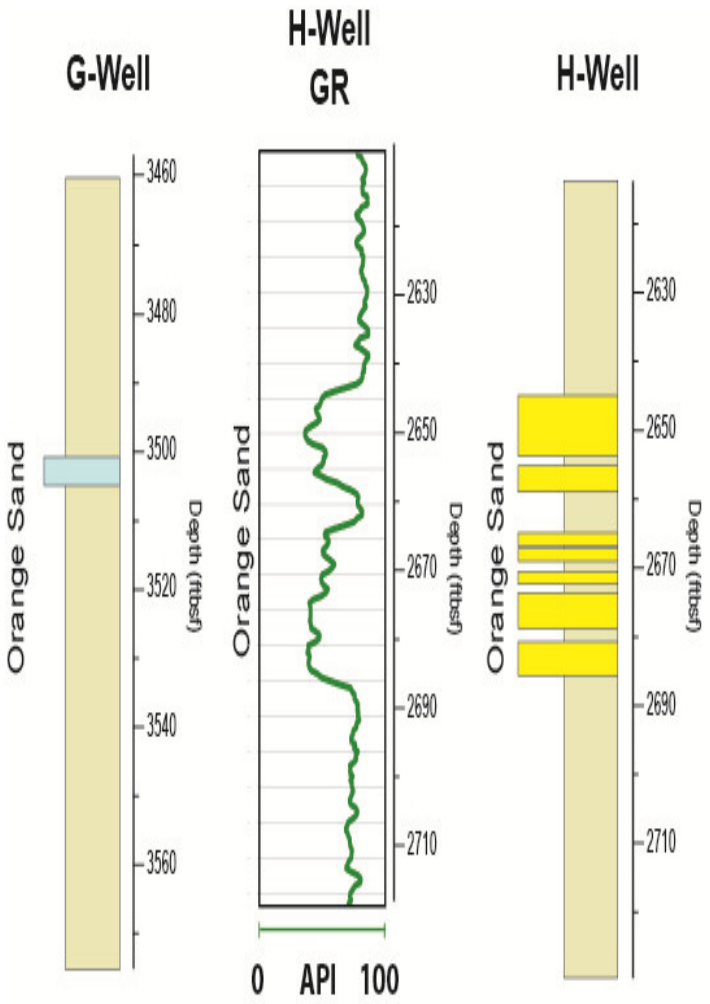

Figure 5.5 Gamma ray (GR) log of the H well for Orange sands and schematic representation of orange sands in both G and H wells. The yellow color indicates moderate to high hydrate saturation and the blue color indicate water bearing sand.

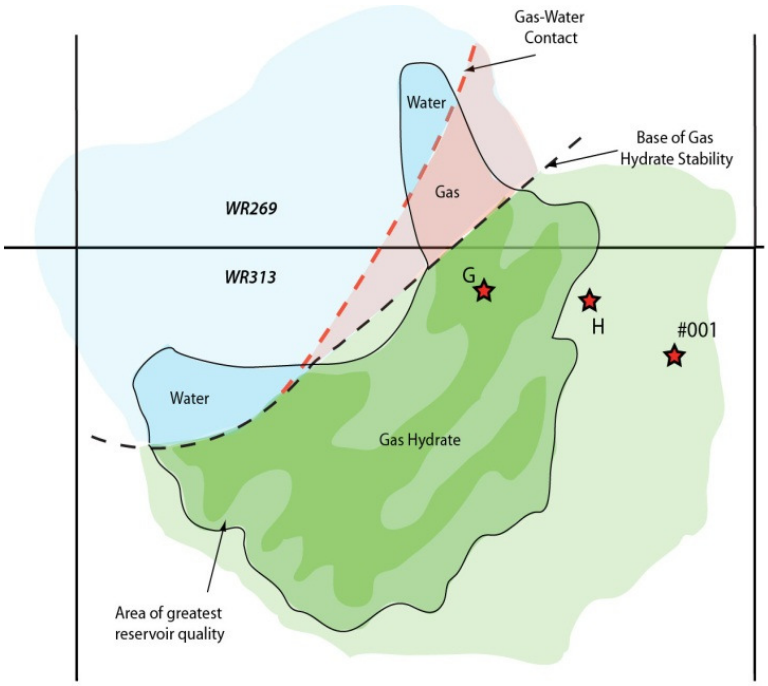

(a)

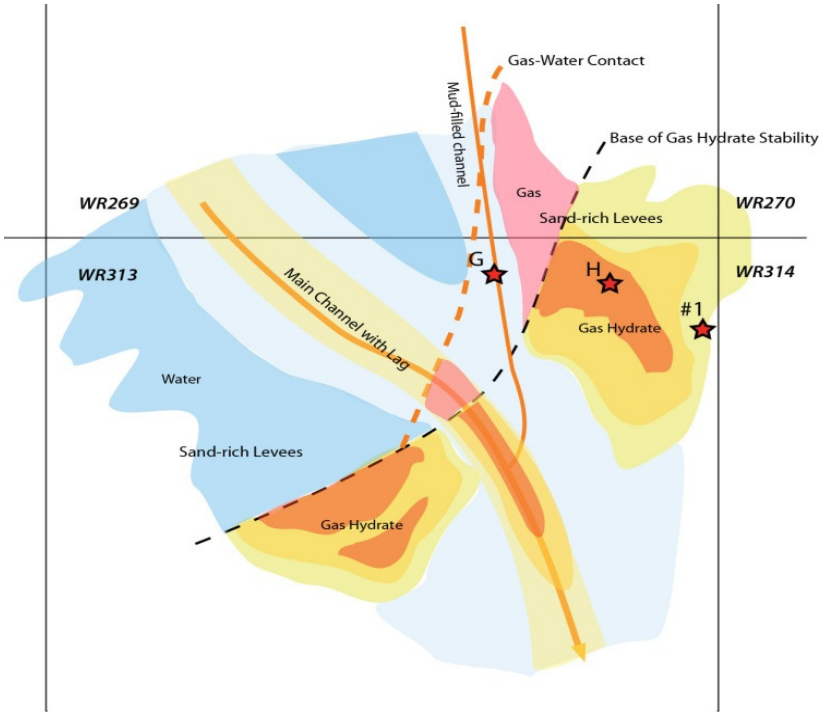

(b)

Figure 5.6 Schematic representation of Isopach map showing (a) Blue sand hydrate deposit (b) Orange sand hydrate deposit. The stars indicate well penetrations

5.2 3-D Reservoir Model description

The objective of this simulation effort is to assess the production potential from the Walker Ridge 313 site in the Gulf of Mexico using a conventional vertical well design and the depressurization method. A vertical well was preferred in this study due to unconfined nature of the sand bodies as shown in Figure 5.4 and Figure 5.5. A complex, dipping 3-D reservoir model is created and subsequently simulated for the Orange and Blue hydrate-bearing sands in the Walker Ridge 313 block. 3-D modeling enables to precisely predict flow patterns which might substantially affect the gas production. The 3D modeling potentially provides more representative results when a reservoir description contains a high degree of variability in both the horizontal and vertical dimensions. Moridis et al.(Moridis et al., 2010) conducted a preliminary evaluation of WR 313 site Gulf of Mexico using a simple 2-D model and suggested that the gas production rates can exceed 10 MMSCF/day. Structural dip which plays an important role at dip angles greater than 10º was neglected in the study by Moridis et al.

The 3-D models used for simulations are based upon the diagrammatic illustrations shown in Figure 5.6. The first step in this study is to digitize the hydrate saturation images of Blue and Orange sands of Walker Ridge 313 using ArcGIS (ESRI, 2001). Figure 5.7 shows the digitized images of Blue and Orange horizons. The digitized map is exported into Petrel (Petrel, 2011) to build reservoir models. A complete suite of well logs is also imported into Petrel to pick Blue and Orange sands using the resistivity and gamma ray logs. The top of Blue and Orange sands is picked for both the wells as shown in Figure 5.8. A non-orthogonal corner point grid is used for 3-D models. A total number of 37 zones and 55 layers are defined to incorporate vertical heterogeneity. Figure 5.9 is the schematic representation of the process involved in building 3-D reservoir models. The vertical heterogeneity is incorporated based on LWD data. Resistivity log

data is used as a primary source of information to estimate hydrate distributions in the Blue and Orange deposits at WR 313 wells, namely the G and H wells. The LWD resistivity logs are interpreted and hydrate saturations are calculated from the resistivity logs using Archie's Law (Archie, 1942) with exponents of n=1.5 at every 0.1 ft. Then, the calculated resistivity-log saturations are superimposed with the 1-ft resolution hydrate depositions estimated from the suite of log data.

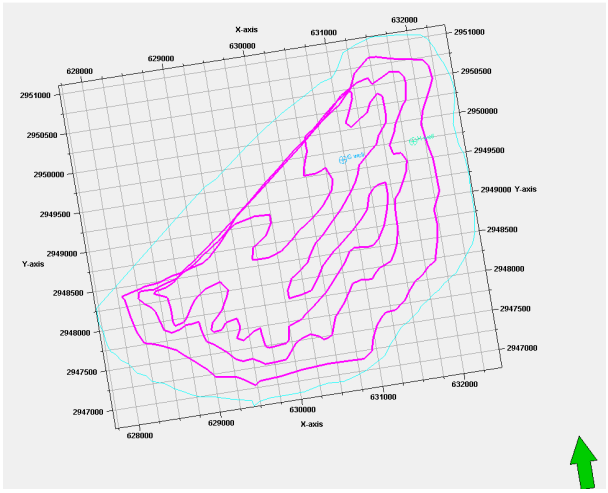

(a)

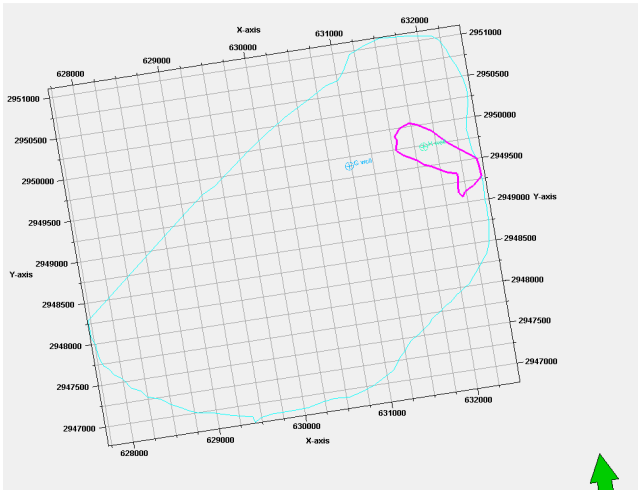

(b)

Figure 5.7 Digitized top view images of (a) Blue and (b) Orange horizons (see Figure 5.3)

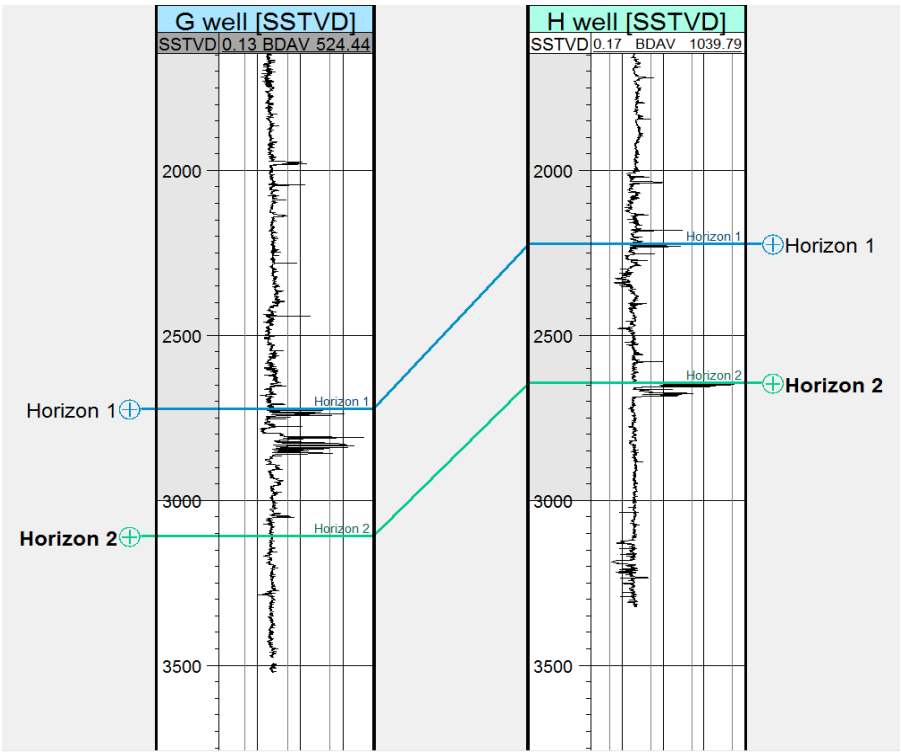

Figure 5.8 Cross section of G and H wells showing Resistivity top Picks of Blue and Orange Sand.

Figure 5.10 and 5.11 shows hydrate saturation distributions calculated using Archie's equation for Blue and Orange hydrate deposit. The red blocks in Figure 5.10 and 5.11 represents 1-ft layers of variable gas hydrate saturation.

The van Genuchten (Equation 32) (Van Genuchten, 1980) capillary pressure model is used to express the relationship between gas aqueous capillary pressure head and the aqueous saturation:

$$\bar{s}_l = \frac{(S_l - S_{lr})}{(1 - S_{lr})} = \left(1 - \left(\alpha\beta_{gl}\left(\frac{P_g - P_l}{\rho_l g}\right)\right)^n\right)^m \tag{32}$$

and the modified Stone three-phase model (Equation 33 and 34) (Aziz and Settari, 1979; Stone, 1970) is used for calculating relative permeabilities

$$K_{rl} = (\bar{s}_l)^n, K_{rG} = (\bar{s}_l)^m \tag{33}$$

$$\bar{s}_l = \frac{(S_l - S_{lr})}{(1 - S_{lr})}\ \bar{s}_g = \frac{(S_G - S_{irG})}{(1 - S_{irG})} \tag{34}$$

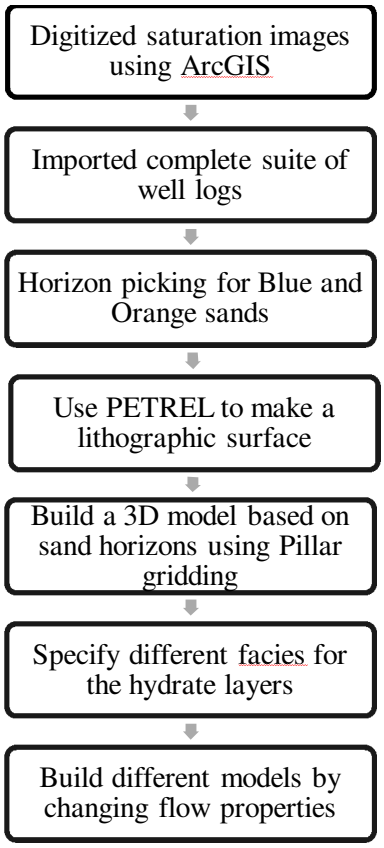

Figure 5.9 Schematic representation of process involved in building 3D reservoir models.

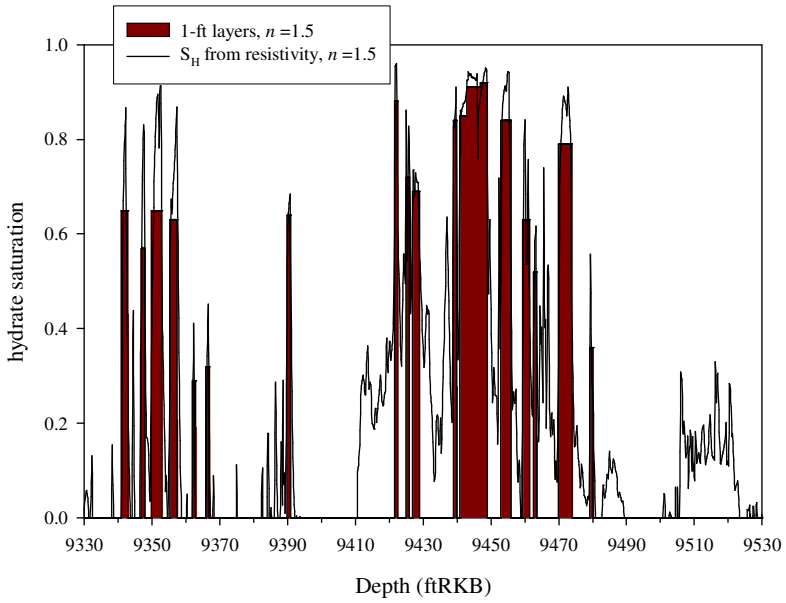

Figure 5.10 Hydrate saturation estimated using *n* = 1.5 in the Archie's equation for the Walker Ridge G well penetrating into the Blue sand. 1-ft layers correspond to the layer thickness used in the reservoir models. The red blocks represent 1-ft layers of variable

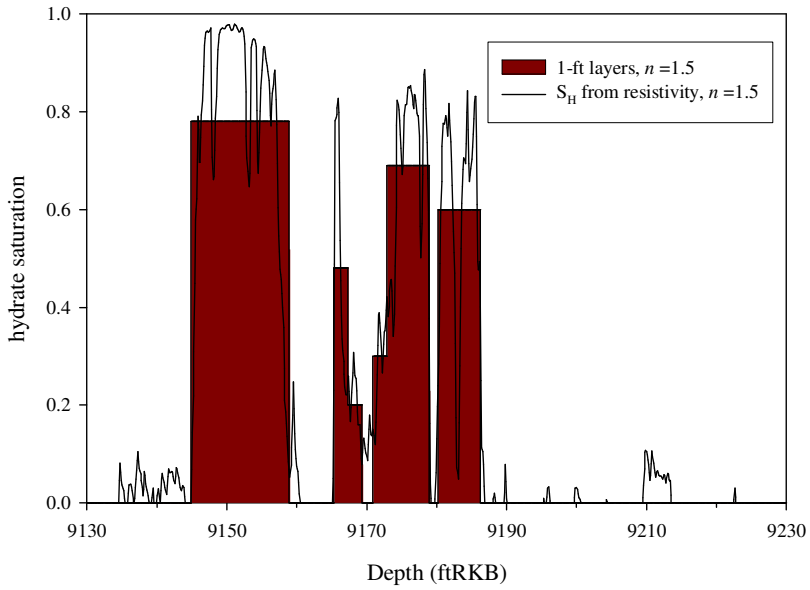

Figure 5.11 Hydrate saturation estimated using n = 1.5 in the Archie's equation for the Walker Ridge H well penetrating into Orange deposit. The red blocks represent 1-ft layers of variable gas hydrate saturation

Where $\overline{s}_l$ is effective aqueous saturation, $\bar{s}_g$ is effective gas saturation, S_l is aqueous saturation, S_{lr} is irreducible aqueous saturation, $\alpha, \beta_{gl}\ n, m$ are reference parameters. k_{rl} is aqueous relative permeability. k_{rG} is gas relative permeability. In the absence of reliable estimates of parameters of relative permeability and capillary pressure functions for the GOM hydrate accumulations, the parameters derived for the Mount Elbert permafrost hydrate deposit are used in the simulations. The parameters for relative permeability and capillary pressure functions were determined through history matching of a mutli-stage well test from the Mount Elbert stratigraphic test well using Schlumberger's Modular Dynamics Formation Tester (MDT) wire-line tool (Anderson et al., 2008). All reservoir parameters for the simulations are listed in Table 5.1. Permeable shale layers of porosity 1% and an absolute vertical permeability of 0.01 mD are specified in the simulation to represent clay rich sediments which has high porosity and low permeabilities. Initial reservoir temperatures are estimated using an average geothermal gradient of 19.6ºC/km.

Table 5.1 Reservoir properties for WR 313 site, Gulf of Mexico

Property	Value/Source
Hydrate bearing sediment (HBS) - saturations	Derived from well logs using Archie's Equation
Permeability-HBS	1000 mD horizontal , 100 mD vertical
Average Porosity of HBS	0.4
Shale layer – Porosity & Permeability	Porosity = 0.01, k_i=0.01mD, $k_i = k_j$, k_k =0.1 k_i
Rock Density	2600 kg/m^3
Rock Specific cheat	1000 J/kg K
Dry Thermal Conductivity	2.0 W/m K
Pore Compressibility	10^{-9} Pa^{-1}
Composite Thermal Conductivity Model	linear
Capillary Pressure Model	Van Genuchten Equation – Equation 32
α	10.204 (m^{-1})
β_{gl}	1
S_{lr}	0.28
n	4.432
m	0.7744
Aqueous Relative Permeability Model	Stone + Aziz – Equation 33, 34
S_{irA}	0.2
n	4.20
Gas Relative Permeability Model	Stone + Aziz – Equation 33, 34
S_{irG}	0.02
n	3.16

Figure 5.12 (a) shows the Blue and Orange sand models with hydrate saturation distribution adapted from Figure 5.3 and 5.6. The reservoir is dipping from NW to SE. The thickness of the sand varies laterally with red region (75% hydrate saturation in Figure 5.12(a)) being the thickest sand followd by green and blue. A partial lateral heterogeneity has been introduced using the seismic hydrate saturation images seen in Figure 5.3. The focus being gas production from G and H wells, a sub model is extracted surrounding the G and H wells. Figure 5.12(b) shows the depth of the extracted sub model.The reservoir dimensions ($i \times j$) of the extracted sub model are 1.8 × 2.5 km (5900 × 8200 ft) where i is in the direction of x-axis and j in direction of y-axis. The thickness of the underburden and overburden shale are 50 m (164 ft). Null blocks have been introduced in the model between Blue and Orange sands to reduce computation time for simulations. Figure 5.13 (a) shows 3-D view of the extracted model showing Blue and Orange hydrate layers. The total volume of hydrate per unit area is defined as a product of hydrate saturation, porosity of the block and net pay (thickness of hydrate bearing sediment as shown in Equation 35. Figure 5.13 (b) shows 2-D view of total volume of hydrate per unit area.

$$\frac{Volume\ of\ hydrate}{Areal\ extent\ of\ sand}(ft)$$

$$= S_H\left[\frac{Volume\ of\ hydrate}{volume\ of\ pore\ space}\right] \times \text{Porosity}\left[\frac{Volume\ of\ pore\ space}{volume\ of\ sand}\right]$$

$$\times [Thickness\ of\ HBS\ ] \tag{35}$$

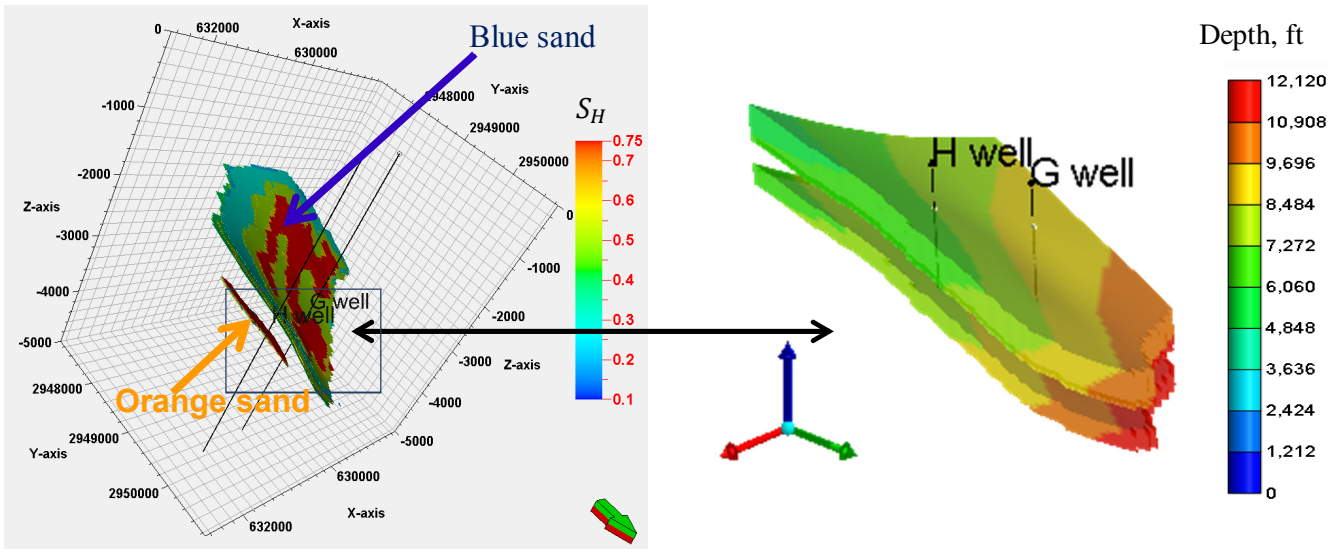

a) b)

Figure 5.12 a) Blue and Orange hydrate deposit showing hydrate saturation b) Extracted reservoir sub model displaying depth for flow simulations.

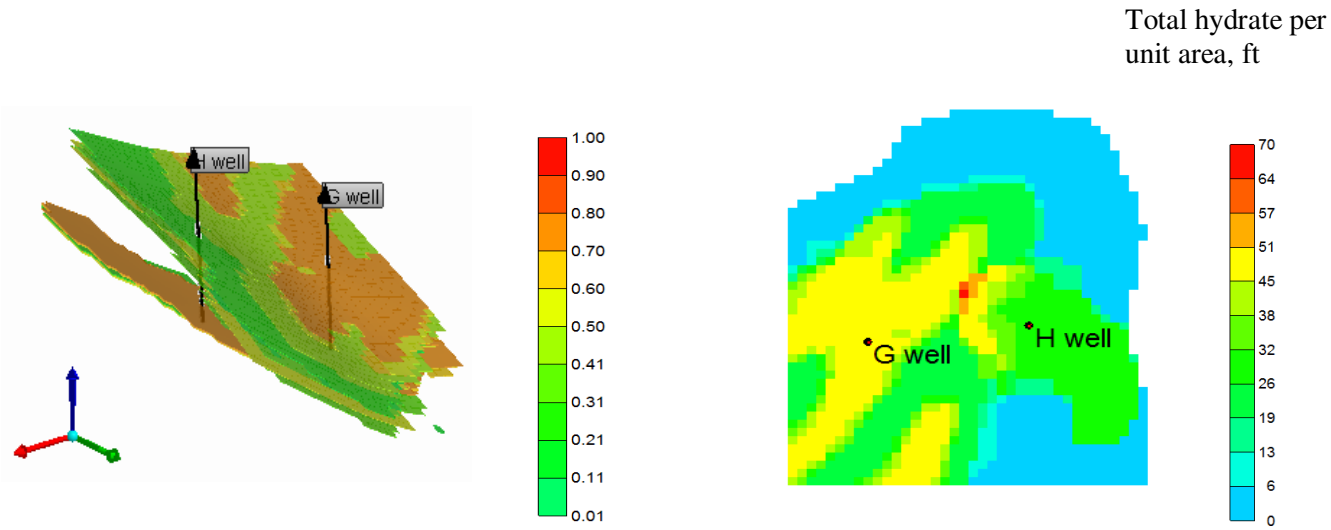

(a) (b)

Figure 5.13 a) Dipping hydrate layers for the extracted reservoir model showing G and H wells b) 2-D view of the total hydrate per unit area (see Equation 35)

5.3 Results and Discussion

One of the major challenges faced in simulating gas production from the reservoir was secondary hydrate and ice formation. Ice can form in the reservoir due to excessive cooling caused by the endothermic nature of hydrate dissociation. Ice formation in the reservoir model can be theoretically avoided by specifying a constant bottomhole pressure of 2700 kPa (393 psi).

Secondary hydrate formation around the well bore has been observed as seen in previous numerical studies by Moridis et al.(Moridis et al., 2010) and Myshakin et al. (Myshakin et al., 2011). Figure 4.14 shows the hydrate reformation (secondary hydrate) around the wellbore. To avoid secondary hydrate formation around the wellbore which blocks further flow of fluids into the well, the well bore has been heated to 150 W/m.

Figure 5.15 and 5.16 reflects the gas and water production from G and H wells. The gas production for both G and H wells started instantaneously without any lag. The gas production for G well reached a maximum of 65 MMscf/day in 0.7 years (255 days) and gradually decreased to 3.5 MMscf/day in 5 years. The uppermost hydrate layers and layers with hydrate saturation less than 60% dissociated first contributing to the first 5 years of production. Hydrate layers with hydrate saturation greater than or equal to 75% did not contribute in the first 5 years of production. Figure 5.18 shows hydrate dissociation pattern and snapshots of total hydrate per unit area at a) t = 0 days, b) t = 5 years, c) t = 10 years and d) t = 20 years. The total hydrate per unit area around G well reduced approximately to 22 ft from 46 ft in a span of 20 years, whereas for H well it reduced to 7 ft from 32 ft.

The H well produced gas earlier than the G well due to early depressurization of the reservoir area surrounding the H well. The average initial hydrate saturation for the upper blue sand at H well was 0.4. The availability of water can be cited as a reason for early depressurization of the

H well. The gas production for H well reached a maximum of 60 MMscf/day in 0.17 years (62 days) and reduced gradually to 3 MMscf/day in 2 years. A pattern of sudden increase in gas production and then a gradual decrease is observed for both G and H wells. The water production for both wells is shown in Figure 5.16. The H well started with a high water production of 10,000 bbl/day due to availability of water in the upper blue sand and also due to the well being operated at a constant bottomhole pressure. The initial water production for the G well was very low when compared to the H well. The water production for H well gradually increased to a maximum of 7000 bbl/day. High water production is attributed to the permeable shale layers and high horizontal permeabilities.

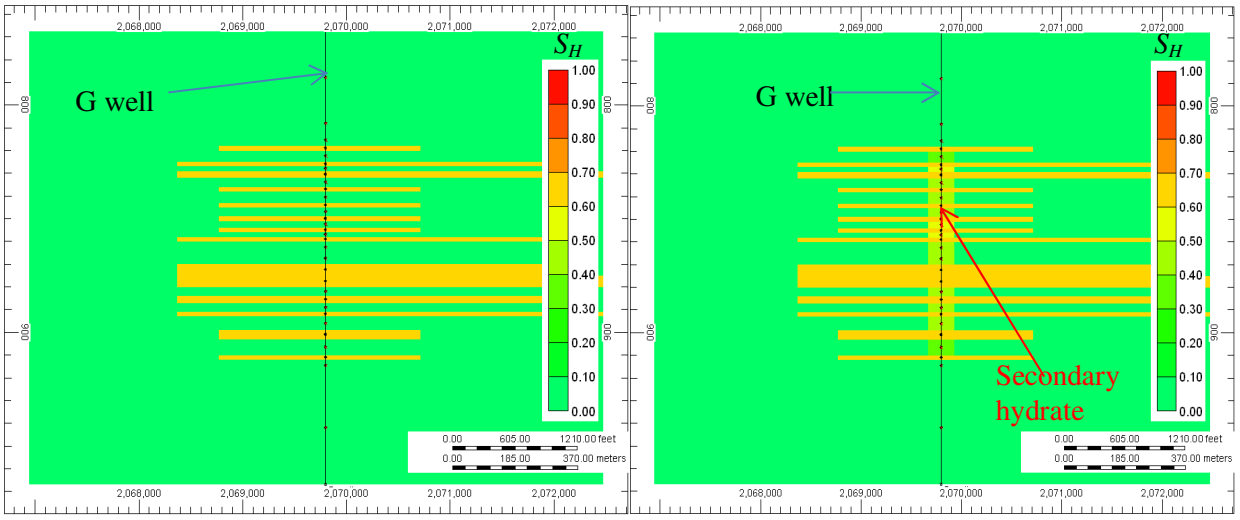

(a) (b)

Figure 5.14 G well Xsection showing evolution of secondary hydrate (a) t = 0 (b) t = 300 days

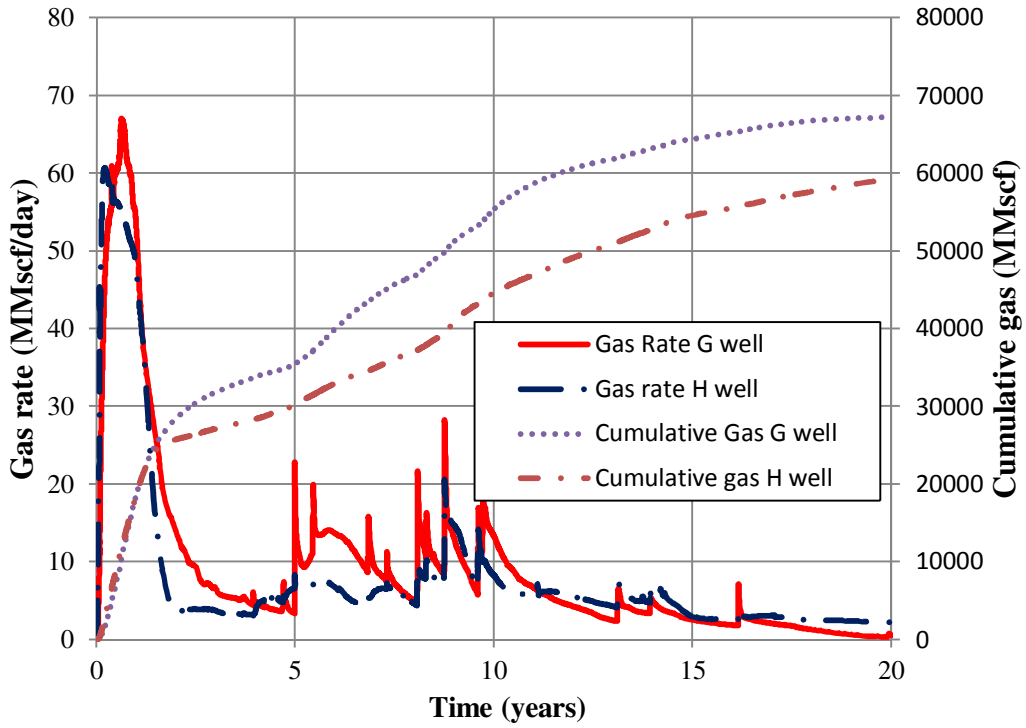

Figure 5.15 Gas rate and cumulative production for G and H wells

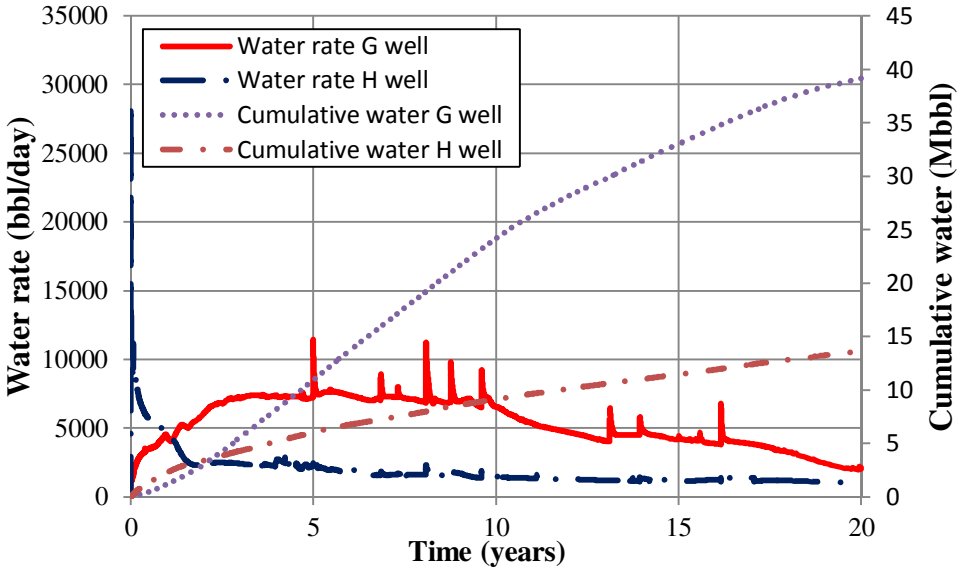

Figure 5.16 Water rate and cumulative production for G and H wells

Gas water ratios (GWR) for G and H wells are shown in Figure 5.17. The GWR for G well reaches a maximum value of 18 Mscf/bbl while GWR for H well reaches a maximum of 10 Mscf/bbl.

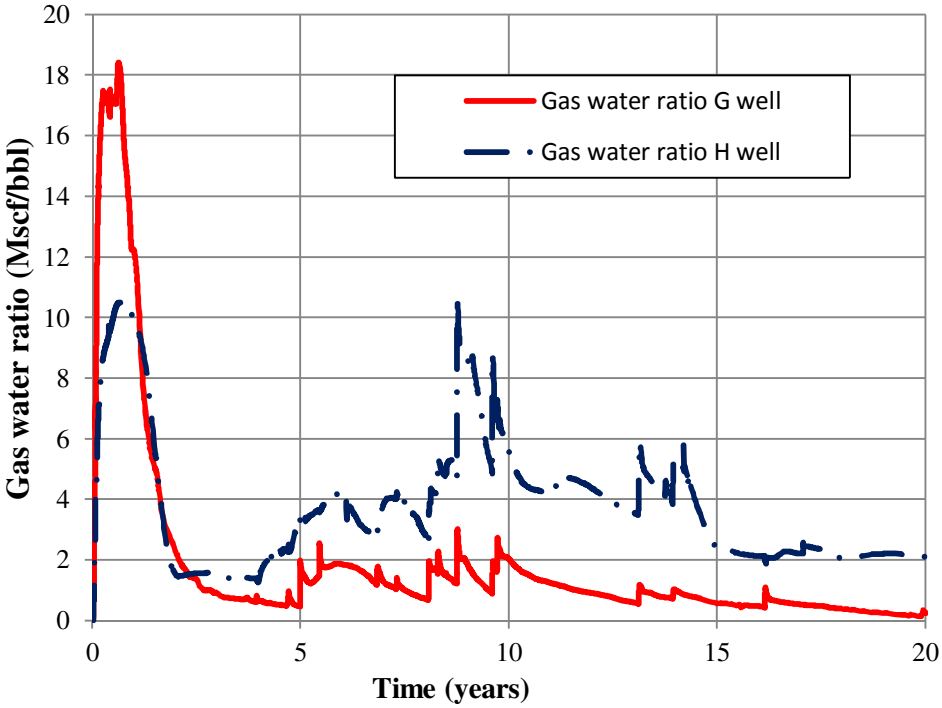

Figure 5.17 Gas water ratio for G and H wells

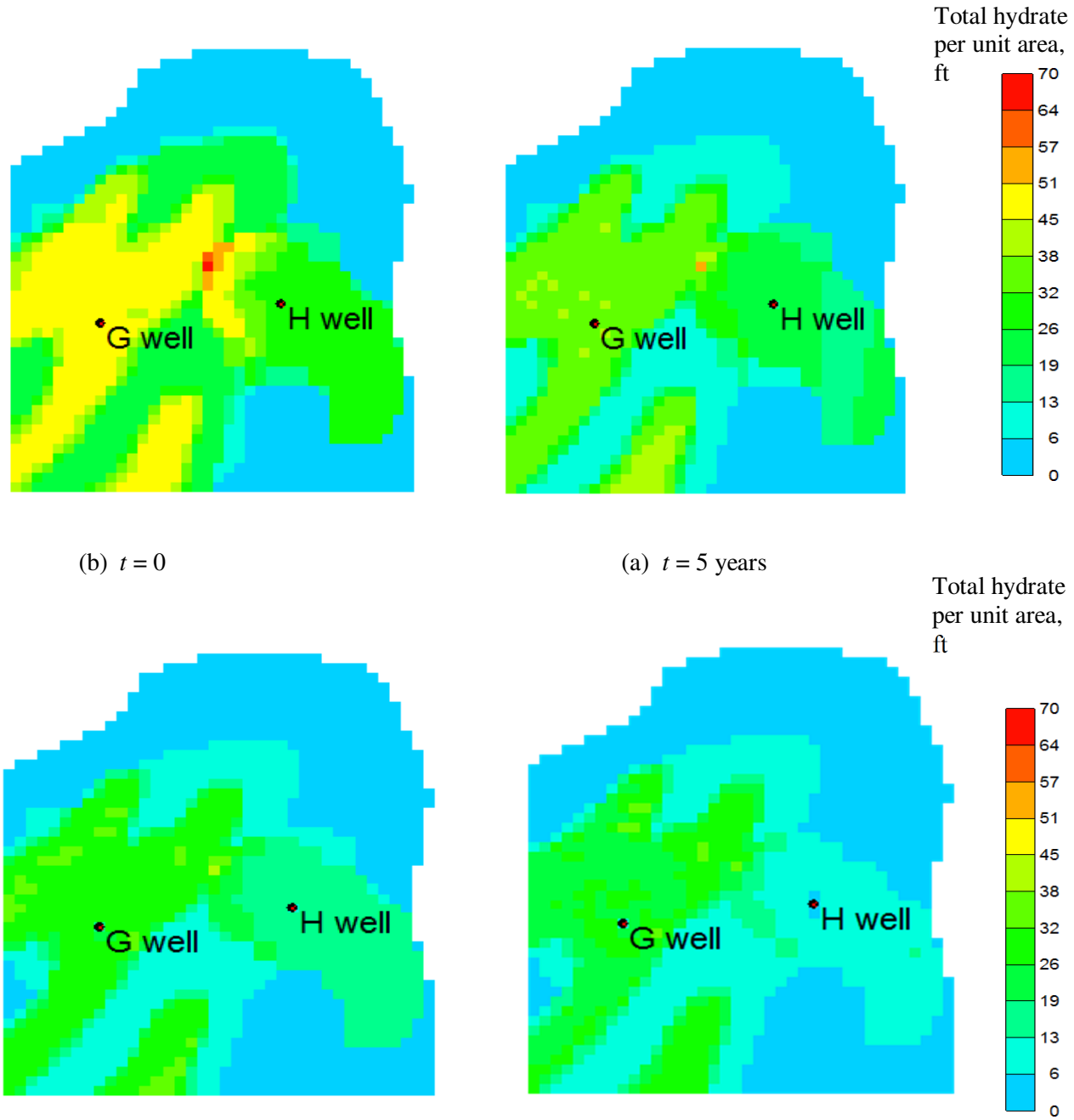

Figure 5.18 2-D snapshots of total hydrate per unit area in feet at (a) t = 0 days (b) t = 5 years (c) t = 10 years and (d) t = 20 years

Figure 5.19 shows the hydrate saturation snapshots at a) t = 0 days, b) t = 5 years, c) t= 10 years and d) t = 20 years. Hydrate dissociation is an endothermic process which also favors secondary hydrate formation as the simulation progress in time as shown in Figure 5.19.

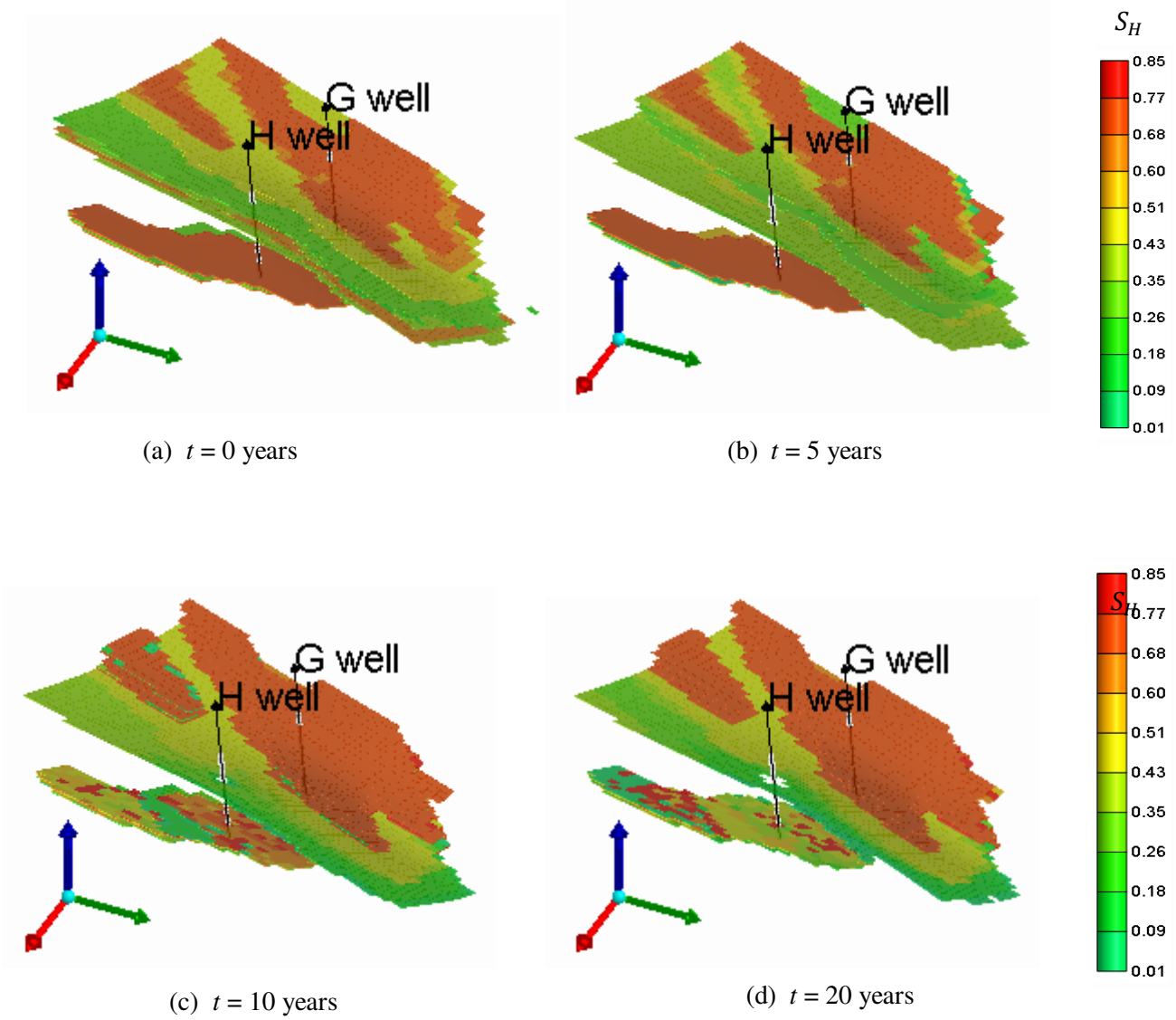

Figure 5.19 3-D snapshots of hydrate saturation, S_H at (a) t = 0 days (b) t = 5 years (c) t = 10 years and (d) t = 20 years

The profiles for well block pressure in Figure 5.20 shows the change in well block pressure due to depressurization for G and H wells.

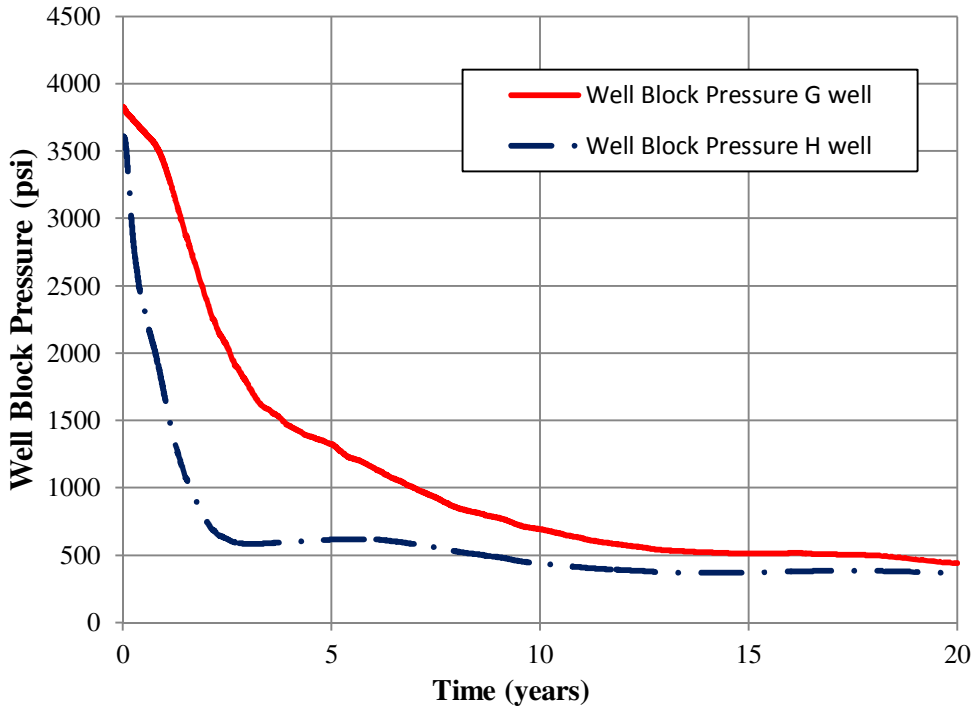

Figure 5.20 Well block pressure profiles for G and H wells.

The well block pressure of H well reduced drastically from 3600 psi to 580 psi in 3 years due to high water production in the first 3 years. Well block pressure for G well reduced from 3800 psi to 1700 psi in 3 years due to low water production. Secondary hydrate formation and high quality gas hydrate sand around G well is the reason behind low water production.

5.4 Uncertainty Assessment of WR 313 G well

The objective of this study is to estimate the uncertainty in gas production that could arise from the uncertainty in the reservoir parameters. Uncertainty propagation can be studied using a variety of methods, the most popular being a Monte Carlo procedure. A Latin hyper cube sampling (Section 3.1) is a process applied for multiple variables to reduce the number of required simulations necessary for a Monte-Carlo simulation. In this method sample values for each uncertain variable are generated using a probability distribution and then the sample values are randomly grouped to create a job pattern for each simulation. The Latin hypercube sampling parameters for WR 313G well is different from the sampling parameters described in Section 3.1. In this study the sampling parameters are selected around the base model to understand the effect of uncertainty in all reservoir parameters, whereas in Section 3.1 the sampling parameters were designed to understand the effect of shale permeability (k_{shale}) on gas production.

An initial Monte Carlo study is performed to understand the behavior of the reservoir model and to gain perspectives on the most important variables with respect to uncertainty in gas production. The base run used for the uncertainty study is same as the reservoir model used in Section 5.3 of this study. Bottom-hole pressure, permeability and porosity are the uncertain parameters in this study. Hydrate saturation, reservoir pressure, temperature and lithology which are specific to the Walker Ridge 313 hydrate deposit are not treated as uncertain parameters due to limited data. All other parameters are same as in Section 5.3 of this study. Latin hypercube sampling is a widely used technique for the propagation of uncertainty analysis for a complex system. In Latin hypercube sampling the input variables are considered to be random variables with known distribution functions. A basic Latin hypercube design of 25 runs with 3 verification runs is used in the uncertainty assessment.

A truncated normal distribution is used for three uncertain parameters (a) porosity, (b) bottomhole pressure and (c) absolute permeability. The shaded area in Figure 5.21 shows the distributions of the three parameters (a) porosity (b) bottom hole pressure and (c) absolute permeability in *i* direction. For each parameter five sample values are generated with probabilities (a) P (2.5), (b) P(25), (c) P(50), (d) P(75) and (e) P(97.5) from the distribution shown in Figure 5.21. The five sample values for each input variable are denoted as '00', '01', '02', '03', and '04'. For each of the 25 runs in the Latin hypercube design a sample value from each input variable is randomly chosen. Table 5.2 illustrates the five sample values with probability distribution picked for each input variable. The design job pattern for each run is shown in Table 3. The job pattern for run 1 in Table 3 is denoted as "020404". It represents the simulation run with '02' (P(25)) of Porosity, '04' (P(97.5)) of Absolute permeability and '04' (P(97.5)) of Bottom hole pressure.

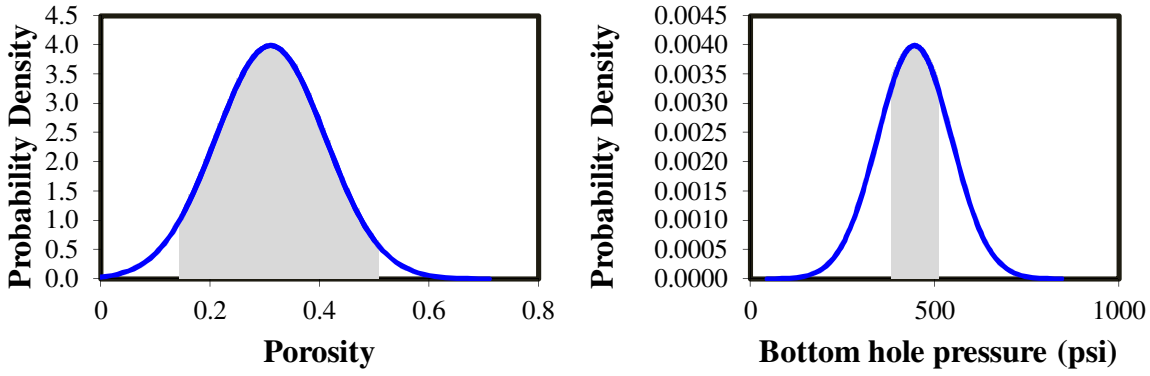

(a) (b)

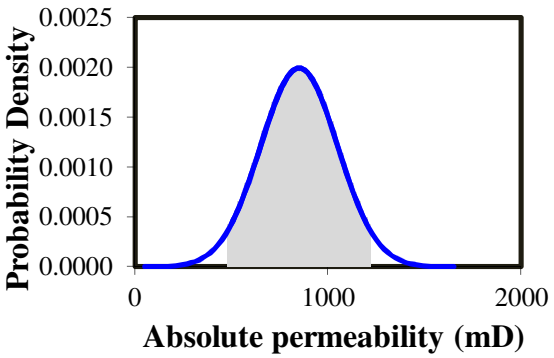

(c)

Figure 5.21 Truncated normal distributions of uncertain variables (a) Porosity, (b) Bottom hole pressure and (c) Absolute permeability

Table 5.2 Sampling of Input parameters

no	Probability	Porosity	Bottom hole Pressure (psi)	Absolute Permeability I (mD)
	Percentile	$\mu = 0.31$, $\sigma = 0.1$, (Min, Max) = 0.1,0.47	$\mu = 445$, $\sigma = 100$, (Min, Max) = 393,500	$\mu = 850$, $\sigma = 200$, (Min, Max) = 500,1200
1	P2.5	0.17955	393	561.67
2	P25	0.27879	418	765.27
3	P50	0.33839	445	888.94
4	P75	0.39383	471	1008.1
5	P97.5	0.45959	496	1168.8

Table 5.3 Design pattern for Latin hyper cube sampling

No	Pattern	Porosity	Absolute permeability, *I* (mD)	Bottom hole pressure (psi)
1	20404	0.33839	1168.8	496
2	40300	0.45959	1008.1	393
3	30403	0.39383	1168.8	471
4	30401	0.39383	1168.8	418
5	40101	0.45959	765.27	418
6	10200	0.27879	888.94	393
7	30104	0.39383	765.27	496
8	00201	0.17955	888.94	418
9	20304	0.33839	1008.1	496

10	40104	0.45959	765.27	496
11	10400	0.27879	1168.8	393
12	00001	0.17955	561.67	418
13	00003	0.17955	561.67	471
14	00302	0.17955	1008.1	445
15	10303	0.27879	1008.1	471
16	10002	0.27879	561.67	445
17	00404	0.17955	1168.8	496
18	20300	0.33839	1008.1	393
19	20102	0.33839	765.27	445
20	10003	0.27879	561.67	471
21	20200	0.33839	888.94	393
22	30203	0.39383	888.94	471
23	30001	0.39383	561.67	418
24	40202	0.45959	888.94	445
25	40102	0.45959	765.27	445

It is difficult to show the results of all 28 simulations in one graph; therefore, similar results are combined into one run. The thickness of the line is proportional to the number of runs coalesced. Figure 5.22 shows the representative gas rates of the simulations and shows a distribution of all runs. The base run is same as in Section 5.3 and is shown in red. The thick blue dotted line in Figure 5.21 represents 21 runs. The gas rate for most of the runs as indicated in Figure 5.22 has reached a maximum of 44 MMscf/day in 0.41 years (150 days) . The gas rates of most of the runs in the model have decreased by about 30% from the base run in the first five years as shown in Figure 5.22. Gas-water ratios remained consistent to that of the base run (Figure 5.22) due to consistent decrease in both gas and water production. Similar to Figure 5.21, similar results have been coalesced and a thicker line shows more runs following that line. Cumulative gas production and cumulative water production are shown in Figure 5.24 and Figure 5.25.

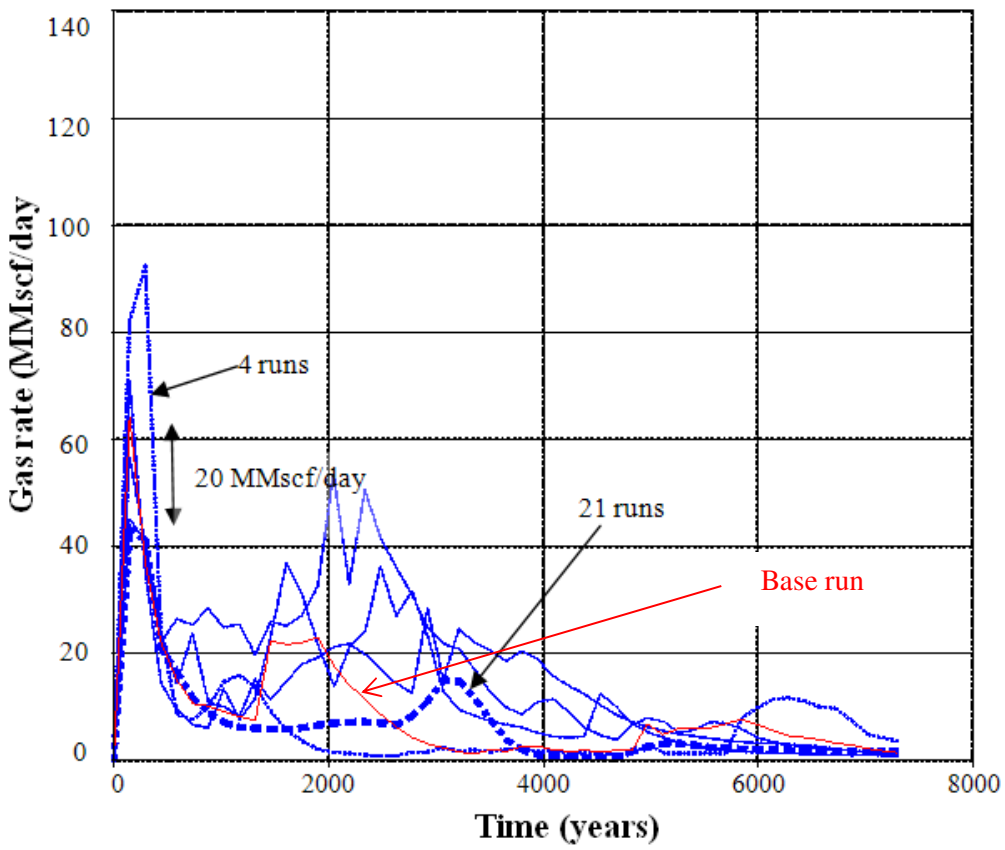

Figure 5.22 Representative gas rates for Monte Carlo runs. The base run is shown in red. The thickest line indicates 21 runs that are close to the same run.

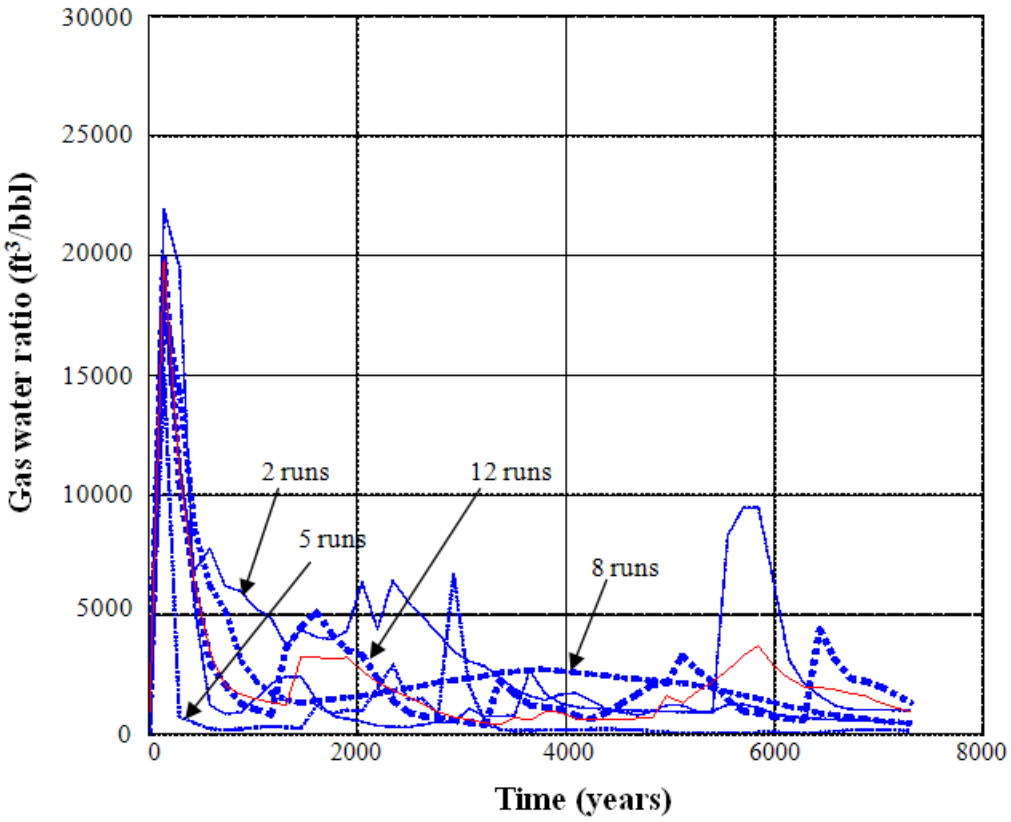

Figure 5.23 Gas-Water Ratio of the Monte Carlo runs. The base run is shown in red. The line thickness is proportional to the number of run following the same pattern. The thickest blue dotted line represents 12 runs.

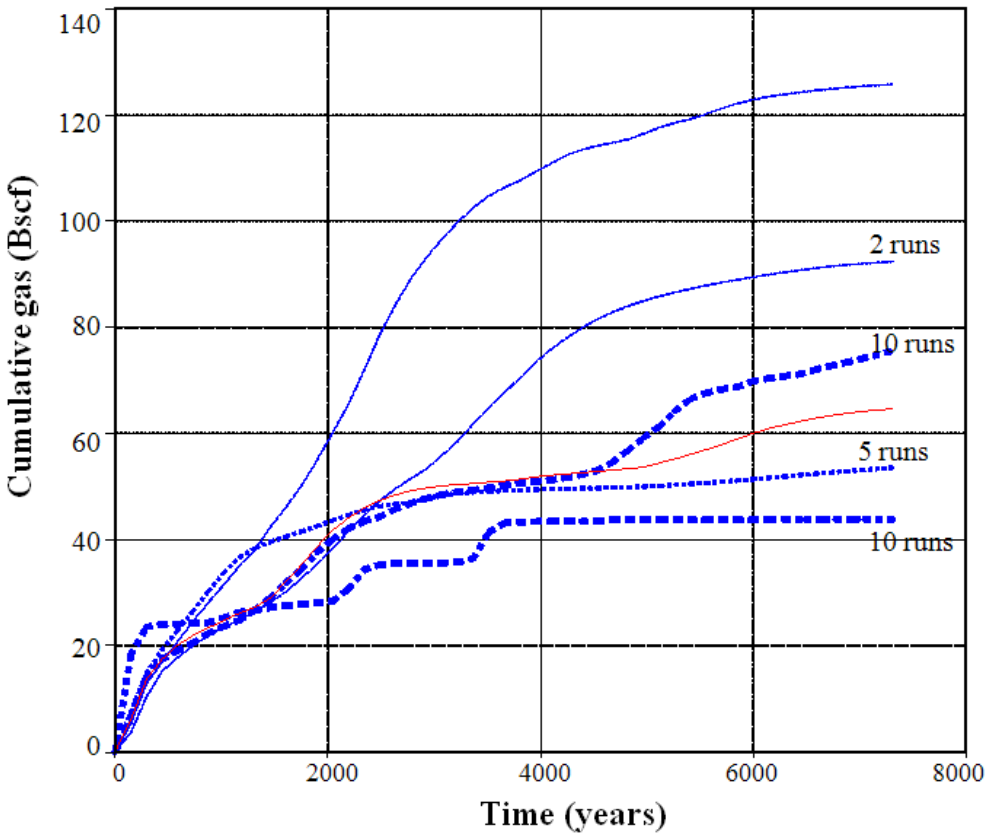

Figure 5.24 Cumulative gas rates of the Monte Carlo runs.

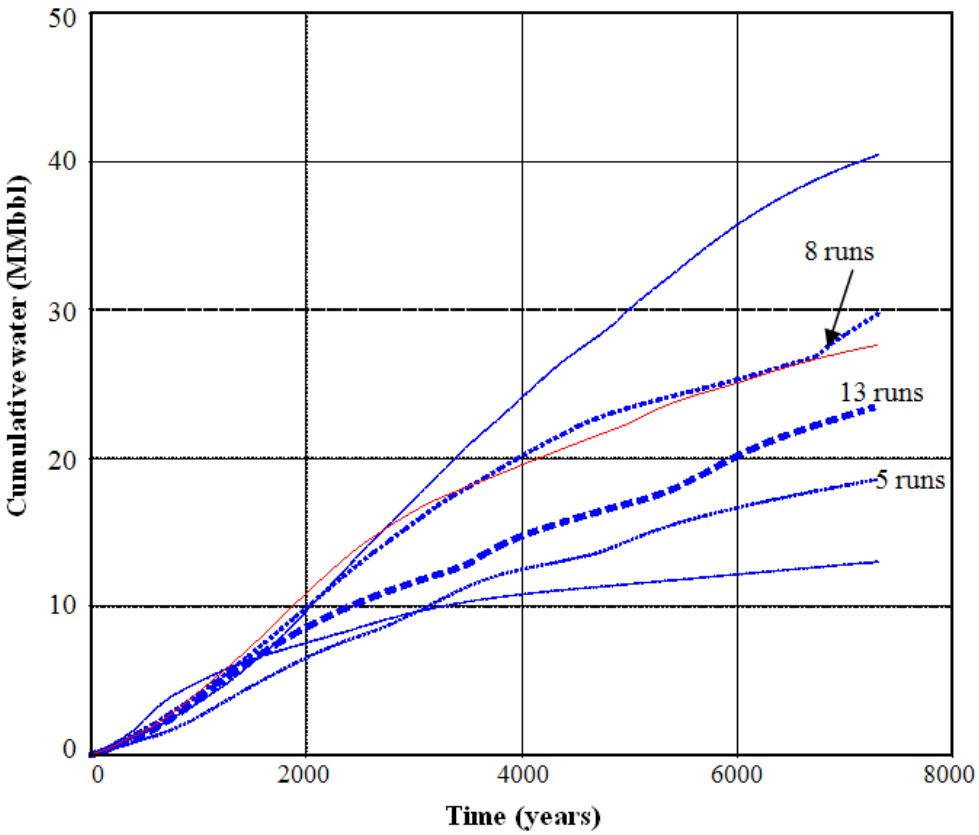

Figure 5.25 Cumulative rate of Monte-Carlo (Latin hypercube) runs

To do this, the gas production rates are discounted to 15%. The effects of each uncertain parameter on the discounted gas rate are calculated. A quadratic model is used to fit the discounted gas rate as the output variable to uncertain variables porosity, permeability and bottom hole pressure in this study. Equation 7 represents as simple quadratic model

$$y = a_0 + \sum_{j=1}^{n} a_j x_j + \sum_{j=1}^{n} a_{jj} {x_j}^2 + \sum_{i<j} \sum_{j=2}^{n} a_{ij} x_i x_j \qquad (36)$$

Where y is output variable (discounted gas rate), x_j are linear effects of parameter (porosity, bottomhole pressure and absolute permeability), ${x_j}^2$ are quadratic effects and $x_i x_j$ are interaction effects. All the parameters are scaled to have a range from -1 to 1. Figure 5.25 represents a

tornado plot showing quadratic model effects estimated. The Y axis in the tornado plot is parameter effect (linear, interaction and quadratic effects) and the X axis denotes response change in disounted gas rate. The tornado plot shows the actual predicted response change in discounted gas rate as the parameter travels from a smallest sample value to the largest sample value. Permeability has the highest positive effect, followed by porosity and bottomhole pressure which has a negative effect. The maximum and minimum values of discounted gas rates obtained from the range of factors considered can also been seen in the said tornado plot shown in Figure 5.26.

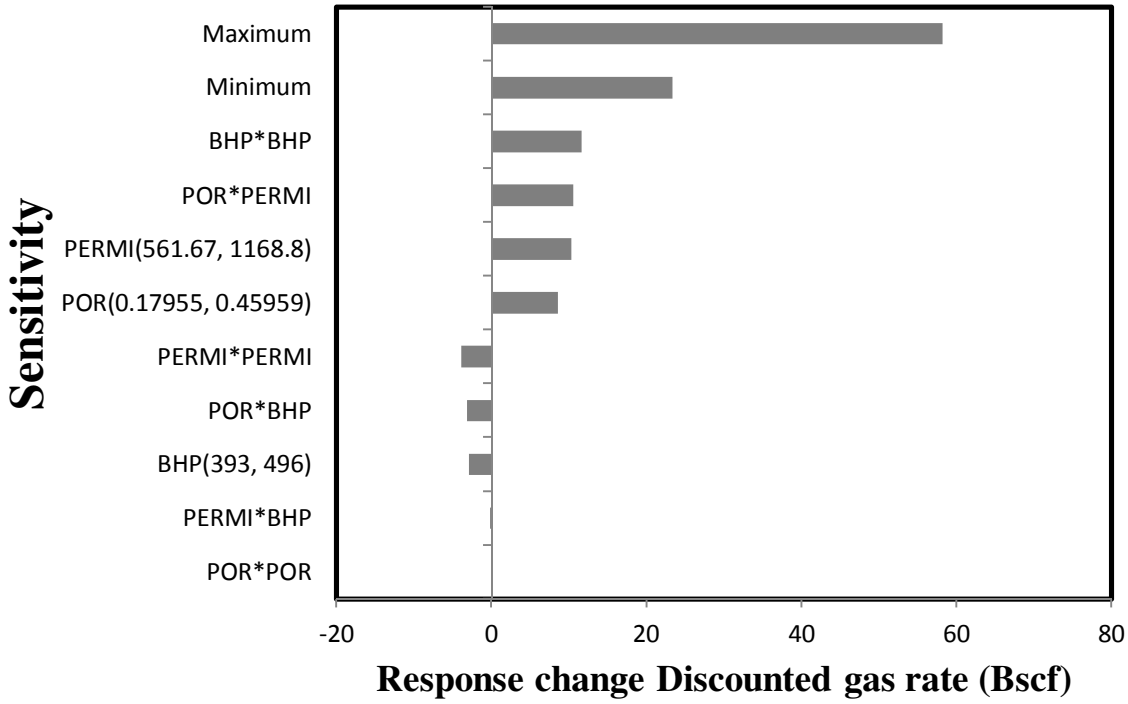

Figure 5.26 Tornado plot showing effect of parameter on Discounted gas production

The net present value (NPV) of gas produced is calculated with variable total drilling and completion costs. Figure 5.27 shows cumulative probability density of the NPV of gas produced obtained by calculating against the current Henry Hub natural gas spot price. The average cost per well in a Gulf of Mexico offshore region dropped from $100 Million US to $80 Million US from 2008 to 2009 based on Joint Association Survey (JAS) data 2009 (JAS, 1976-2011)]. We have calculated NPV for three different drilling and completion costs (50, 80 and 100 Million USD). Different curves in Figure 5.27 represent NPV calculated using different drilling and completion costs. The 50th percentile of the NPV for a well cost of $80 MiilionUS is $16 MillionUS.

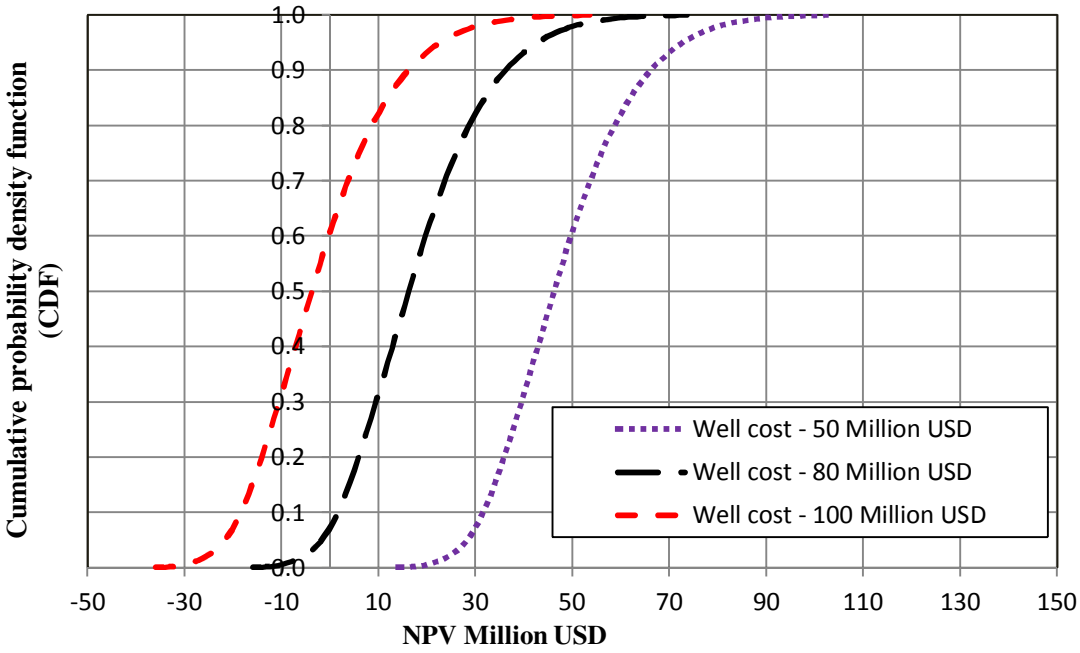

Figure 5.27 Cumulative Probability distribution function of NPV in Million USD

Conclusions:

The gas production potential of Gulf of Mexico Walker Ridge 313 Blue and Orange hydrate deposits is investigated. A complex dipping 3-D reservoir models are developed based on available well log and seismic data. Reservoir simulations predict that the Gulf of Mexico hydrate accumulations can produce at high rates using conventional wellbore completion. A secondary hydrate barrier around a wellbore was observed during gas production in 1 year of production. The secondary hydrate formation has to be avoided for flow of fluids into the well bore. Gas production from WR 313 reservoirs displays high rates that can reach 65 MMscf/day for G well and 60 MMscf/day for H well. Cumulative hydrate layer thickenss of 24 ft ("Initial 46 ft" –"Final 22 ft" = 24 ft) dissociated around G well, and 25 ft ("Initial 32 ft" – "Final 7 ft" = 25ft) around H well. Hence the similar gas production from both wells.

The uppermost hydrate layers and layers with hydrate saturation less than 60% dissociated quicker than the layer with higher hydrate saturations contributing to the first 5 years of production. Hydrate layers with high hydrate saturations up to 80% did not dissociate in the course of the simulation. An uncertainty assessment of Walker Ridge 313 G well is performed using a Latin hyper cube sampling method with porosity, bottom hole pressure and absolute permeability being the uncertain variables. The gas rates of a majority of the runs have decreased. The effect of uncertainty of porosity, permeability and bottom hole pressure on the discounted gas rate are studied. Permeability has the highest effect, followed by porosity and bottom hole pressure. The net present value is calculated based on different drilling and completion costs. The 50^{th} percentile of the NPV for a well cost of $80 Miilion U.S. is $16 Million U.S.

6. Geomechanical modeling using CMG STARS

6.1 Introduction

Methane hydrates contain significant amounts of hydrocarbons both arctic and deep water sediments due to the favorable pressure and temperature conditions. Many of these hydrate deposits can overlay active hydrocarbon production and many producing wellbores penetrate hydrate-bearing sediments. These sediments are usually unconsolidated. Shear strength is the most important property to be considered for sediment failure. Shear strength is defined as the maximum resistance of a soil to shear. The shear strength of hydrate bearing sediments is a function of hydrate saturation, with strength increasing with hydrate saturation the higher the hydrate saturation higher is its strength (Yun et al., 2007). When hydrate dissociates gas and water will be generated and will change the shear strength of the sediment. Hydrate dissociation can result in sediment failure, well bore instability, loss of foundations or even on a larger scale, slope failures. There are very few experimental studies relating to the strength of hydrate bearing sediments. The most cited study on methane hydrates was by Masui et al. (Masui et al., 2005) in which the dependence of different geomechanical properties on hydrate saturation was discussed. This simulation-based work is focused on assessing the potential disturbance of the *in situ* hydrate deposits by the production of hot hydrocarbon fluids through the wellbores.

Rutqvist et al. (Rutqvist, 2008) developed a numerical simulator (T+F) by integrating Tough/+Hydrate and a commercial code Flac3D (Itasca, 2004). Rutqvist et al. (Rutqvist et al., 2009b) performed geomechanical simulations for the stability of HBS in the vicinity of warm pipes. They have simulated a layered sequence of five hydrate formations; each of 40 m thick confined at the top and bottom by impermeable shale layers and calculated a total subsidence of

0.8 m and 4 m for Toyoura sand and clay respectively. They concluded that this huge subsidence can adversely affect integrity and stability of well bore assembly.

The thermal impact from an inclined borehole case was studied by Suntichai Sipngarmlert (Silpngarmlert, 2011) for the case of a 45-degree inclined producing well with a 30-foot thick hydrate-bearing interval. They observed hydrate dissociation up to a distance of 60 feet from the wellbore. In this work CMG STARS is validated with a more rigorous geomechanical model (T+F).

6.2 Validation of CMG STARS with T+F (TOUGH+Flac3D)

Rutqvist et al. (Rutqvist et al., 2009a) has done geomechanical simulations on Toyoura sand using TOUGH+Flac3D (T+F) model. It would be very beneficial to compare the results of CMG with the T+F model. The same geometry and properties are used as in Rutqvist et al. Figure 6.1 shows the pressure, temperature and hydrate saturation profiles around a hot wellbore generated using T+F model in 30 years. Figure 6.2 shows similar results generated using CMG STARS in this study.

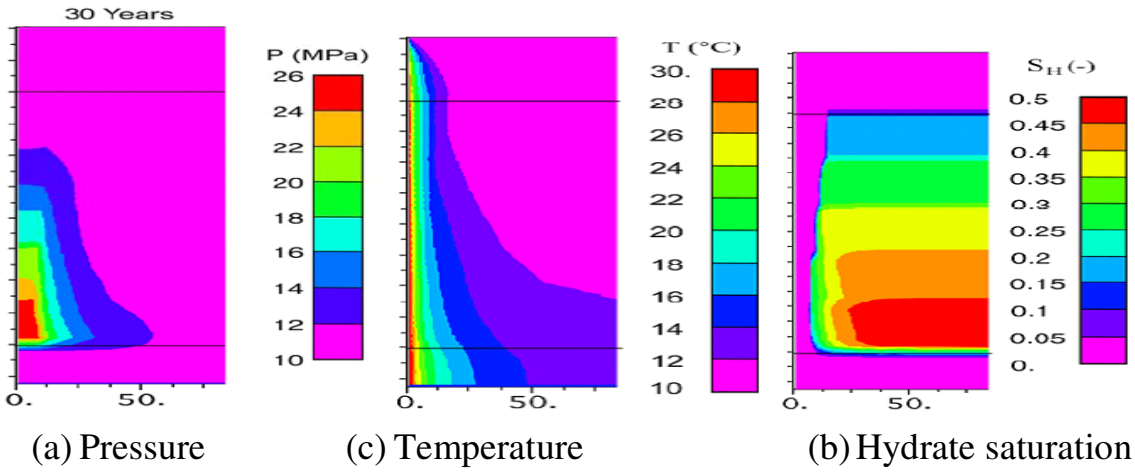

Figure 6.1 (a) Pressure, (b) temperature, (c) hydrate saturation profiles around a hot wellbore

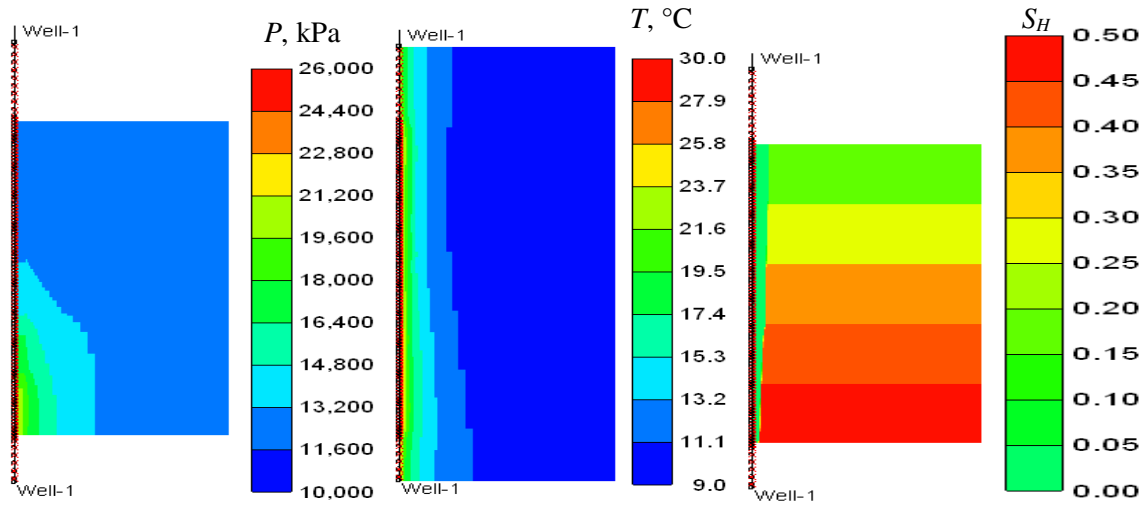

Figure 6.2 Pressure, temperature and hydrate saturation profiles for CMG STARS

Hydrate dissociates due to heat transfer from the hot well bore that produces oil at temperature of 30ºC. There is a lot of uncertainty associated with the geophysical and geomechanical properties of the hydrate bearing sediments. In this work, simulations of hydrate deposits in the immediate vicinity of heated wellbores will be performed under different lithologic settings to assess the potential response of the hydrate dissociation in the pore space. Sensitivity studies of different parameters on subsidence of the hydrate bearing sediment around the well bore are performed. The sensitivity variables are initial saturations, lithologic settings, porosity and permeability of shale boundaries and temperature of the hot hydrocarbon fluids in the wellbore. Considering the effect of different parameters, a worst case scenario is modeled.

6.3 Base Model Prudhoe Bay L pad

Potential consequences of a hot wellbore located within a hydrate deposit may include the dissociation of the hydrate and subsequent destabilization of the sediments surrounding the wellbore. For future exploration or field tests it is extremely important to predict the affected area around the wellbore due to hydrate dissociation. There are 55 wells drilled from Prudhoe Bay L-Pad in North Slope Alaska (see Figure 6.3) which produces hot crude oil. Figure 6.3 shows a schematic representation of the L-Pad. The wells from Pad as shown in Figure 6.4 are drilled through the hydrate formations (blue color in Figure 6.4).

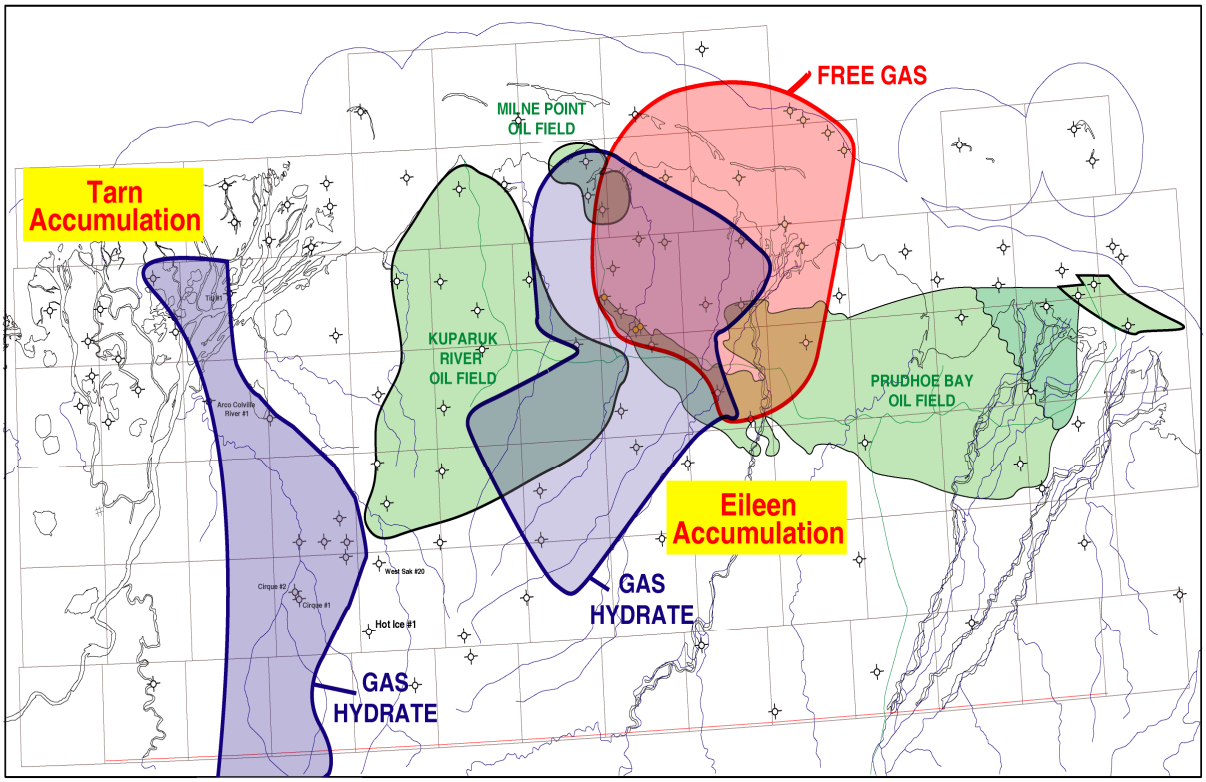

Figure 6.3 Gas hydrate accumulation in North slope of Alaska

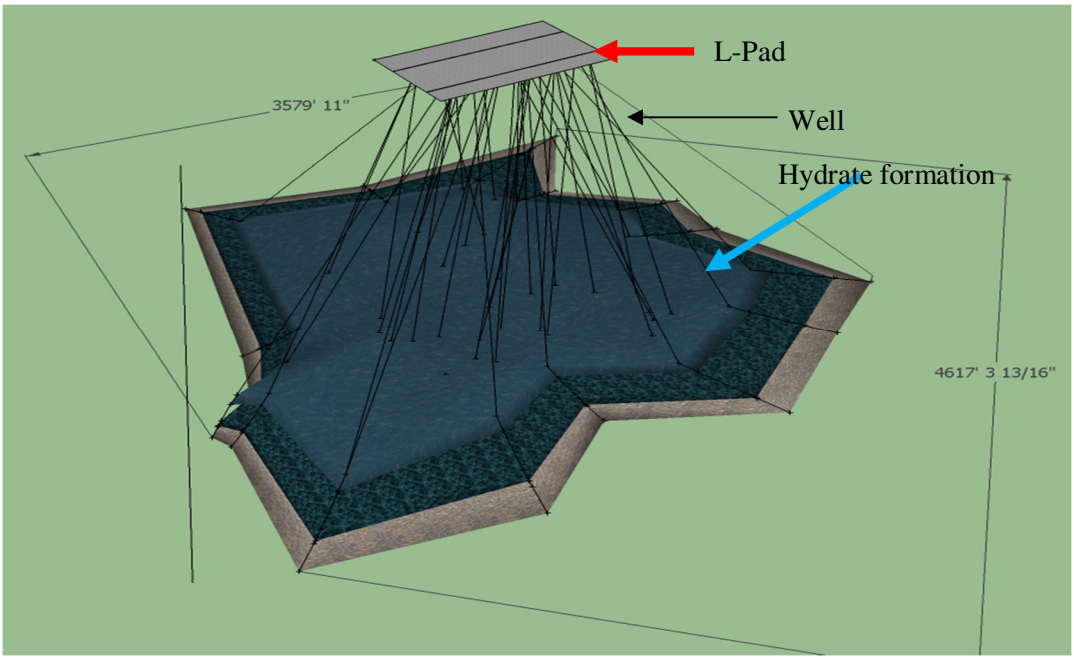

Figure 6.4 Schematic representation of Prudhoe-Bay Lpad

The base case problem originates from Prudhoe Bay L-pad site in Alaska. The geographical location is shown in Figure 6.3. The base case problem is adapted from the the International Methane hydrate code comparison project. The base case is a radial grid of radius 450 m and depth of 118 m. The shale layers in the periphery are 50 m deep. The geometric view of the grid is shown in Figure 6.5. The pressure and temperature of the uppermost layer of the hydrate bearing diment (HBS) are 7.327 MPa and 278.15 K. The hydrostatic pressure gradient 9792 Pa/m and the geothermal gradient is 3°C/100 m. The discretization of the grid in the r direction is logarithmic (from r_w = 0.1 m to r = 450 m) and in the z direction, the HBS is uniformly discretized while the shale layer is logarithmically distributed. The reeservoir parameters, relative permeability curves and capillary pressure are same as in the base model specified in Section 3.2.

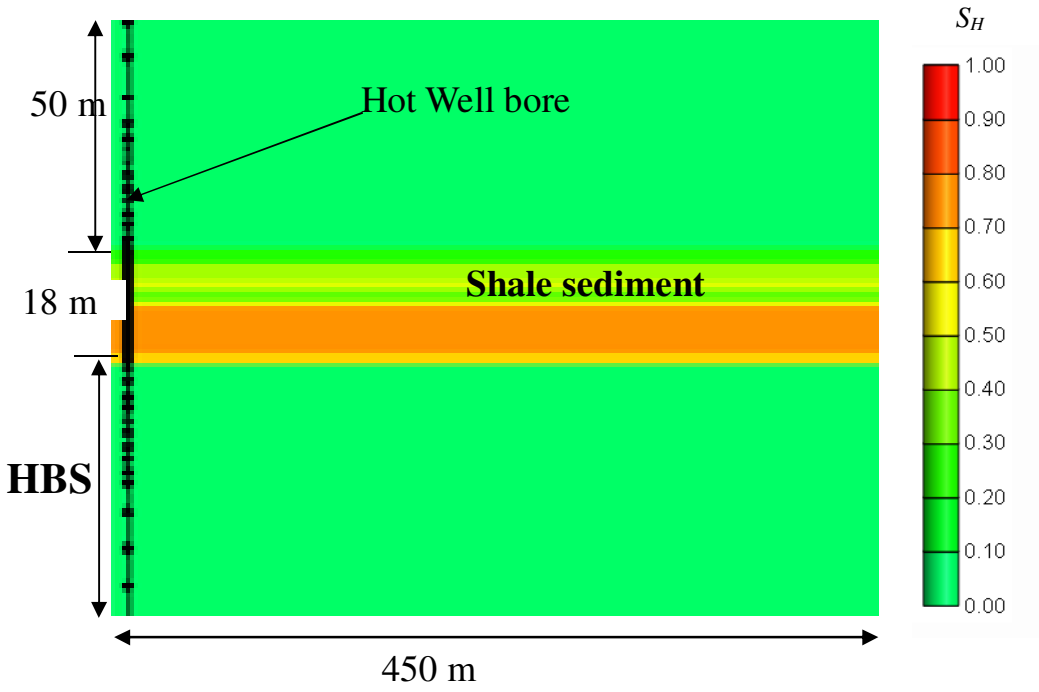

Figure 6.5 Geometric view of the grid

The temperature of the wellbore is maintained at 30°C for the base case. CMG STARS (STARS and Guide, 2008) coupled with a 2D finite element model is used for simulations. Fluid flow and formation deformation are coupled in a sequential manner, the two calculations are performed simultaneously passing information back and forth STARS inbuilt Flexible well bore model is used to accurately predict radial heat transfer from wellbore to the surroundings. A coupling of porosity as a function of pressure, temperature and mean stress is used. Elasto-plastic Mohr coulomb model is used for all simulations. The reservoir is constrained only at the bottom. The initial stress field is assumed to be isotropic. Table 6.1 lists geomechanical properties and initial stress used in the simulations

Table 6.1 Geomechanical properties

Property/Model	Hydrate Layer	Shale layer
Youngs Modulus	1 GPa	0.1 GPa
Friction angle	30	30
Cohesion	1100 kPa	200 kPa
Vertical Stress	15 MPa	
Horizontal Stress	15 MPa	

Base Case simulation results

All the simulations are run for a time period of 20 years using CMG STARS. The temperature of the wellbore is maintained at 30°C. Due to radial heat transfer hydrate dissociates quickly increasing the pressure around the wellbore by 1000 kPa. There is no secondary hydrate formation observed during the simulation. This high pressure rise at time t = 3 days acts as a barrier for further hydrate dissociation. Not a significant increase in pressure is observed at the end of simulation (t = 20 years) due to permeable under burden and overburden. A maximum of 12 m of hydrate bearing layer is dissociated in the horizontal direction as shown in Figure 6.6. A very low subsidence of 0.1 cm was observed initially (t = 5 days) due to rapid hydrate dissociation as shown in Figure 6.7a. Due to increase in the amount of gas around the well bore during the course of simulation, uplift is observed in the surrounding shale layer. This uplift increased to a maximum of 2 cm at the end of the simulation as shown in Figure 6.7b. A small

volumetric strain of 0.001% is observed around the wellbore. A very small decrease in the mean effective stress (increase in pore pressure) was observed at the surface.

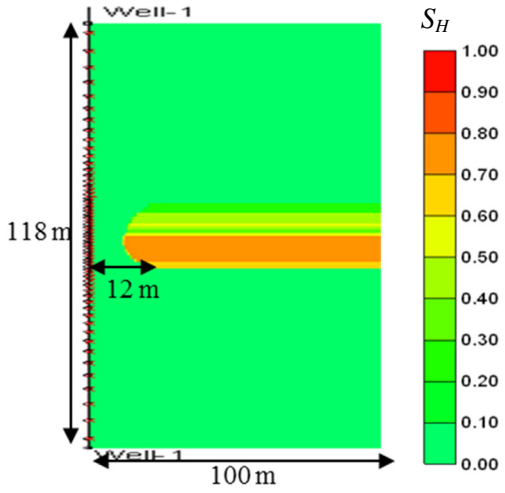

Figure 6.6 Hydrate saturation at *t*=20 years

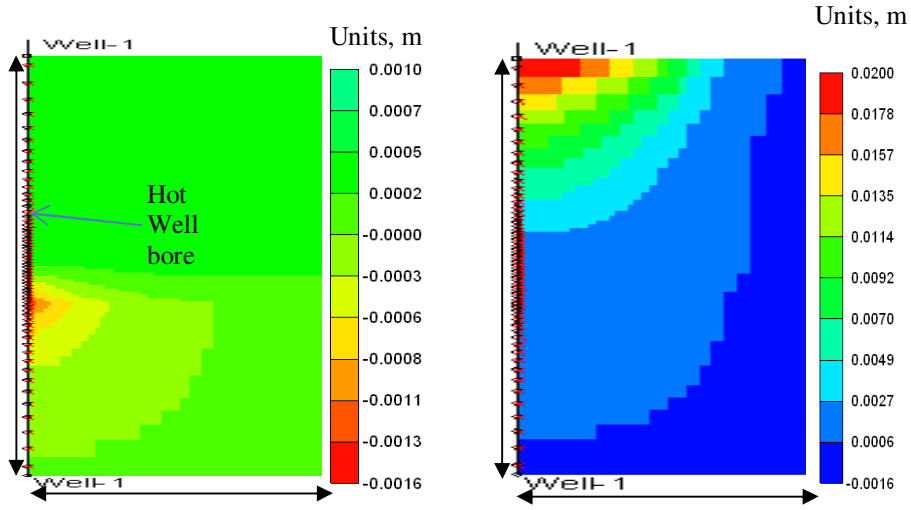

Figure 6. 7 Evolution of vertical displacement (negative of subsidence) around the well bore a) t = 5 days b) t = 20 years.

The lateral extent of hydrate dissociation was also small (~ 12 m) indicating no interference with nearby wells at Prudhoe Bay L-pad. This small disturbance of sediment around the well bore was because of permeable shale layers. Impermeable shale or different shale properties can affect

results creating a reasonable damage to the well bore. The geo-mechanical response to thermal loading primarily depends on thickness of hydrate bearing layer and porosity and permeability of under burden and overburden. The development of stress fields around the well bore can be significant. Well bore stability depends on the properties of surrounding shale layers. The thermal conductivity of the well and the cement as well as the sediment can largely effect near well bore stability. All these parameters might increase the volumetric strain causing sediment collapse.

6.4 Effect of impermeable shale on well bore stability

In impermeable formations there is no loss of fluid into the formation which can increase the pore pressure affecting well bore stability. In this study an impermeable shale (Shale porosity (φ_{sh}) – 0.0) is incorporated and modeled to see the effect on well bore stability.-An impermeable shale layer has increased the volumetric strain of the immediate shale layer by 10%. The lateral extent of hydrate dissociation was similar (~ 9 m) to the base case. Figure 6.8a shows the gas saturation profile around the well bore at the end of simulation. Pressure profiles at two different locations (P & Q) are recorded. The locations are shown in Figure 6.8b.

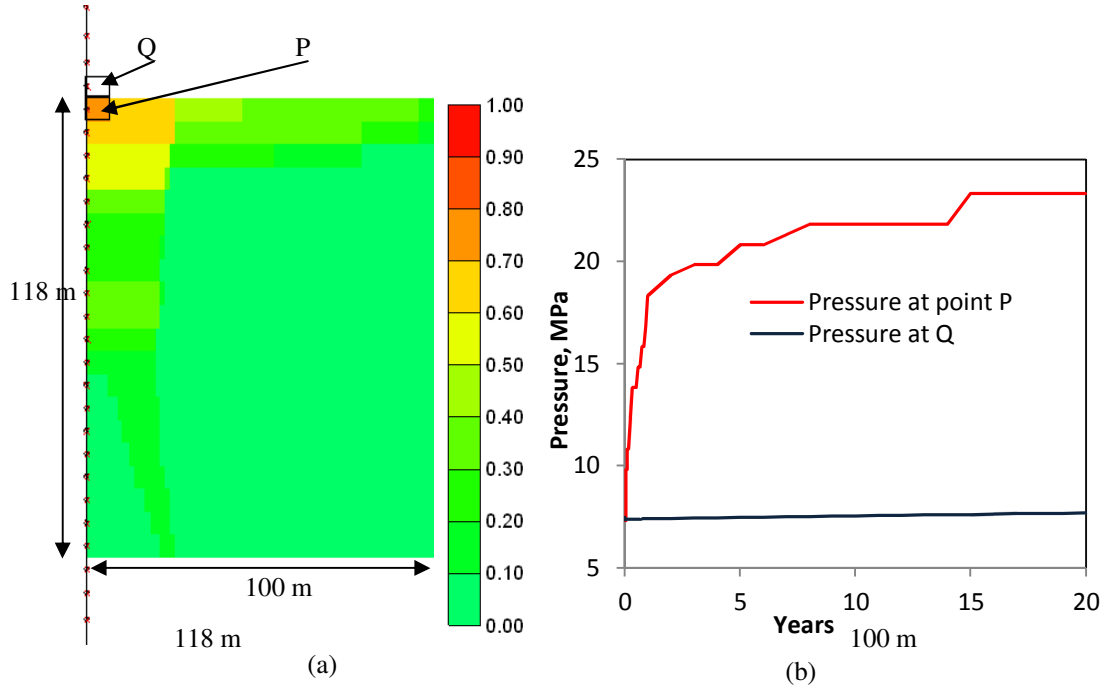

Figure 6.8 (a) Gas saturation distribution around the well bore for time t = 20 years, (b) Evolution of pressure at points P and Q

High pressure increase at point P due to hydrate dissociation is shown in Figure 6.8b. Decrease in the minimum effective stress of the shale layer surrounding the hydrate layer is observed.

6.5 Effect of Initial Conditions on well bore stability

The temperature of the well bore is changed from 30°C (base case) to 60°C with all other parameters same as the base case. Hydrate dissociation has increased laterally to 15 m from the wellbore. Initial saturations are calculated based on Archie's Equation resulting in average hydrate saturation as 0.6 for the base case. To understand the effect of hydrate saturation on the well bore stability a simulation with an average hydrate saturation of 0.4 is performed. The geomechanical response is similar except the fact that more hydrate dissociated (~ 12 m) around the well bore.

To consider the effect of deeper hydrate bearing sediments on well bore, the initial pressure and temperature of the top of the hydrate bearing layer is changed to 10 MPa and 9.8°C

respectively. All other parameters are same as the base case. No difference in geotechnical response was observed.

For the base case the absolute permeabilities of the HBS was derived from the well logs. A simulation was run by reducing the average vertical permeability (k_k) from 100 mD to 1 mD for the hydrate bearing layer. A drastic increase in the volumetric strain was observed around the well bore. Maximum volumetric strain observed near the well bore is -1%. Figure 6.9 shows the volumetric strain around the wellbore.

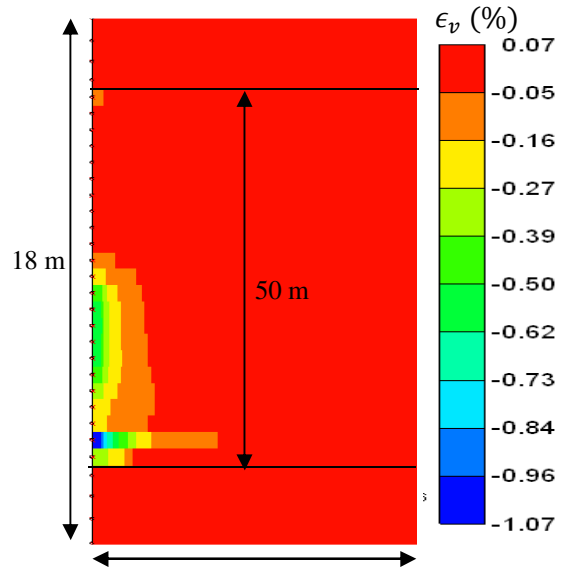

Figure 6.9 Volumetric strain around the wellbore at *t* = 10 days

6.5 Worst Case Scenario

Considering the effects of different parameters on well bore stability, a worst case scenario is simulated. Table 6.2 shows reservoir parameters for the worst case scenario. The parameters are

selected in such a way that each parameter change has a negative effect on well bore stability. An impermeable under burden and overburden are considered. The average absolute vertical permeability (K_k) of the hydrate bearing layer is reduced from 100 mD to 1 mD. The thickness of the hydrate bearing sediment is doubled from 18 m to 36 m. Young's modulus of the hydrate bearing sediment and the shale is reduced to 10 times the base case. Well bore temperature is maintained at 60°C. All other parameters are same as in the base case.

Table 6.2 Reservoir parameters for base case and the worst case scenario

Property	Base case	Worst Case Scenario
shale -Porosity, fraction	0.01	0
Average Permeability, mD	1000	1
Youngs Modulus, Gpa	1	0.1
Thickness of HBS, m	18	36
Well bore temperature, °C	30°C	60°C

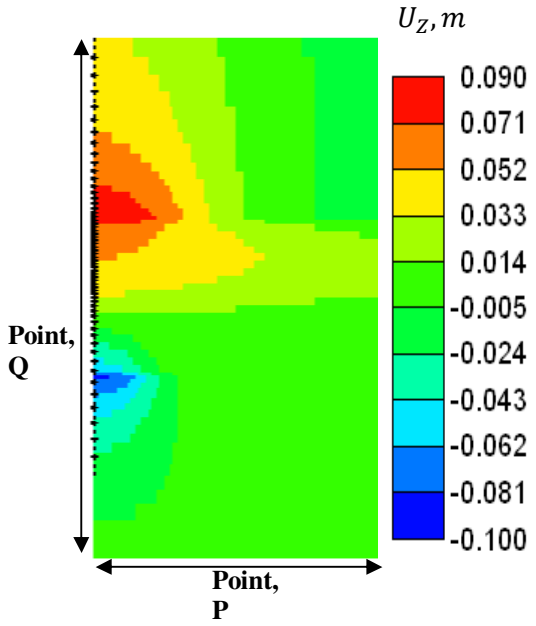

Figure 6.10 Vertical displacement for the worst case scenario at time *t* = 10 years

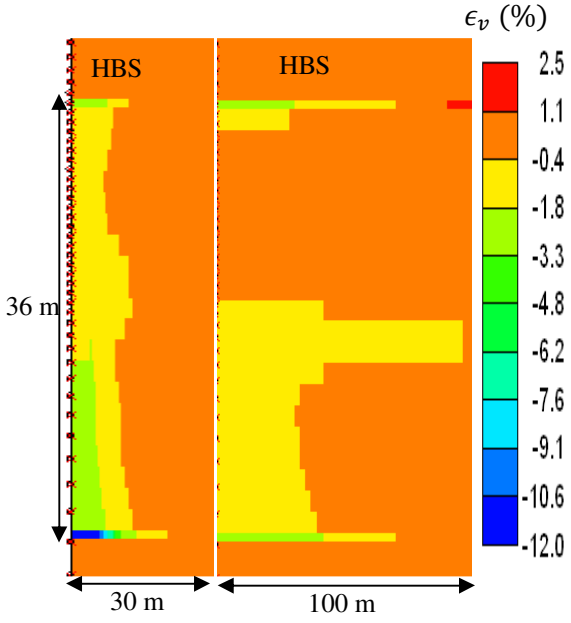

Figure 6.11 Evolution of volumetric strain for the worst case scenario a) *t* = 1 year b) *t* = 20 years

The lateral extent of hydrate dissociation around the well bore is found to be about 10 m in a period of 20 years. A maximum of 18 % volumetric strain is observed at an early stage (initial 10 days) around the well bore. The high volumetric strain is attributed to increase in pore pressure due to lack of pore space for the dissociated gas and water to move around the well bore. A

threefold increase in the permeability is observed around the well bore. This huge increase in permeability can be attributed to the increase in volumetric strain. As shown in Figure 6.12, subsidence and uplift is observed at the bottom and top of the hydrate bearing sediment respectively. Subsidence is caused by the hydrate dissociation releasing gas and water molecules. The gas molecules tend to move to the top of the hydrate bearing sediment causing a vertical uplift (displacement) at the top as shown in Figure 6.12. Subsidence is always a dominant mechanism and uplift plays an important role when there is impermeable shale surrounding the hydrate bearing sediment.

Figure 6.11 shows vertical displacement around the well bore at time 10 years. Due to rapid hydrate dissociation in the first 10 days, a maximum subsidence of 20 cm was observed. There is no secondary hydrate formation due to high well bore temperatures. Figure 6.12 shows the evolution of volumetric strain in a period of 20 years. Table 6.2 lists the results of the simulation

Table 6.3 Summary of Worst Case Scenario results

Worst-case scenario results		
Maximum value (around well bore)	t < 10 days	t = 20 years
Volumetric strain (%)	20	2.5
subsidence -Bottom of HBS (cm)	20	4.35
Uplift- Top of HBS (cm)	5.6	8.5

Conclusions

The extent of hydrate dissociation around a hot well bore is limited by the thermal diffusion of heat moving radially away from the casing and cement. The lateral extent of hydrate dissociation is in the range of 12 m around the well bore (maintained at 30°C). A very low subsidence of 0.1

cm is observed initially due to rapid hydrate dissociation. A maximum of 2 cm uplift is observed around the wellbore for a period of 20 years. A sensitivity study of different parameters on subsidence of the hydrate bearing sediment around the well bore is performed. HBS thickness, Porosity and permeability of under burden and overburden play a key role in deciding well bore stability.

Worst case scenario is modeled considering the effect of different parameters. A maximum volumetric strain of 18% with a subsidence of 20 cm is observed around the well bore**.** Development of stress fields around the well bore can be significant. Dipping structures and deviated wells can add complexity to this discussion on well bore stability

7. Conclusions

There is a vast reserve of hydrate accumulations in the United States. A fraction of the methane that is recovered from hydrates can address the energy demand to a great level. Since hydrate deposits are known to act as stabilizers of geological strata, it is important to know the behavior of hydrates and to understand the hazards of drilling in the ocean floor and continental shelves. Two hydrate accumulations in North Slope of Alaska and Gulf of Mexico are simulated for natural gas production.

A study of the propagation of Uncertainty propagation in gas production from PBU L-Pad North Slope of Alaska was done using a Latin hypercube sampling of porosity permeability, bottom hole pressure and hydrate reaction kinetics as uncertain parameters. Permeability of hydrate bearing sediment has the highest positive effect. Shale porosity and permeability has a negative effect on gas production. An increase in shale permeability showed a decrease in the gas production from methane hydrate due to less efficient depressurization. Hydrate dissociation activation energy has a higher negative effect than activation energy of hydrate formation. The probability distribution of discounted (15%) cumulative gas production with P50 of 213 MMScf (Maximum gas rate (10 years) – 190 Mscf/day), P10 of 135 MMScf (Maximum gas rate (10 years) – 225 Mscf/day) and P90 of 306 MMScf (Maximum gas rate (10 years) – 90 Mscf/day) is observed.

Gas production of horizontal well, deviated well to vertical well for Prudhoe Bay L-Pad site are compared. Gas rates for a horizontal well without pressure drop reached a maximum rate of 1059 Mscf/day (30,000 m^3/day) in 5 years. Gas rates for horizontal well with pressure drop reached a maximum gas rate of 600 Mscf/day (17,000 m^3/day) in 5 years. Pressure drop have a

huge negative impact on gas production from horizontal wells. The driving force for dissociation and fluid flow changes along the wellbore. Symmetry cannot be assumed in horizontal wells. Production of water is approximately 3 times more for horizontal wells. Integrated system of a well bore model with reservoir simulations is needed to accurately predict gas production from horizontal wells.

The gas production potential of Gulf of Mexico Walker Ridge 313 Blue and Orange hydrate deposits was investigated. A complex dipping 3-D reservoir models are developed based on available well log and seismic data. Reservoir simulations predict that the Gulf of Mexico hydrate accumulations can produce at high rates using conventional wellbore completion. A secondary hydrate barrier around a wellbore was observed during gas production in 1 year of production. The secondary hydrate formation has to be avoided for flow of fluids into the well bore. Gas production from WR 313 reservoirs displays high rates that can reach 65 MMscf/day for G well and 60 MMscf/day for H well.

Geomechanical modeling of thermal disturbance caused due to a hot well bore in hydrate bearing formation is studied. The lateral extent of hydrate dissociation is in the range of 12 m around the well bore (maintained at 30°C). A very low subsidence of 0.1 cm is observed initially due to rapid hydrate dissociation. Worst case scenario is modeled considering the effect of different parameters. A maximum volumetric strain of 18% with a subsidence of 20 cm is observed around the well bore**.** Development of stress fields around the well bore can be significant. Dipping structures and deviated wells can add complexity to this discussion on well bore stability. When geomechanically-weak sediments are involved, collapse of the formation around the wellbore is possible affecting installation of production structures and facilities over hydrate bearing sediments.

8. References

Anderson, B. et al., 2011a. Formation pressure testing at the Mount Elbert Gas Hydrate Stratigraphic Test Well, Alaska North Slope: Operational summary, history matching, and interpretations. Marine and Petroleum Geology, 28(2): 478-492.

Anderson, B. et al., ANALYSIS OF MODULAR DYNAMIC FORMATION TEST RESULTS FROM THE MOUNT ELBERT-01 STRATIGRAPHIC TEST WELL, MILNE POINT UNIT, NORTH SLOPE ALASKA.

Anderson, B.J. et al., 2011b. Regional long-term production modeling from a single well test, Mount Elbert gas hydrate stratigraphic test well, Alaska North slope. Marine and petroleum geology, 28(2): 493-501.

Anderson, B.J. et al., 2008. Analysis of modular dynamic formation test results from the Mount Elbert-01 stratigraphic test well, Milne Point Unit, North Slope Alaska. British Columbia, Canada.

Archer, D., 2007. Methane hydrate stability and anthropogenic climate change. Biogeosciences Discussions, 4(2): 993-1057.

Archie, G., 1942. The electrical resistivity log as an aid in determining some reservoir characteristics. I. Pet Tech, 5.

Aziz, K. and Settari, A., 1979. Petroleum reservoir simulation, 476. Applied Science Publishers London.

Beres, D.L. and Hawkins, D.M., 2001. Plackett-Burman technique for sensitivity analysis of many-parametered models. Ecological Modelling, 141(1-3): 171-183.

Bosch, M., Mukerji, T. and Gonzalez, E.F., 2010. Seismic inversion for reservoir properties combining statistical rock physics and geostatistics: A review. Geophysics, 75(5): 75A165.

Boswell, R. et al., 2011. Architecture of Gas-Hydrate-Bearing Sands from Walker Ridge 313, Green Canyon 955, and Alaminos Canyon 21: Northern Deepwater Gulf of Mexico. Marine and Petroleum Geology.

Boswell, R. et al., 2008. Investigation of Gas Hydrate-Bearing Sandstone Reservoirs at The" Mount Elbert" Stratigraphic Test Well, Milne Point, Alaska.

Collett, T. et al., 2010. Gulf of Mexico Gas Hydrate Joint Industry Project Leg II: Logging-While-Drilling Operations and Challenges.

Collett, T. and Scientific Party, N., 2007. Occurrence of Marine Gas Hydrates in the Indian Continental Margin: Results of the Indian National Gas Hydrate Program (NGHP) Expedition 01, pp. 01.

Collett, T.S., 1998. Well log evaluation of gas hydrate saturations.

Collett, T.S., Johnson, A., Knapp, C. and Boswell, R., 2009. Natural gas hydrates—a review. Natural gas hydrates—Energy resource potential and associated geologic hazards: 146–219.

Collett, T.S. and Ladd, J., 1995. 19. DETECTION OF GAS HYDRATE WITH DOWNHOLE LOGS AND ASSESSMENT OF GAS HYDRATE CONCENTRATIONS (SATURATIONS) AND GAS VOLUMES ON THE BLAKE RIDGE WITH ELECTRICAL RESISTIVITY LOG DATA1. The Program, pp. 179.

Crutchley, G.J., Pecher, I.A., Gorman, A.R., Henrys, S.A. and Greinert, J., 2010. Seismic imaging of gas conduits beneath seafloor seep sites in a shallow marine gas hydrate province, Hikurangi Margin, New Zealand. Marine Geology, 272(1-4): 114-126.

Dai, J., Xu, H., Snyder, F. and Dutta, N., 2004. Detection and estimation of gas hydrates using rock physics and seismic inversion: Examples from the northern deepwater Gulf of Mexico. The Leading Edge, 23(1): 60.

Dallimore, S.R. and Collett, T.S., 2002. Summary and implications of the Mallik 2002 gas hydrate production research well program. Scientific results from the Mallik: 1-36.

Doug, 2011. GAS HYDRATE SATURATION FROM RESISTIVITY ANISOTROPY. Proceedings of the 7th International Conference on Gas Hydrates.

Dvorkin, J., Nur, A., Uden, R. and Taner, T., 2003. Rock physics of a gas hydrate reservoir. The Leading Edge, 22(9): 842.

EIA, 2008. Annual Energy Outlook 2008 with Projections to 2030, Report DOE/EIA-0383.

EIA, 2011. US Energy Information Administration (EIA), 2011.

ESRI, A., 2001. Environmental systems research institute. California, USA.

Fohrmann, M. et al., 2007. Seismic characterization of the Fiordland gas hydrate province, New Zealand. Natural Gas Hydrates: Energy Resource Potential and Associated Geological Hazards: AAPG Special Publication. Pp.

Gaddipati, M., 2008. Code comparison of methane hydrate reservoir simulators using CMG STARS, West Virginia University.

Gamwo, I.K. and Liu, Y., 2010. Mathematical modeling and numerical simulation of methane production in a hydrate reservoir. Industrial & engineering chemistry research, 49(11): 5231-5245.

Hammerschmidt, E., 1934. Formation of gas hydrates in natural gas transmission lines. Industrial & Engineering Chemistry, 26(8): 851-855.

Helton, J.C. and Davis, F.J., 2003. Latin hypercube sampling and the propagation of uncertainty in analyses of complex systems. Reliability Engineering & System Safety, 81(1): 23-69.

Hunter, R.B. et al., 2011. Mount Elbert Gas Hydrate Stratigraphic Test Well, Alaska North Slope: Overview of scientific and technical program. Marine and Petroleum Geology, 28(2): 295-310.

Hyndman, R., Yuan, T. and Moran, K., 1999. The concentration of deep sea gas hydrates from downhole electrical resistivity logs and laboratory data. Earth and Planetary Science Letters, 172(1): 167-177.

Itasca, F., 2004. Fast Lagrangian Analysis of Continua in 3 Dimensions, User Manual, Version 3.1, Itasca Consulting Group. Inc., Minneapolis.

JAS, 1976-2011. Joint Association Survey on Drilling Costs (1976-

2011), American Petroleum Institute, Washington,

D.C.

Jones, E. et al., 2008. Scientific objectives of the Gulf of Mexico gas hydrate JIP Leg II drilling.

Kelley, J.T., Dickson, S.M., Belknap, D.F., Barnhardt, W.A. and Henderson, M., 1994. Giant sea-bed pockmarks: evidence for gas escape from Belfast Bay, Maine. Geology, 22(1): 59.

Kim, H., Bishnoi, P., Heidemann, R. and Rizvi, S., 1987. Kinetics of methane hydrate decomposition. Chemical Engineering Science, 42(7): 1645-1653.

Kleinberg, R., Flaum, C. and Collett, T., 2005. Magnetic resonance log of JAPEX/JNOC/GSC et al. Mallik 5L-38 gas hydrate production research well: gas hydrate saturation, growth habit, and relative permeability. BULLETIN-GEOLOGICAL SURVEY OF CANADA, 585: 114.

Kowalsky, M.B. and Moridis, G.J., 2007. Comparison of kinetic and equilibrium reaction models in simulating gas hydrate behavior in porous media. Energy Conversion and Management, 48(6): 1850-1863.

Kurihara, M. et al., 2008. ANALYSES OF PRODUCTION TESTS AND MDT TESTS CONDUCTED IN MALLIK AND ALASKA METHANE HYDRATE RESERVOIRS: WHAT CAN WE LEARN FROM THESE WELL TESTS?

Kvenvolden, K., 1993. Gas hydrates geological perspective and global change. Reviews of Geophysics, 31(2).

Kvenvolden, K.A., Lorenson, T.D., Survey, G. and Coastal, W., 2001. A global inventory of natural gas hydrate occurrence. USGS WR CMG.

Majumder, M., Identification of gas hydrates using well log data-A review.

Makogon, I.U.F., 1997. Hydrates of hydrocarbons. Pennwell Corp.

Masui, A., Haneda, H., Ogata, Y. and Aoki, K., 2005. The effect of saturation degree of methane hydrate on the shear strength of synthetic methane hydrate sediments, pp. 657-663.

Mavko, G., Mukerji, T. and Dvorkin, J., 2003. The rock physics handbook: tools for seismic analysis of porous media. Cambridge Univ Pr.

Max, M.D., 2003. Natural gas hydrate in oceanic and permafrost environments, 5. Springer.

McKay, M.D., Beckman, R.J. and Conover, W., 1979. A comparison of three methods for selecting values of input variables in the analysis of output from a computer code. Technometrics: 239-245.

McMullan, R.K. and Jeffrey, G., 1965. Polyhedral clathrate hydrates. IX. Structure of ethylene oxide hydrate. The Journal of Chemical Physics, 42: 2725.

MH21, 2012. Methane hydrate research consortium.

Moridis, G., 2008a. TOUGH+ HYDRATE v1. 0 user's manual: a code for the simulation of system behavior in hydrate-bearing geologic media.

Moridis, G. and Collet, T., 2003. Strategies for gas production from hydrate accumulations under various geological and reservoir conditions. Report LBNL-52568, Lawrence Berkeley National Lab., Berkeley: 1-49.

Moridis, G. et al., 2011. Challenges, Uncertainties, and Issues Facing Gas Production From Gas-Hydrate Deposits. SPE Reservoir Evaluation & Engineering, 14(1): 76-112.

Moridis, G., Kowalsky, M. and Pruess, K., 2005a. HydrateResSim Users Manual: A Numerical Simulator for Modeling the Behavior of Hydrates in Geologic Media. Contract No. DE-AC03-76SF00098. Department of Energy, Lawrence Berkeley National Laboratory, Berkeley, CA.

Moridis, G. and Reagan, M., 2007. Strategies for gas production from oceanic Class 3 hydrate accumulations.

Moridis, G., Reagan, M., Boswell, R., Collett, T. and Zhang, K., 2010. Preliminary Evaluation of the Production Potential of Recently Discovered Hydrate Deposits in the Gulf of Mexico.

Moridis, G.J., 2008b. The use of horizontal wells in gas production from hydrate accumulations.

Moridis, G.J., Seol, Y. and Kneafsey, T.J., 2005b. Studies of reaction kinetics of methane hydrate dissocation in porous media.

Mrozewski, S. et al., 2010. Gulf of Mexico Gas Hydrate Joint Industry Project Leg II: LWD Logging Program Design, Data Acquisition and Evaluation.

Myshakin, E.M., Gaddipati, M., Rose, K. and Anderson, B.J., 2011. Numerical simulations of depressurization-induced gas production from gas hydrate reserviors at the walker ridge 313 site, northern gulf of mexico. Marine and Petroleum Geology.

NETL, 2012a. International methane hydrate code comparison study.

NETL, C.P., 2012b. Ignik Sukumi gas hydrate field test: CO2/CH4 exchange.

Numasawa, M. et al., 2008. Objectives and Operation Overview of the JOGMEC/NRCan/Aurora Mallik Gas Hydrate Production Test.

Ocean, A., 2011. Rising Arctic Ocean temperatures cause gas hydrate destabilization and ocean acidification. Geophysical Research Letters, 38: L08602.

Pearson, C., Halleck, P., McGuire, P., Hermes, R. and Mathews, M., 1983. Natural gas hydrate deposits: A review of in situ properties. The Journal of Physical Chemistry, 87(21): 4180-4185.

Petalas, N. and Aziz, K., 2000. A mechanistic model for multiphase flow in pipes. Journal of Canadian Petroleum Technology, 39(6).

Petrel, 2011. Petrel Seismic Visualization software http://www.slb.com/services/software/geo/petrel/petrel_2011.aspx.

Plackett, R.L. and Burman, J.P., 1946. The design of optimum multifactorial experiments. Biometrika, 33(4): 305-325.

Pooladi-Darvish, M., 2004. Gas production from hydrate reservoirs and its modeling. Journal of Petroleum Technology, 56(6): 65-71.

Pooladi-Darvish, M. and Hong, H., 2010. Use of MDT Results over a Hydrate Interval at Mt. Elbert for Long Term Production Forecast–Implications of Uncertainties. Journal of Marine and Petroleum Geology: 1-11.

Reagan, M.T., 2010. The effect of reservoir heterogeneity on gas production from hydrate accumulations in the permafrost.

Revil, A. and Cathles, L., 1999. Permeability of shaly sands. Water Resources Research, 35(3): 651-662.

Ripmeester, J.A., John, S.T., Ratcliffe, C.I. and Powell, B.M., 1987. A new clathrate hydrate structure. Nature, 325(6100): 135-136.

Ruppel, C., 2011. Methane Hydrates and Contemporary Climate Change. Nature Education Knowledge, 2(12): 12.

Ruppel, C., Boswell, R. and Jones, E., 2008. Scientific results from Gulf of Mexico Gas Hydrates Joint Industry Project Legá1ádrilling: Introduction and overview. Marine and Petroleum Geology, 25(9): 819-829.

Rutqvist, J., 2008. Development of a numerical simulator for analyzing the geomechanical performance of hydrate-bearing sediments.

Rutqvist, J., Moridis, G., Grover, T. and Collett, T., 2009a. Geomechanical response of permafrost-associated hydrate deposits to depressurization-induced gas production. Journal of petroleum science and engineering, 67(1-2): 1-12.

Rutqvist, J., Moridis, G.J., Grover, T. and Collett, T., 2009b. Geomechanical response of permafrost-associated hydrate deposits to depressurization-induced gas production. Journal of Petroleum Science and Engineering, 67(1-2): 1-12.

Ryu, B.J. et al., 2009. Gas hydrates in the western deep-water Ulleung Basin, East Sea of Korea. Marine and Petroleum Geology, 26(8): 1483-1498.

Shelander, D., Dai, J. and Bunge, G., 2010. Predicting saturation of gas hydrates using pre-stack seismic data, Gulf of Mexico. Marine Geophysical Research, 31(1): 39-57.

Silpngarmlert, S., 2011. Modeling the Thermal disturbance of gas hydrate related to oil and gas production. Fire in Ice, Newsletter, Fall 2011.

Sloan, E. and Koh, C., 2007. Clathrate hydrates of natural gases. CRC Press.

STARS, C. and Guide, U., 2008. Advanced process and thermal reservoir simulator. Computer Modelling Group Ltd., Calgary, Alberta, Canada.

Stone, H., 1970. Probability model for estimating three-phase relative permeability. Journal of Petroleum Technology, 22(2): 214-218.

Tomasini, J., de Santa Ana, H. and Johnson, A., 2010. Identification of new seismic evidence regarding gas hydrate occurrence and gas migration pathways offshore Uruguay.

Van Genuchten, M.T., 1980. A closed-form equation for predicting the hydraulic conductivity of unsaturated soils. Soil Science Society of America Journal, 44(5): 892-898.

White, M. and McGrail, B., 2006. STOMP-HYD: A new numerical simulator for analysis of methane hydrate production from geologic formations, pp. 1-2.

Worthington, P.F., 2010. Petrophysical evaluation of gas-hydrate formations. Petroleum Geoscience, 16(1): 53.

Xu, H., Dai, J., Snyder, F. and Dutta, N., 2004. Seismic detection and quantification of gas hydrates using rock physics and inversion. Advances in the study of gas hydrates: 117-139.

Xu, W. and Ruppel, C., 1999. Predicting the occurrence, distribution, and evolution of methane gas hydrate in porous marine sediments. Journal of Geophysical Research, 104(B3): 5081-5095.

Yun, T.S., Santamarina, J.C. and Ruppel, C.D., 2007. Mechanical properties of sand, silt, and clay containing tetrahydrofuran hydrate.

Zhang, K., Moridis, G., Wu, N., Li, X. and Reagan, M., 2010. Evaluation of Alternative Horizontal Well Designs for Gas Production From Hydrate Deposits in the Shenhu Area, South China Sea.